Towards an ab-axis giant proximity effect using ionic liquid gating

Atesci, H.

Citation

Atesci, H. (2018, September 12). *Towards an ab-axis giant proximity effect using ionic liquid gating*. *Casimir PhD Series*. Retrieved from https://hdl.handle.net/1887/65452

Author: Atesci, H.
Title: Towards an ab-axis giant proximity effect using ionic liquid gating
Issue Date: 2018-09-12

Towards an *ab*-axis giant proximity effect using ionic liquid gating

Towards an *ab*-axis giant proximity effect using ionic liquid gating

Proefschrift

ter verkrijging van

de graad van Doctor aan de Universiteit Leiden,

op gezag van Rector Magnificus prof. mr. C.J.J.M. Stolker,

volgens besluit van het College voor Promoties

te verdedigen op woensdag 12 september 2018

klokke 13.45 uur

door

Hasan Ateşçi

geboren te Almelo

in 1990

Promotores: Prof. dr. J.M. Van Ruitenbeek
Prof. dr. ir. J.W.M. Hilgenkamp

Promotiecommissie: Prof. dr. ir. M. Huijben (University of Twente)
Prof. dr. J. Ye (University of Groningen)
Prof. dr. J. Aarts
Prof. dr. E. R. Eliel
Prof. dr. J. Zaanen

Casmir PhD series, Delft-Leiden 2018-09
ISBN 978-90-8593-357-1
An electronic version of this thesis can be found at
https://openaccess.leidenuniv.nl

This work is part of the research program with project number 12PR3047, which is financed by the Netherlands Organization for Scientific Research (NWO). The research of this thesis was performed at Leiden University and MESA + Research Institute of the University of Twente.

The cover image aims to summarize the ionic liquid gating performed on cuprates. The droplet in the background represents the ionic liquid. N,N-diethyl-N-(2-methoxyethyl)-N-methylammonium (DEME) cations and bis(trifluoromethanesulfonyl)imide (TFSI) anions. The ions are located just above the atomic terraces of a $La_{2\text{-}x}Sr_xCuO_4$ crystal.

Contents

Chapter 1

Introduction

Since its discovery in 1911 by Kamerlingh Onnes [1], superconductivity has been a very intriguing topic in physics. The advent of the Bardeen-Cooper-Schliefer (BCS) theory in 1957 made it possible to explain the basic mechanisms of superconductivity. The theory states that the electrons of the system undergo a bosonic transition, behaving as a single quantum mechanical wave function. The related order parameter is $\psi = \psi_0 e^{i\phi}$, where the amplitude of the wave function ψ_0 determines several key properties such as the energy gap Δ and transition temperature T_c. The highest T_c perceived to be possible (~30 K [2]) was reached with the compound Nb_3Ge in 1979 with a T_c of 23.2 K [3], which was surpassed in 1986 with the discovery of high-T_c superconductivity in the cuprate compound of $La_{2\text{-}x}Ba_xCuO_4$ with a T_c of 35 K. The subsequent discovery of many new cuprates culminated in critical temperatures as high as 150 K in $HgBa_2Ca_2Cu_3O_{8+\delta}$ only 6 years later [4]. Theoretically, it was clear that the original BCS framework was not adequate in describing this new class of compounds [2], and to this day there is no scientific consensus on the origins of some of the basic phenomenology of high-T_c superconductivity, e.g. the so-called pseudogap and the giant proximity effect. It seems that a general, BCS analog for the cuprate superconductors is even further away. Nevertheless, there is a renewed interest in the field due to improved growth techniques [5–7] and novel electrostatic charge induction mechanisms which use ionic liquids [8–11].

Among all the enigmatic issues regarding high-T_c superconductivity, this thesis aims to clarify the origins of the giant proximity effect (GPE) found in some systems where two superconductors are coupled by a weak link, also called Josephson junctions. Hence, addressing the GPE would first involve the concept of the standard proximity effect found between a superconductor (S) and a normal metal (N). The theory concerning this issue was developed in the 1960s [12], stating that when Cooper pairs leak from S to N, the order parameter amplitude of the Cooper pairs decays exponentially away from the superconductor over a characteristic length ξ, also called the coherence length, leading to a mutual altering of the properties of both materials. For Josephson junctions, where two interfaces are present, the results are analogous to the aforementioned case of a single interface. The supercurrent between both superconducting leads with a critical temperature T_c in such SNS junctions is given by [12]

$$I_c = \frac{\pi}{2eR_n}\frac{|\Delta_0|^2}{k_B T_c}\frac{d}{\xi_n}e^{-d/\xi_n}, \tag{1.1}$$

where R_n is the normal resistance of the metal, Δ_0 is the superconducting gap in the bulk of the superconductor, d is the thickness of the normal metal, and ξ_n is the superconducting coherence length in the normal region. Here, ξ_n decreases with temperature T as $1/T$ (clean limit: $\xi_n \ll l_n$) or $1/\sqrt{T}$ (dirty limit: $\xi_n \gg l_n$), with l_n the mean free path in N.

1.1 Giant proximity effect

Not all Josephson junctions behave according to this relationship. One of the first mentions of an anomalous proximity effect in high-T_c superconductors was made in 1991 regarding co-planar junctions of the cuprates $HoBa_2Cu_3O_{7\text{-}x}$/$La_{1.5}Ba_{1.5}Cu_3O_{7\text{-}\delta}$/$HoBa_2Cu_3O_{7\text{-}\delta}$ [13]. Here, supercurrents were detected spanning over distances reaching 500 nm, two orders of magnitude larger than the theoretical value of the coherence length [14]. Other reports include co-planar Nb-BiSb-Nb junctions [15] for distances reaching 1000 nm. Others, see Ref.16, used laser light with a specific energy to photoinduce local free holes in the CuO_2 planes of $YBa_2Cu_3O_{7\text{-}\delta}$. In doing so, Josephson junctions of varying separations could be made. Long range proximity effects could be seen in junctions with separations of up to 100 nm, while the coherence length is only 15 nm. In Ref.17 oxygen ion-irradiated junctions of $YBa_2Cu_3O_{7\text{-}\delta}$ could lead to Josephson coupling over large distances (up to 880 nm) between undamaged superconducting leads. Furthermore, in Ref.18, unconventional Josephson coupling was present in ramp-edge junctions of $Pr_{1.85}Ce_{0.15}CuO_4/Pr_{2-x}Ce_xCuO_4/Pr_{1.85}Ce_{0.15}CuO_4$, which are electron-doped cuprates. The coupling is independent of the concentration x of Ce^+ per unit cell and persists for barrier widths of up to 40 nm, approximately three times larger than the nominal coherence length. The same is not true for ramp-edge junctions of $La_{2-x}Sr_xCuO_4$ with a 50 nm thick barrier of $La_{1.95}Sr_{0.05}CuO_4$ stacked between its optimally doped electrodes [19].

The issue with the aforementioned co-planar geometric junctions is that it usually involves an ex-situ process of ion milling/damaging. This leads to a badly defined interface in terms of cation or oxygen stoichiometry, as argon ion milling tends to be a destructive process and involves oxygen vacancy production. Hence, in all of these *ab*-axis (i.e., in-plane directions, parallel to the *a* and *b* axes of the unit cell) reports, it is not clear whether the effect is intrinsic to the junction or is caused by the deficiencies in the method of preparation such as impurities by ion implantation, or interfacial effects due to improper growth techniques.

In *c*-axis geometry junctions (i.e., out-of-plane direction, parallel to the *c* axis of the unit cell), it is crucial that there are no superconducting shorts between the electrodes due to suboptimal growth of the barrier material. This can be caused either by superconducting shorts related to surface roughness being larger than the barrier thickness, or secondary-phase precipitates. These strict requirements were met using molecular beam epitaxy (MBE) methods. Using MBE, Bozovic *et al.* have been able to grow superlattices of $Bi_2Sr_2CuO_6/Bi_2Sr_2CaCu_2O_8$ [5] and $La_2CuO_{4+\delta}/La_{1.85}Sr_{0.15}CuO_4$ [6]. In both cases a supercurrent was found between the electrodes over distances of 10^2 times the corresponding coherence lengths along the *c*-axis in the temperature range of $T_{c'} < T < T_c$, with $T_{c'}$ and T_c being the critical temperatures of the barrier (S') and electrode (S), respectively. The observation has been coined the giant proximity effect (GPE). These reports showed that the GPE is indeed intrinsic. Similar results were found in pulsed laser deposited (PLD) $YBa_2Cu_3O_{7-\delta}/La_{2-x}Sr_xCuO_4$ superlattices [20].

Giant and anomalous proximity effects were also reported for metal superconductors [21, 22], indicating that the effect is not solely restricted to cuprate high-T_c materials, but seems to be more of a generic

Material	$\xi_{nominal}$ (nm)	L (nm)	Explanation given	Ref.
LSCO/LSCO(Sr=0.35)	$2-3$	10	Phase stiffness	[23]
LSCO(x =0.15)/LCO(4+δ)/ LSCO(x =0.15)	$0.1-0.2$	20	Resonant tunneling	[6]
LSCO(x =0.16)/LSCO(x =0.06)/ LSCO(x =0.16)	< 2.5	46	Resonant tunneling, phase pinning	[7]
YBCO/YBCO(6+δ)/YBCO	2	800	Resonant tunneling	[17]
YBCO(6+δ)/YBCO/YBCO(6+δ)	9	100	-	[16]
YBCO(6+δ)/LSCO/YBCO(6+δ)	< 1	20	Phase fluctuations	[20]
BSCO/BSCCO/BSCO	$0.1-0.3$	7.4	-	[5]
PCCO(x =0.15)/PCCO(x =0.05)/ PCCO(x =0.15)	4.5	35	-	[18]
HBCO/LBCO/HBCO	0.75	100	-	[13]
Pb+Pb/Si(111)	-	> 100	de Gennes	[21]
Nb/BiSb/Nb	-	1000	-	[15]

Table 1.1: List of long range proximity effect literature references, along with $\xi_{nominal}$, L (maximal width of the barrier that still shows a Josephson coupling) and the explanations given. Here, LSCO, YBCO, BSCO, BSCCO, PCCO, HBCO and LBCO are abbreviations for $La_{2-x}Sr_xCuO_4$, $YBa_2Cu_3O_7$, $Ba_2Sr_2CuO_6$, $Ba_2Sr_2CaCuO_8$, $P_{2-x}Ce_xCuO_4$, $HoBa_2Cu_3O_{6+\delta}$ and $La_{1.5}Ba_{1.5}Cu_3O_{6+\delta}$, respectively. If applicable, the doping levels of the respective cuprates are enclosed within parentheses.

effect of junction materials at temperatures in between both T_c's. A more comprehensive list of various literature references to the anomalous proximity effect can be seen in Table 1.1.

1.2 Schools of thought

It is important to note that until now there is no consensus on the origins of the GPE, and it is possible that different explanations apply for different systems. Some make use of conventional theoretical frameworks to explain the effect. In short, these make use of de Gennes' theory. The second type relates to the debated pseudogap physics, and several theories regarding superconducting puddles and phase pinning exist in this context. Others have come up with new mechanisms of Bose-Einstein condensation of real-space pairs [24], chiral d-density waves generated superconductivity [25], and type-II

Bose-Mott insulators.

1.2.1 Conventional de Gennes theory

Some explanations given for the GPE in the literature were given in terms of conventional de Gennes theory, as used for SN interfaces. According to Cherkez *et al.*, de Gennes already discussed the proximity effects between two superconductors with different critical temperatures and energy gaps [12], albeit qualitatively [21]. According to the authors, the local density of states of superconductors S and S' should be modified considerably in the sense that a local order is induced due to some attractive pairing interaction. The authors use the Usadel equations to quantify superconducting parameters at the interface, and find that the induced order parameter should decay exponentially as a function of the distance x from the interface, similar to de Gennes' theory:

$$\Delta \propto e^{-x/L_\Delta(T)}. \tag{1.2}$$

Here, $L_\Delta(T)$ is the temperature dependent decay length, which diverges near the $T_{c'}$ along de Gennes' theory as $L_\Delta \sim 1/\sqrt{T - T_{c'}}$. The authors of Ref.26 are of the opinion that also the results for $YBa_2Cu_3O_{7-\delta}$ can be explained with de Gennes' theory. They have put forward the idea that in most cases the $SS'S$ junctions concern one and the same material with different doping, as is the case in Ref.16. Due to this, they argue, the coupling constants of both the S and S' parts [27] of the junction are rather similar, leading to seemingly long range proximity effects. However, their suggestion does not account for the anomalous proximity effects seen in stacks of different materials, such as $YBa_2Cu_3O_{7-\delta}$ and $La_{2-x}Sr_xCuO_4$ [20].

1.2.2 Pseudogap phenomenon

When Cooper pairs are formed with a pairing energy Δ per electron, an energy gap opens in the density of states of the material, coupled to an increase of the electronic states just at the edges of the gap, which is confirmed by scanning tunneling spectroscopy [28] and other methods [29]. For high-T_c superconductors, the energy gap, however, does not disappear for temperatures higher than the critical temperature, when the material has a non-zero resistance, giving it an anomalous property, coined as the pseudogap. The exact physical origins of the pseudogap are still unknown, but it is most apparent in underdoped cuprates (see Fig. 1.1).

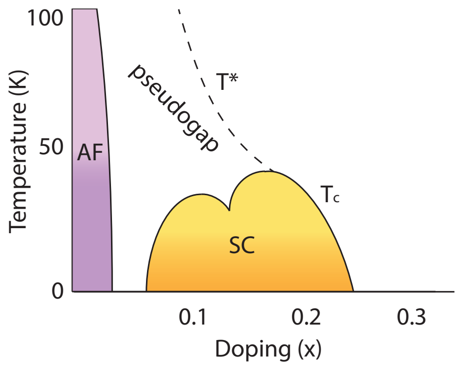

Figure 1.1: The typical phase diagram of hole-doped cuprates. Between the antiferromagnetic (AF) insulator and superconducting (SC) phases, a pseudogap is present at temperatures below $T^{*}>\mathrm{T}_c$, primarily in the underdoped regime.

According to some, the pseudogap represents a mixture of phases combined with the superconducting phase [30]. Others view the pseudogap as signifying preformed pairs as a precursor to superconductivity, which acquires global phase coherence only below T_c [31].

The latter is derived from the idea that amplitude and phase are the main parameters that describe the order parameter. The formation of Cooper pairs is not sufficient to induce superconductivity, as the pairs need to condense into a phase coherent quantum mechanical state [32]. Hence, this picture makes use of the competition between amplitude (i.e. pairing) and phase to account for the large pseudogap in underdoped cuprates. According to this view [32], pairing may dominate at low doping levels where the system is homogeneous. The large energy scale of pairing in the underdoped cuprates leads to a high pairing temperature T_p (see Fig. 1.2), which gets reflected in the pseudogap. Electronically, the material is spatially inhomogeneous and this inhomogeneity is followed by the order parameter, leading to a non-zero resistance. In particular, the phase stiffness of the order parameter is weakened and becomes susceptible to fluctuations. The phase fluctuations tend to decrease the phase ordering temperature T_θ [33], while the system transforms to a phase ordering regime when increasing the inhomogeneity through doping, leading to an increase (decrease) in T_θ (T_p). Hence, optimal T_c is found at intermediate doping levels.

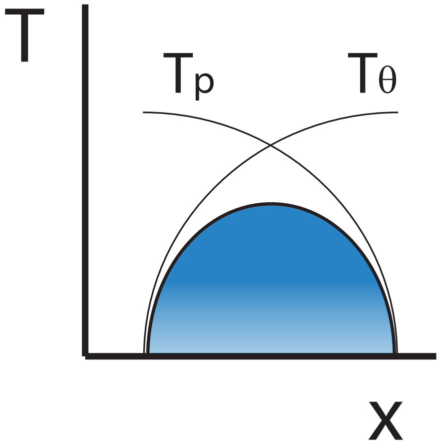

Figure 1.2: Phase diagram belonging to the physics of preformed pairs. The interplay between the pairing (T_p) and phase ordering (T_θ) temperatures as a function of doping x leads to an optimal critical temperature T_c at intermediate doping levels [32].

With this picture in mind, introducing phase stiffness in an underdoped cuprate provides the necessary ingredient to optimization of T_c. The necessary phase coherence can be provided by superconducting metals [34], or cuprates with large phase stiffness, present in either the superconducting regime [7] or the overdoped regime [23]. Consequently, Yuli *et al.* [23] reported substantial increases in T_c for underdoped $La_{2\text{-}x}Sr_xCuO_4$ films in the range of $x = 0.05 - 0.125$ when an overdoped layer of $La_{1.65}Sr_{0.35}CuO_4$ is grown as a capping layer. The authors mention that the effect is not attributable to strain effects or intermixing of Sr cations or oxygen within the layers. Rather, they suggest that the overdoped $La_{2\text{-}x}Sr_xCuO_4$ quenches the phase fluctuations present in the underdoped material, leading to larger phase stiffness and hence an enhancement of T_c in overdoped-underdoped multilayers. This approach is capable of explaining phase coherence effects in more generic systems which include non-cuprate superconductors as well, such as granular Pb films covered by a layer of Ag

[22].

The same argument can be used to explain the giant proximity effect in $SS'S$ junctions [35]. The critical current dependence on the temperature and barrier width is found to be qualitatively different than in the standard SNS case. More specifically, the effective T_c of the junction is predicted to behave as

$$T^{eff} \cong T_c \left[1 - \left(1 - \frac{T_{c'}}{T_c} \right) \frac{ln(d/\xi)}{ln(L/\xi)} \right]. \tag{1.3}$$

Here, d, ξ and L stand for the barrier width, the coherence length and length of the superconducting leads, respectively. T_c and $T_{c'}$ represent the critical temperature of the S and S' layers, respectively. These are proportional to their nominal critical temperatures. According to Ref.35, the giant proximity effect is visible for length scales smaller than the magnetic penetration depth λ. In light of the theory proposed, this should coincide with a ratio of $\ln(\mathrm{d}/\xi)/\ln(\kappa)$ that is sufficiently small, preferably below unity. Here, $\kappa = \lambda/\xi$, which for cuprates in the order of 10^2 - 10^4.

1.2.3 Superconducting puddles

Some theoretical works have made attempts to explain the giant proximity effect in light of inhomogeneous barriers [36, 37], in which the barrier material is considered to contain pockets of superconductivity. This concept is rooted in the preformed pairs picture of the pseudogap phase. Covaci *et al.* proposed that this is due to interstitial oxygen dopants, which enhance the pairing interaction locally [38]. Hence, these superconducting clusters will be linked through the proximity effect, leading to a current through the percolative paths, coupling the superconducting electrodes [39]. This is comparable to statements in Ref.36, in which a theoretical framework of the giant proximity effect was made by assuming an inhomogeneous nature of the barrier material. Here, superconducting islands are imbedded in a metallic matrix. This allows Cooper pairs to tunnel resonantly through a series of superconducting islands, comparable to what is stated in the works of Bozovic *et al.* [6]. The percolation-like interpretation should lead to the typical critical order parameter seen in percolation-driven conduction. Hence, the critical current I_c measured between the superconducting leads, is predicted to behave accordingly as [36]

$$I_c \propto (T/T_c - 1)^{\nu}, \tag{1.4}$$

where ν is the well-known critical index value of $4/3$ in percolation theory.

1.3 Novel theoretical explanations

1.3.1 Mott insulators

The concept of Mott insulators was introduced in 1949 [40], which stated that some materials that should be metallic according to standard band theory are insulating due to strong Coulombic electron-electron repulsive interactions. These effects are reported to become prominent in systems where the dimensionality of the system is reduced, such as one-dimensional GaAs wires, or undoped two-dimensional high-T_c superconductors [41]. The basic electronic characteristics of the cuprates is described using the archetypical cuprate $La_{2\text{-}x}Sr_xCuO_4$, the crystal structure of which is seen in Fig. 1.3a. Here, the CuO_2 planes are separated by charged reservoir layers. The insertion of Sr into the charged reservoir layers changes the charge carrier density of the planes. The Cu $3d$ or O $2p$ bands of the CuO_2 planes are the lowest in energy, hence responsible for the macroscopic electronic properties such as high-T_c superconductivity.

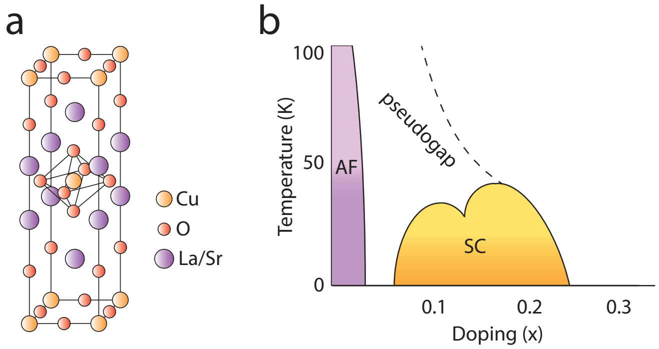

Figure 1.3: **(a)** The body-centered tetragonal structure of $La_{2\text{-}x}Sr_xCuO_4$ and **(b)** its phsase diagram. Different phases (antiferromagnetic (AF), superconducting (SC) and pseudogap) are present, depending on the temperature and doping.

The undoped compound La_2CuO_4 has an odd number number of electrons per unit cell, which under band theory conditions would be metallic. This is clearly not the case, as the compound is an antiferromagnetic (AF) insulator. This is due to the on-site electron repulsion U dominating over the hopping energy t, leading to a split in the conduction band. This scenario applicable is for $x = 0$ in the phase diagram of Fig. 1.3b. Introducing a certain concentration x of Sr^{2+} per unit cell as substitute for La^{3+} in the charge reservoir layers leads to holes in the CuO_2 planes of the material. This destroys the AF phase of the material until the pseudogap state is reached at high enough x. Increasing x further leads to superconductivity and eventually to a Fermi liquid-like phase.

1.3.2 Type-II Bose-Mott insulators

The phase of interest in this case is the superconducting one. Its main signatures are zero resistivity and the so-called Meissner state. In the latter state, the external magnetic field is expelled from the material completely. However, this is only valid for superconductors of type I, conventional superconductors such as Al, Hg and Pb. Type II superconductivity includes nearly all compound superconductors and behaves similarly to its type I counterpart only up to a critical magnetic field H_{c1}, after which the magnetic field penetrates the material, albeit in the form of magnetic flux quanta of $\Phi_0 = 2.07 \times 10^{-15}$ Tm^2 ordered in a vortex lattice. Only above a critical field $H_{c2} > H_{c1}$ does the superconductivity disappear (see Fig. 1.4a).

Making use of the concept of duality, Beekman and co-workers developed a stand-alone theory for the investigation of Bose-Mott insulators. Surprisingly, the theory offered new opportunities for interpreting the GPE [42]. Simply put, superconductors expel the external magnetic field, while insulators expel electrical currents. Superconductors of type II above a certain critical magnetic field H_{c1} allow for the penetration of the magnetic field in magnetic flux quanta Φ_0, leading to Abrokosov vortices. On grounds of duality, something similar should happen in its type II insulating analog, but now for the electrical current. Above a critical current, the insulator should allow for the penetration of this current, in the form of quantized supercurrent filaments (see Fig. 1.4b).

According to this theory, the main parameter which determines the phase transitions is the quantum disorder, expressed as U/J with $J = 4t^2/U$, the hopping parameter in the Bose-Hubbard Hamiltonian. At one end of the U/J spectrum, i.e. $U/J \to \infty$ the on-site repulsion dominates and the insulating phase shows up (see Fig. 1.4c), albeit of Type I. Lowering U/J to intermediate values induces a change to a Type-II Bose-Mott insulator. A further decrease leads to crossing over the quantum critical (QC) point and eventually to the familiar superconducting regimes.

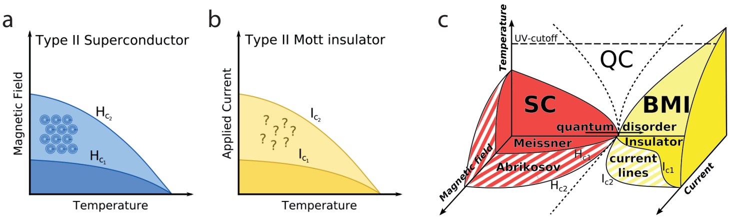

Figure 1.4: **(a)** Phase diagram of a typical type-II superconductor. For $H < H_{c1}$ the Meissner effect is present, while for $H_{c1} < H < H_{c2}$ the external magnetic field penetrates the material in magnetic flux quanta, leading to vortices. The superconducting state is cancelled for $H > H_{c2}$. The insulating analog of the type-II superconductor is the type-II Bose-Mott insulator, the phase diagram of which is shown in **(b)**. For $I < I_{c1}$ no external current is present in the material, which is not the case for $I_{c1} < I < I_{c2}$, where the current penetrates in quanta. **(c)** Phase diagram of the proposed type-II Bose-Mott insulator as a function of temperature, quantum disorder U/J and applied field and current. Adapted from [42].

The charge carriers in the material described by Beekman and Zaanen are bosons, similar to the Cooper pairs in superconductors, except that these experience a large amount of on-site, Mott-like repulsion. Hence, these materials are called type-II Bose-Mott insulators at intermediate U/J levels, or as U/J is controlled by doping, at intermediate doping levels as well. This suggests that the type-II Bose-Mott insulator could be found in the pseudogap phase where both the bosonic attraction and the electrostatic repulsion of electrons play a role, which can be found at approximately $x = 0.05$ for $La_{2\text{-}x}Sr_xCuO_4$.

Some crude estimates can be made regarding the quantum of current. It should be noted that while Φ_0 is a universal constant, the same cannot be said about the current quantum I_0. It is dependent on material properties such as phase velocity c_{ph} and the lattice parameter a. Its precise formulation is given by

$$I_0 = \frac{4\pi e c_{ph}}{a}. \tag{1.5}$$

Here, e is the electron charge. Approximating c_{ph} by the Fermi velocity (equal to 2.7×10^5 m/s) and using a = 3.9 Å results in $I_0 = 1.4\times10^{-3}$ A. These current quanta of I_0 are carried in filamentary structures and have a width given by the so-called Mott proximity depth,

$$\lambda_M = \lambda_L \left(\frac{c_{ph}\mu_0 e^2}{\hbar \Phi_\infty^2} \right)^{1/2}, \tag{1.6}$$

where λ_L is the London penetration depth. μ_0 is the magnetic permeability of free space and Φ_∞ is a dimensionless constant in the order of unity. Estimations have shown that this is up to two orders of magnitude smaller than λ_L [19].

If we take the aforementioned current quantum along with a typical critical current density of 1×10^9A/m^2 in La$_{2\text{-}x}$Sr$_x$CuO$_4$, the width of the filament would have to be at least ~1 μm wide, which requires λ_L to be very large. This would only be possible when this parameter starts to diverge near the superconducting phase transition.

The energy cost of the formation of a supercurrent filament would be linear in length. Therefore, the authors argue, the current can be carried across a significant length scale, and may offer an alternative explanation for the giant proximity effect.

1.4 Outline of the thesis

The theory developed by Beekman and Zaanen offers the possibility of an interesting new phase of matter that has not yet been discovered. A first possible area to search for such a new phase is in the pseudogap region of doping of high-T_c superconductors, which formed the initial starting point of the research project of this thesis.

The present theoretical framework offered by the authors provides a partial guide since it has a number of crucial unknowns, prime examples of which include the effects of finite temperatures on the current filaments. Furthermore, the theory assumes that the current quantum filaments enter into the type-II Bose-Mott insulator isotropically, while the distribution of charge carrier density in cuprates such as La$_{2\text{-}x}$Sr$_x$CuO$_4$ is concentrated at the copper-oxide layers and is hence very much two-dimensional. In addition, the finite thickness of the films might lead to difficulties in the hypothetical formation of the filaments in the *ab*-axis, as λ_M is in the order of 10 nm. Therefore we took the pseudogap phase as our starting point and focused on the interpretation of the mechanism for giant proximity effect.

Material-wise, a material is needed with an accessible phase diagram. For this requirement the cuprate $La_{2\text{-}x}Sr_xCuO_4$ is preferred. This has to do with the uniqueness of the $La_{2\text{-}x}Sr_xCuO_4$ system in that by simply changing the Sr concentration (albeit with some small oxygen non-stoichiometric possibilities), the whole of the phase diagram can be traversed. Furthermore, its crystal structure is the simplest among its cuprate counterparts with single CuO_2 layers [43]. In view of the sensitivity of the giant proximity effect to various growth inhomogeneities and imperfections, the material should be grown homogeneously and single-crystalline. Again, $La_{2\text{-}x}Sr_xCuO_4$ fits perfectly in this picture, as this has already been demonstrated by Bozovic and co-workers [6].

Based on the enhancement in the order of 10^2 of the distance over which Josephson coupling can be obtained in the c-axis in the experiments of Bozovic, the proximized effects should be observable for distances up to 400 nm in the ab-axis, as the coherence length is 3.2 nm.

In order to clarify the nature of the giant proximity effect, a number of experiments can be set up to differentiate between the applicability of the theories. This would mean that the behavior of three main junction parameters $T_{c'}$, I_c and ξ would have to be investigated qualitatively, and if possible, quantitatively as a function of barrier properties such as length L and temperature T.

Hence, in order to investigate the giant proximity effect in the ab-axis, a junction area has to be in its pseudogap phase, connected to superconducting leads. To pursue this, a number of methods are proposed and applied. The first proposal, as is described Chapter 8, makes use of ionic liquid gating on an initially superconducting film with a low T_c, indicated as S in (Fig. 1.5a). With this method, the gating is not applied everywhere on the film as an artificial junction area is made as the gating effect on top of this area is blocked by means of a barrier. The increased carrier density on the gated areas leads to a higher T_c, indicated as S'. Hence, the junction area at some point in temperature is in its pseudogap phase while the leads are still superconductors. The great advantage of this approach is that it allows creating a junction in a film that is structurally homogeneous. As this is a rather novel technique, the fundamentals of ionic liquid gating based on a thorough literature study is discussed in Chapter. 2. On the experimental side, the goal of mastering the ionic liquid gating technique lead us to perform experiments on various oxide materials such as $SrTiO_3$ (Chapter 4), $Nd_{2-x}Ce_xCuO_4$ (Chapter 5) and $La_{2-x}Sr_xCuO_4$ (Chapter 6).

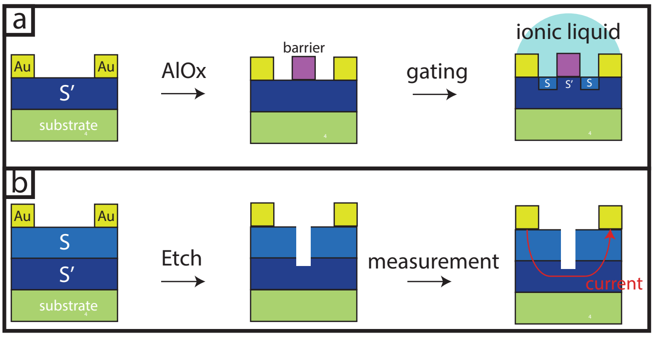

Figure 1.5: A schematic of two used methods of obtaining an *ab*-axis Josephson junction. **(a)** Ionic liquid gating-based Josephson junction. Here, the gating elevates the initial T_c. The barrier blocks the gating in the junction area. **(b)** The etched bilayer-based Josephson junction. The etched bilayer ensures that the flow of electrons between both S leads goes through the S' layer.

The second method makes use of etched bilayers, and is described in detail in Chapter 7. In short, this method involves the deposition of a film of low $T_{c'}$ (denoted as S'), followed by one of high T_c (denoted as S), see Fig. 1.5b. Etching away the top layer ensures that the flow of electrons between both S is through the S' area. The main advantage of this method is that the $\Delta\ T_c$ can be much higher than in the former method, as the top layer can be freely chosen. Furthermore, any electrochemical effect induced by the ionic liquid gating in the first method is circumvented in the etched bilayers. A disadvantage, however, is that the etched depth is not constant, as the top layer and interfacial layer between the top and bottom layers have some roughness. Hence, the etched depth needs to be increased to ensure that the top layer is completely etched away over the entire width of the junction area. Furthermore, the etching process leaves some disorder in the etched layer. For most hole-doped cuprates, this leads to a non-superconducting layer, the thickness of which is typically in the order of a few nm. A more important note is that the coherence length in cuprates is anisotropic, with the c-axis component usually smaller by an order of magnitude or more. Hence, if the etching depth is too much, this can annul any potential proximity effect between the superconducting leads.

The thesis is finalized with an outlook on the origins of the GPE based on key measurements made with both methods in Chapter 9.

Chapter 2

Ionic Liquids

For their importance in this thesis as a whole, a separate chapter is dedicated to the many aspects of ionic liquid (IL) gating. Gating by means of ILs covers only a small fraction of the total amount of research involving ionic liquids, the total research area of which has relevance in electrochemistry, photo chemistry, catalysis, electronics, and even clean energy [44, 45]. In terms of electrochemical aspects, ILs offer interesting research into memresistive devices. As an example, IL-induced memresistive properties have been shown in WO_x *[46],* TaO_x *[47],* TiO_x *[48],* $SrTiO_3$ *[49]and ZnO [50], the crux of which is the ability to attain controllable switching by means of structural or chemical defects. More relevant to the work done in this thesis is the importance of ionic liquid gating in the field of electronics, where the ability to large charge carrier densities is key. In this field, a large amount of research has been done on a host of materials including topological insulators [51], dichalocogenides [52–54], graphene [55], nickelates [56], manganites [57, 58], cuprates [10, 59–66] and other oxides [11, 67–73]. The oxide class of materials is the most relevant to this thesis, and hence the review below is dedicated specifically to ionic liquid gating experiments on these materials. For its importance in this thesis as whole, this chapter is dedicated to a literature discussion on charge carrier density induction using ionic liquids.*

2.1 Controlling the surface charge carrier density

ILs are molten salts having melting points below 373 K [44]. ILs are composed of organic or inorganic ions and differ from aqueous electrolytes in the absence of a solvent. Although the first IL was synthesized in 1914 [74], it took a long time before its first application for electrochemical studies, which started in 1980s. Since then, over 10^6 possible ILs have been proposed to exist [75]. The main cations that are used in IL applications are alkyls (C_nH_{2n+1}) bonded to pyridinium (C_5H_5NH), imidazolium ($C_3N_2H_4$), phosphonium (PH_4), ammonium (NH_4), etc. These are combined with anions such as ${BF_4}^-$, ${PF_6}^-$, ${NO_3}^-$, Cl^-, CH_3COO^-, ${CF_3SO_3}^-$ and $(CF_3SO_2)_2N^-$ [44].

The charged and solvent-free nature of ILs tends to lead to complex molecular organization and structure such as ion pairing or ion aggregation, governed by Coulombic, van der Waals, dipole-dipole interactions, hydrogen-bonding, and solvophobic forces. [76]. Hence, the properties of ILs are too complex to be described by classical theories for aqueous electrolytes [77]. By playing with the ionic species or length of cations and anions, the intrinsic cohesive and repulsive interaction profile of the ions changes, allowing one to change properties such as hydrophobicity, electrical conductivity, viscosity, melting point, and the electrochemical window.

The interfacial physics of ionic liquids is equally complex. In the most simple description, developed in 1853 by Helmholtz [78], two plates are assumed to be connected via an ionic liquid. A potential difference between these plates will drive a layer of cations (anions) to the surface by the electric field of the electrode plane at negative (positive) potential. Due to the fact that an ionic liquid is a good conductor the potential drop in the bulk of the liquid at the end of the process is zero. Screening of the electric field thus needs to happen at the interface with the plates. In short, the interfaces will form charged layers, or so-called electric double layers (EDLs), in essence a nanoscopic version of the macroscopic capacitor. The entire potential drop happens between these charged layers. The potential drop depends on the choice of model and the level of approximation, but in Fig. 2.1a we assume the profile to be linear.

In standard oxide dielectric field effect transistors (FETs), the drop in the potential happens over a distance which is up to two

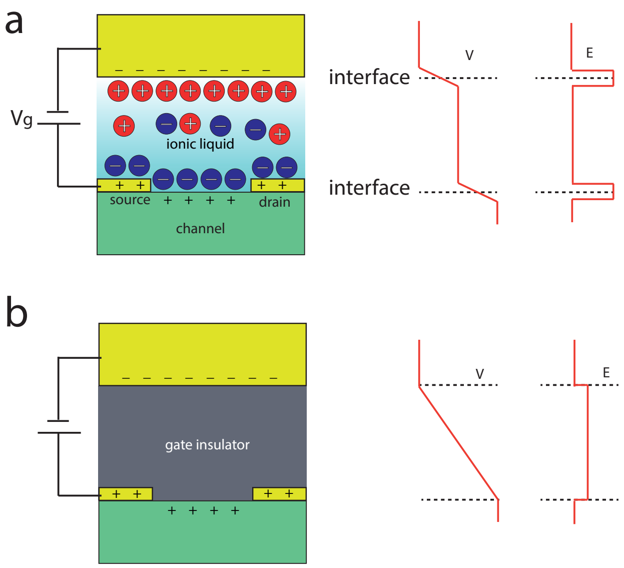

Figure 2.1: **(a)** Schematic overview of the gate/IL/channel system. A gate voltage V_g is applied between gate and source and the electric field is screened at the electrode and channel interfaces with EDLs. The potential difference V is maximized at the interfaces, approximated as a linear functions, with no potential difference in the IL. The electric field E, therefore, is maximized at the EDLs. **(b)** In a standard oxide dielectric field effect transistor, the drop in potential is distributed over distances that are up to two orders of magnitude larger than the EDL separation distance, leading to a substantially limited induced electric field.

orders of magnitude larger than in the case of EDLs (Fig. 2.1b) [79]. The induced polarization σ at a gate voltage V_g across a dielectric of thickness d and dielectric constant ϵ_r follows from Coloumb′s law as $\sigma = \epsilon_0\epsilon_r V_g/d$. Hence, the implications of a larger thickness to the induced polarization can, in principle, be compensated by applying a larger gate voltage. However, oxides tend to break down when a very high electric field E is applied across them, such that V_g has to be kept below $E_b d$, with E_b the breakdown field. The much-used SiO_2 in conventional Si FETs, for example, has a breakdown field of 10 MV/cm [80]. Together with a dielectric constant of $\epsilon_r = 3.9$, this leads to maximum polarization of 3.5 μC/cm^2 (or 2×10^{13} charges/cm^2), which is relatively small compared to polarization levels attainable with ionic liquids, typically in the order of $10 - 100$ μC/cm^2 [80].

The penetration of the electric field into a conducting film is counteracted by electrostatic screening, essentially limiting the field effect. The amount of screening depends on a variety of factors, as is formulated by the Thomas-Fermi model: the electric field in the conductor decays exponentially with a decay constant λ_{TF}. In the high-T_c cuprate superconductor $La_{2\text{-}x}Sr_xCuO_4$, $n_0 \sim 1.6\times\, 10^{21}/\mathrm{cm}^3$ at optimal doping $x = 0.15$, while ϵ_r is about 30 [81], resulting in a screening length of approximately 11 Å, i.e. slightly less than the c-axis lattice parameter of the unit cell. The superconducting properties at the surface are only fully tunable by the external, transverse electric field when λ_{TF} dominates the coherence length in the same direction, ξ_z. In the case of $La_{2\text{-}x}Sr_xCuO_4$, ξ_z is 2.2 Å [82], which is sufficiently small.

The field-induced surface charge carrier density induced by the IL gating can be written as [83]

$$\Delta n = \frac{1}{d}\int_0^d \frac{\epsilon_0\epsilon_{\mathrm{IL}}E}{e\lambda_{\mathrm{TF}}} e^{-z/\lambda_{\mathrm{TF}}}dz = \frac{\epsilon_0\epsilon_{\mathrm{IL}}E}{ed}(1 - e^{-d/\lambda_{\mathrm{TF}}}). \tag{2.1}$$

Here, e is the electron charge, while ϵ_{IL} is the dielectric constant of the IL of 14.5 [84] of, in this case, N,N-diethyl-N-(2-methoxyethyl)-N-methylammonium bis(trifluoromethylsulfonyl)imide (DEME-TFSI). Furthermore, d is the EDL distance of typically 1 nm. Assuming $d \gg \lambda_{\mathrm{TF}}$, the equation simplifies to $\Delta n = \frac{\epsilon_0\epsilon_{\mathrm{IL}}E}{ed}$. Hence, to turn the surface layer of the material of interest, the cuprate Mott-insulator La_2CuO_4 into its optimally doped state, a gate voltage of -2.0 V is needed.

In the experimental literature of $La_{2\text{-}x}Sr_xCuO_4$, we find that the effect is achieved at $V_g = -4.5$ V for the same IL and active film thickness, i.e. 1 UC [10]. For other materials, even smaller charge carrier densities have been reported. For $La_{0.8}Sr_{0.2}MnO_3$ [57], $SrIrO_4$ [85] and VO_2 [69], it has been found that gating hardly produces any effect electrostatically. These findings indicate that there are some factors that cause some degree of deviation from the ideal Helmholtz scenario, and that the complete process of gating is far from understood.

2.2 Deviations from the ideal Helmholtz scenario

The microstructure and capacitance of the electrical double layers (EDLs) at the IL/electrode interface play an essential role in determining IL-induced transport phenomena in oxides. To gain a certain degree of apprehension of these phenomena, a more detailed picture of the ionic liquid/oxide interface is needed, as there are some factors that contribute to the non-ideal Helmholtz scenarios. Although some experiments suggest that the IL/electrode interface is one ion layer thick (typically 3 to 5 Å) [86], the ideal Helmholtz layer picture negates the role of entropy. Thermal disorder leads to a diffuse EDL, where not all counterions are gathered in one layer [87]. Others have shown that alternating layers of cations and anions are formed and that the layering persists for many monolayers, as has been experimentally verified using X-ray reflectivity techniques [88]. As molecular shapes are often complex, with charges typically delocalized among many atoms, the layering and diffusivity and hence the capacitance of the EDL will also be dependent on these factors. The size of the anions and cations further influence the capacitance, as this will change the spacing between the charged double layers. A smaller ion size, for example results in a larger EDL capacitance, capable of inducing a higher interfacial charge carrier density.

Randomness of the charge order in the ionic liquid at the interface gives rise to a rapidly varying electrostatic potential which results in an exceptionally large decrease in mobility of the charge carriers in materials that are known to have highly mobile charge carrier densities, as experiments done by Petach *et al.* in Ref.89 have shown. In compensation for this effect, some have used a separator layer such as hexagonal boron nitride to limit the effects of the Coulomb scattering on the mobility [71]. However, the increased electric double layer distance has a negative influence on the polarization. Hence, one can expect an optimum in the induced conductivity as a function of separator layer thickness for gated materials in general, depending on the cation/anion species and the homogeneity of the anion/cation layer [90]. Theoretical studies have shown similar conclusions of inhomogeneity induced by IL in two-dimensional electronic systems based on specific features of the resistivity versus temperature [91], such as the width of the superconducting transition. Inhomogeneity in doping can also be caused by the suboptimal crystallinity and roughness of the surface. It was shown in Ref.92 that FeSe interfaces containing pits, the pits served as electron traps when gated with an IL.

The packing density is another intrinsic property of the EDL which has to be considered. This quantity is influenced by the intrinsic electron structure of the anion or cation. For example, ILs with coordinating imidazolium cations 1-ethyl-3-methylimidazolium ($EMIM^+$) and 1-hexyl-3-methylimidazolium ($HMIM^+$) are delocalized π-electron systems, which tend to have stabilizing stacking interaction between themselves, leading to a denser packing of the cations at the surface [93, 94]. Noncoordinating ammonium-based cations such as N,N-diethyl-N-(2-methoxyethyl)-N-methylammonium ($DEME^+$) do not have a delocalized π-electron imidazolium ring, leading to lower packing densities. The capacitance of the EDL is further dependent on the cation polarizability, and the preferred cation or anion orientation under the applied electric field [44, 86], for this determines the double layer thickness.

2.2.1 Surface electrochemistry

Since the start of IL gating for FET purposes in 1955 [95], there has been a massive amount of research in this field, with the number of published articles on this subject in the order of 10^4, and the number of gated materials in the order of 10^2. However, there seems to be no single, universal IL gating mechanism that applies to all of them [96], and only a fraction of those materials are behaving purely electrostatically when gated. The rest of the materials show some kind of electrochemical behavior.

But how do we distinguish electrochemical processes from electrostatic ones in the context of IL gating of oxides? Many electrochemical processes like oxygen vacancy production or ion intercalation are characterized by a large pseudocapacitance [97], which, through Faradeic charge transfer processes, accumulates charges in a slow way. Hence, such processes typically have large time constants [98], often leading to hysteresis effects [99]. However, a process with a long time constant is not a unique characteristic for electrochemistry, as there are some electrostatic cases where the interaction between the large electric field in the EDL and the oxygen electric dipole moments in cuprates such as $YBa_2Cu_3O_{7\text{-}\delta}$ [100] and $La_{2\text{-}x}Sr_xCuO_{4+\delta}$ [64] leads to a rearrangement of oxygen vacancies. In turn, this causes a change in the doping of the CuO_2 planes over time scales of minutes [83], comparable to typical electrostatic processes of hydrogenation and oxygen vacancy production [62, 63, 67]. Other characteristics of electrochemical reactions include irreversibility [101] and irreproducibility [52], though there are some oxygen vacancy processes in VO_2, TiO_2 and $SrTiO_3$ that are known to be reversible and reproducible as well [99].

In other words, electrochemical gating is not always distinguishable from electrostatic gating by means of reversibility, reproducibility and time scales. Although these criteria can still be used, additional measures need to be taken to obtain a complete picture. As charge transfer processes tend to be activated by the gate voltage and temperature, one can turn to the cyclic voltammetry as a tool to distinguish electrochemistry from electrostatics. Any charge transfer process increases the current between the gate and oxide electrodes, leading to a so-called charge transfer peak at the oxidation or reduction potential of the reaction. In case of electrostatics, no peaks are to be expected, and the integrated current should scale as a function of the applied gate voltage, V_g as $Q = CV_g$, with C the capacitance of the EDL interface with the oxide channel. In terms of temperature, the rate of activated processes scales exponentially via $I \propto e^{-E_a/k_BT}$, with I, k_B, T and E_a the current of the activated process, Boltzmann constant, temperature, and activation energy, respectively. The integrated gate current in such a case should follow an exponential behavior as a function of temperature as well.

What factors induce electrochemistry on the surface? If we start with ideal circumstances, the oxide channel is impermeable to ions, and the charge carrier accumulation or depletion happens electrostatically (see Fig. 2.2a). There are factors, however, that promote permeation of ion species to and from the oxide in the form of electron

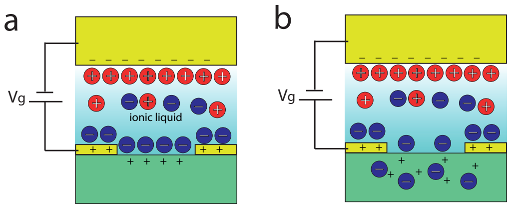

Figure 2.2: **(a)** IL-induced electrostatic gating: the charged interfaces are formed while no ion intercalation takes place, neither are there other processes that lead to stoichiometric changes in the channel. **(b)** In the electrochemical case, the stoichiometry of the channel is changed, in this case by means of ion intercalation.

transfer processes or diffusion of electroactive species (see Fig. 2.2b) [44]. These factors are the chemical affinity of the IL and the oxide surface, the crystal structure and crystalline quality of the oxide, the size and charge of the ions in the IL, or the magnitude and direction of the electric field induced in the EDL, the presence of impurities, the density of step-edges, etc. All of the different factors that could influence the electrochemistry are considered below.

2.2.2 Gate voltage and gate temperature related factors

Electric field-induced electrochemical processes can be independent of the IL-specific electrochemical window (EW) of the ionic liquid, defined as the voltage range in which the ionic liquid neither oxidizes or is reduced, i.e. stays electrochemically inert. The EW is determined by the range of potential differences for which the cation (anion) resists reduction (oxidation), with typical EWs ranging from 2.0-6.0 V at room temperature. Depending on the composition and structure of the ionic liquid and oxide material, there exists a voltage threshold above which electron transfer takes place between the surface and the ions in the liquid. The charge transfer leads to ion diffusion, because the ions converted at the interface need to be replaced, either from the liquid or solid side. The authors of Ref.49 show a bias dependence of oxygen vacancy production in $SrTiO_3$, whereby irreversible oxygen vacancy production is induced at $V_g \geq 3.75$ V, leading to surface degradation of several micrometers deep. Irreversible changes were also seen in nickelates, such as $NdNiO_3$ at $V_g \leq -2.5$ V [56]. For

$YaBa_2Cu_3O_{7\text{-}\delta}$, gate voltages as small as 0.9 V [63] or 1.0 V [102] can lead to electrochemical effects related to a change of the oxygen content of the film. Furthermore, electrochemical reactions often are found at only one voltage polarity [103–106]. As an example, $NdNiO_3$ as reported by Ref.107 shows electrochemical reactions for a specific regime of positive gate voltages, while for negative gate voltages no electrochemistry is observed.

When the gating is performed at a relatively high temperature, electrochemistry is induced at a larger rate, even at modest gate voltages. For example, gating experiments on $La_{1/3}Sr_{2/3}FeO_3$ leads to irreversible chemical reactions involving Fe and La migration into the IL, even before applying any gate potential [108]. The authors attribute the observed exchange of ions at the interface to the high gating temperature, related to the melting point of 60 C and to a higher reactivity of the IL used.

The fact that electrochemical processes are activated can be exploited to avoid breakdown at V_g above the EW. Hence, decreasing the temperature reduces the rate of the electrochemical reaction and hence effectively widens the EW. As an example, an EW of 2.7 V is found at room temperature for the IL gating of ZnO with DEME-TFSI [109]. The electrochemical window could be expanded up to 6.0 V simply by reducing the gating temperature to 220 K.

Furthermore, the direction of the field (i.e. polarity of the gate voltage) influences which type of anions or cations are taking place in the reaction. For positive gate voltages, oxygen vacancies can be induced, or cations (e.g. H^+) can be intercalated [69, 96, 102], which is not possible for negative voltages because of the Coulombic repulsive action. For negative gate voltages, oxygenation [63] can be induced, or negative ions can be intercalated [108].

In nickelates, for example, hydroxide ions produced by water electrolysis can react with Ni and degrade the film, as has been shown for $LaNiO_3$ [110]. Similar effects of degradation were observed in $SmNiO_3$ with experiments performed with unbaked IL having water contamination [103]. Furthermore, irreversible behavior is found at other materials, such as the ferromagnetic semiconductor $La_{0.8}Ca_{0.2}MnO_3$ at $V_g = -3$ V due to water contamination of the IL. Other examples include oxygen vacancy production at positive gate voltages in some materials, e.g. $La_{0.8}Sr_{0.2}MnO_3$ [57]. In other cases, e.g. Sr_2IrO_4, it can lead to oxygenation at negative voltages by means of a hydroxilation reaction, i.e. $Sr_2IrO_x + 2\delta OH^- \longrightarrow SrIrO_{x+\delta} + \delta H_2O + 2\delta e^-$ [85].

2.2.3 IL-related factors

IL gating on oxides adds an additional complication in the layering of the EDL, related to the binding affinity of the ions to the oxide surface. It is known that some cations or anions have acidic groups, and the acidic H atom of the imidazolium ring, for example, has a relatively strong coordinative hydrogen bond with the O atoms of an oxide surface, as is the case with TiO_2 [99]. The chemical bonding with the surface tends to be reversible, and increases the packing density and therefore increases the charge carrier density. However, these properties often lead to hysteresis effects and chemical modification [50]. Therefore, noncoordinating cations and an absence of acidic groups in cations is preferred when gating oxides, which is true for $DEME^+$. Similarly, in Ref.111 it was found that replacing the acidic H-atom of the imidazolium cation increases the stability of ZnO devices in ambient conditions. In $La_{1/3}Sr_{2/3}FeO_3$ an intermixing region even without bias application across the EMIM-PF_6/oxide interface leads to a surface reaction with the IL and involving Fe and La cations. This might be caused by the ${PF_6}^-$ anion reactivity with the surface, or the intrinsic instability of $La_{1/3}Sr_{2/3}FeO_3$ to ionic interfaces.

2.2.4 Packing-related factors

Apart from the properties of the IL, other factors that influence the chemical activity of the oxide surface with the IL is the surface energy of the crystalline facet facing the IL. As an example, it has been shown in TiO_2 that the facets with the highest surface energy tend to form more oxygen vacancies, which act as n-type dopants, and hence lead to a higher charge carrier density. This might be of relevance for gating on $SrTiO_3$, as TiO_2 is one of the terminations of the unit cell, and IL induced oxygen vacancy formation is also reported for this material.

The crystal structure of the oxide electrode interface is equally important influencing the doping mechanism of gating. Oxides with open unit cell structures with a high ionic mobility of oxygen and tendency to form oxygen vacancies, such as VO_2 [67] and $SrTiO_3$ [49], are prime examples of oxides susceptible to oxygen electromigration. Other oxides are relatively stable against oxygen vacancies, but have vacant sites in their unit cells. If these are surrounded by negatively charged ions, such as O^{2-}, these materials would have the tendency to be more sensitive to H^+ ion intercalation, such as the case with WO_3. And since H^+ is a ubiquitous impurity ion, this kind of electrochemistry would be easily detectible in materials that are prone to cation intercalation [96]. Other forms of intercalation are also possible in such materials involving K^+ and Na^+, for example when using a polyethylene oxide/$KClO_4$ [112] or polyethylene glycol/NaF [113] mixtures, respectively. Other oxides that have more compact crystal structures[113] are not sensitive to intercalation or oxygen electromigration, and hence perform purely electrostatically when gated with ILs, an example of which is indium tin oxide. Similarly, it was found that the high chemical stability of the ferromagnetic semiconductor $Ti_{0.9}Co_{0.1}O_2$ prevented the films from degrading, even at gate voltages of up to 3.8 V [114].

While the above applies for bulk samples, IL gating of thin films is accompanied by extra complications. The lattice mismatch between the film and substrate and other growth conditions can lead to crystalline defects such as grain boundaries and this has been shown to affect the mechanism of gating. As an example, thin films of epitaxially grown VO_2 on TiO_2 show reversible gating, while those grown on the lattice mismatched hexagonal Al_2O_3 lead to irreversible electrochemical reactions when gated [115]. Stoichiometry can also play a role, as is known from Ref.116 for the spinel $Zn_xFe_{3\text{-}x}O_4$ as the mechanism of gating changed depending on the Zn doping. The appendix provides the reader with a more comprehensive overview of the IL gating experiments.

2.2.5 Water as electroactive species

Water absorption in ILs is a key issue in IL gating, as it can reduce the EW and alter the device performance through electrochemistry [50, 62]. The presence of water dopes the IL with a weak Brønsted acid, because of which the IL becomes protic. This is accompanied by the formation of a proton and a hydroxyl ion, i.e. H^+ and OH^-. Compared to the typically large organic ions present in an IL, these dissociation products are smaller in size. Hence, at a given gate potential, one of the two species forms a physisorbed inner Helmholtz layer for which the separation distance with the interface is smaller as well, leading to significantly higher electrostatically accumulated charge carrier densities.

As our field of interest involves correlated oxide materials, the electrostatic picture of physisorption is susceptible to change, especially when using a multitude of (correlated) oxide materials having charged atomic layers in the unit cell. Stacking different oxide materials can lead to polar build-up of the electric field, the best example of which is $LaAlO_3$ on TiO_2-terminated $SrTiO_3$ [117]. The polarized termination in oxides, which is accompanied by a large surface energy, makes the surface more sensitive to charged ions [118], even more so to electroactive species such as H^+ or OH^-. When a certain termination has a higher affinity to one of the two species, applying the correct polarity of the gate voltage can lead to a charge transfer processes of hydroxilation or hydrogenation, representing OH^- or H^+ surface chemisorption, respectively. In such scenario, the electron transfer from and to the drain electrode dominates the induced changes in conductivity of the material, as opposed to the electrostatic effect of the EDL, as has been shown for different ZnO surface terminations [50].

More generally, the electroactive nature of H_2O shifts the cathodic (anodic) limiting potential of the sample towards the positive (negative) potential [119], essentially limiting the electrochemical window (EW) of the IL. The shift in the potential depends on the concentration of water in the IL. It has been shown, for example, that a 3 %wt H_2O contamination can diminish the EW by as much as 2.0 V [120]. Effects of unwanted electroactivity have been shown to exist even down to a level of tens of ppm [119]. In the cuprate class of materials relevant for this thesis, it was found in Ref.60 that simply applying the IL (DEME-TFSI) on the channel of a $LaCuO_{4+\delta}$ film even before applying any gate potential leads to the reduction of its conductivity and T_c of close to 20 K. Similar effects were found at the moment of application of the IL on a $YBa_2Cu_3O_{7\text{-}\delta}$ channel[62]. This is likely due to damage by the water contained in the liquid, as pumping eliminated the decrease in conduction.

Ionic liquids are also expected to have traces of halides, acids, residual solvents and other residuals which originate from the fabrication process, which, in principle, can act as dopants of the IL, similar to water. Likewise, similar electrochemical effects could be expected of these dopants if present in sufficiently large concentrations.

2.3 Conclusions

Ideally, we would like the electrochemical component of IL gating to be minimized, as some of the electrochemistry is irreversible and can affect the experiments in a negative way.

For this, we prefer the noncoordinating DEME$^+$ ion as this has a weak bond with oxygen atoms of the oxide material, as discussed in Section 2.2.

Furthermore, the IL should be kept free from any water as much as possible, as this is an electroactive species. One way of achieving this requirement is by selecting a hydrophobic IL [119], for example those with a bis(trifluoromethylsulfonyl)imide (TFSI) cation [121], widely used in IL gating experiments [8, 10, 49, 98, 122]. Furthermore, the partial pressure of these molecules has to be minimized. The reader is referred to Section 3.6 for a more specific description of the IL treatment.

Other considerations include the temperature, which has to be kept as low as possible while charging the ionic liquid, as the activated processes of electrochemistry are exponentially dependent on the temperature, as discussed in Section 2.2.2. Hence, to effectively maximize the EW, the experimental gate temperature needs to be minimized. To facilitate this, an IL needs to be chosen with a minimal melting temperature. DEME-TFSI has one of the lowest melting temperatures available for ILs of 183 K. Hence, together with the previous considerations in mind, we have decided to use DEME-TFSI for the IL gating experiments presented in this thesis.

2.4 Appendix

Here, the IL gating mechanism on a number of oxide materials, along with some its key parameters, are listed.

Material	IL	Gate (K) Temp.	IL treatment	V_g range	Gating mechanism	Ref.
Ferromagnetic semiconductors						
$La_{0.7}Sr_{0.3}MnO_3$	P(VDF-TrFE)	300	-	$-35V \leq V_g \leq 35V$	EC (oxygen vacancy)	[123]
$Pr_{0.65}(Ca_{0.75}Sr_{0.25})_{0.35}MnO_3$	DEME-TFSI	230	-	$-3 \leq V_g \leq 3V$	ES	[124]
$Ca_{1-}xCe_xMnO_3$	DEME-TFSI	300	1 Torr	$0 \leq V_g \leq 2V$	ES	[125]
$La_{0.525}Pr_{0.1}Ca_{0.375}MnO_3$	DEME-TFSI	220	-	$-3V \leq V_g \leq 3V$	ES for $-2V \leq V_g \leq 2V$ EC for $\|V_g\| \geq 2V$	[126]
$Ti_{0.9}Co_{0.1}TiO_3$	DEME-TFSI	300-320	-	$0 \leq V_g \leq 3.8V$	ES	[114]
$La_{0.8}Ca_{0.2}MnO_3$	EMIM-TFSI/ polyethylyne oxide + $LiClO_4$	298	-	$-3 \leq V_g \leq 3V$	EC for Vg = 3V	[127]
Ferrates						
$Zn_xFe_{3-x}O_4$	DEME-TFSI	300	5×10^{-5}Torr	$-1.5 \leq V_g \leq 1.5V$	EC (oxygen vacancy)	[116]
$La_{1/3}Sr_{2/3}FeO_3$	EMI-PF6	333K	-	$-2 \leq V_g \leq 0V$	EC:La/Fe migration	[108]
Nickelates						
$SmNiO_3$	TMEM-Py4	220	N_2 atmosphere	$-2.5 \leq V_g \leq 0V$	Without IL treatment: electrochemical etching for $V_g \leq$-1.2V With IL treatment: ES for $-2.5_g \leq 0V$ EC for $V_g \geq 0V$	[103]
$NdNiO_3$	BMPyr-TFSI	280	$p_{O_2}, H_2O \leq 1$ ppm	$-4V \leq V_g \leq 0V$	ES for $-3 \leq V_g \leq 0V$ EC for $V_g \leq -4V or V_g \geq 0V$	[104]
$NdNiO_3$	EMIM-DCA	240	120 C for 48 h	$-2.5V \leq V_g \leq 2.5V$	EC for $V_g \geq 0V$: oxygen vac. ES for $V_g \leq 0V$	[105]
$SmNiO_3$	TMEM-Py4	433	160C for 12h	$-2V \leq V_g \leq 2V$	EC for $V_g \leq 0V$:oxygenation $V_g \geq 0V$:oxygen vacancy	[106]

Material	IL	Gate (K) Temp.	IL treatment	V_g range	Gating mechanism	Ref.
Titanates						
$SrTiO_3$	PS-PMMA-PS:EMI-TFSI	300	-	$2.8V \leq V_g \leq 3.5V$	-	[73]
$SrTiO_3$	DEME-TFSI	190-210	10^{-5} Torr	$0V \leq V_g \leq 3V$	ES	[128]
$SrTiO_3$	EMIM-TFSI	300	10^{-7} mbar, 120 C for 12 h,	$0V \leq V_g \leq 2V$	EC: oxygen vacancy	[70]
$SrTiO_3$	Polyethylene oxide+$KClO_4$	320	-	$2V \leq V_g \leq 5V$	ES for $V_g \leq 3.75V$ EC:$V_g \geq 3.75V$	[49]
TiO_2	DEME/EMIM/HMIM-TFSI	280	10^{-7} Torr, 120 C for 12 h	$-2.3V \leq V_g \leq 2.3V$	EC: oxygen vacancy	[99]
Cuprates $La_2CuO_{4+\delta}$	DEME-TFSI	240	-	$1.2V \leq V_g \leq 3.0V$	EC	[60]
$La_{2-x}Sr_xCuO_4$	EMIM-DCA	300	-	$-2.5V \leq V_g \leq 3.2V$	ES: oxygen displacement	[64]
$YBa_2Cu_3O_{7-\delta}$	DEME-TFSI	220	10^{-2}Torr	$-4V \leq V_g \leq 10V$	EC: oxygen migration	[63]
$YBa_2Cu_3O_{7-\delta}$	Polyethylyne oxide+$KClO_4$	300	-	$0V \leq V_g \leq 3V$	EC for $V_g \geq 1V$	[102]
$YBa_2Cu_3O_{7-\delta}$	DEME-TFSI	240	-	$-2.52V \leq V_g \leq 2.0V$	inconclusive	[129]
$YBa_2Cu_3O_{7-\delta}$	Polyethylyne oxide+$KClO_4$/ Polyethylyne oxide+$CsClO_4$	300	-	$0V \leq V_g \leq 3V$	EC for $V_g \geq 0V$:oxygen vacancy	[130]
$Nd_{2-x}Ce_xCuO_{4-\delta}$	DEME-TFSI	210	60 C for several days	$0V \leq V_g \leq 2.5V$	EC	[131]

Material	IL	Gate (K) Temp.	IL treatment	V_g range	Gating mechanism	Ref.
Other oxides						
$SmCoO_3$	DEME-BF4	300	-	$-2V \leq V_g \leq 0V$	ES	[132]
ZnO	DEME-TFSI	220	10^{-1}Torr	$0V \leq V_g \leq 6V$	ES	[109]
ZnO	EMIM-TFSI,EMIM-TCB, EMIM-FAP,HMIM-FAP, EMMIM-TFSI,BMMIM-TFSI BMIM-TFSI	300	10^{-2}mbar, 60 C for 12 h	$1.5V \leq V_g \leq 1.5V$	ES except for BMIM-TFSI EC in ambient air	[111]
WO_3	DEME-TFSI, polyethylyne glycol+NaF	294-304	10^{-6}Torr	$-2V \leq V_g \leq 2V$	EC:hydrogen intercalation	[96]
WO_3	DEME-TFSI	230	120 C for several days	$0V \leq V_g \leq 2V$	ES	[133]
WO_3	DEME-TFSI, polyethylyne oxide+$LiClO_4$	300	70 C for several days	$-2V \leq V_g \leq 2V$	ES for DEME-TFSI, EC (Li^+ intercalation) for polyethylyne oxide+$LiClO_4$	[134]
WO_3	EMIM-TFSI,PYR14-TFSI	300	10^{-6} Torr, 80 C overnight	$-1.5V \leq V_g \leq 1.5V$	EC: protonation	[97]
Indium-tin-oxide	DEME-TFSI	-	-	$0 \leq V_g \leq 2.5V$	ES	[113]
InO_x	EMIM-TFSI	300	PO_2,H_2O $\leq 5000ppm$	$-1.03V \leq V_g \leq 1.03V$	-	[135]
VO_2	DEME-TFSI	-	-	$-3V \leq V_g \leq 3V$	ES	[11]
VO_2	HMIM-TFSI	300	-	$-3V \leq V_g \leq 3V$	EC for $V_g \geq 1.5V$: oxygen vacancy	[67]
$SrRuO_3$	EMI-TFSI	300	10^{-6} Torr	$-2.5V \leq V_g \leq 3V$	EC:oxygen vacancy	[136]

Chapter 3

Methods of fabrication of *ab*-axis Josephson junctions

The giant proximity effect in cuprate ab-axis Josephson junctions is investigated utilizing a number of methods, namely the gating by means of ionic liquids and etched bilayers. In this chapter, these methods are described along with the pulsed laser deposition technique used for thin film growth.

3.1 Pulsed laser deposition

As described in Chapter 1, in order to investigate the giant proximity effect in the ab-axis properly, an $SS'S$ junction needs to be made. In other words, a lower critical temperature ($T_{c'}$) of an S' area connected to higher T_c S leads. Furthermore, crucial to the making of Josephson junctions is the precise control of growth conditions of the thin cuprate films. For this, we have decided to use pulsed laser deposition (PLD). With the emergence of the laser era in the 1960s, several groups sought to investigate the excitation of atoms and laser-vaporization from solid surfaces [137]. Soon after, attempts were made to flash evaporate ma- terial using the laser as a heat source [138]. Early attempts in 1970s eventually culminated in stoichiometric deposition of multi-component films, such as $YBa_2Cu_3O_7$ films [139], and has since then been successfully utilized to fabricate high quality (epitaxial) ceramic films, ranging from superconductors to ferromagnetic materials.

Although PLD involves a lot of complex physics such as collisional, thermal and electronic excitation, exfoliation and hydrodynamics, in its core, it is a simple technique, using laser pulses to remove material from a target. The absorbed beam energy is converted into thermal, chemical and mechanical energy, which results in electronic excitation of the target surface atoms, and eventually in the ablation of the surface. The ablated material is contained in the form of a highly directional plume, which contains a collection of species, including ions, (clusters of) atoms, microscopic particulates. Once in contact with the surface of the substrate, the adatom essentially feels a hill-valley potential surface along both coordinates parallel to the surface. Initially, the single bond of the adatom with the substrate surface is usually weak, and allows the adatom to change adsorption sites, corresponding to the valleys of the potential surface (see Fig. 3.1). At some point, it can attach itself to another diffusing adatom, forming an island group. The saddle-like potential landscape of the step edges form natural pathways for adatom diffusion, facilitating a growth front of the adatom island. Detachment from the island group is also possible, or even from the surface of the substrate itself. In other cases, adatoms land on the surface of an adatom island, and, similarly to surface diffusion, can diffuse on the island surface. For sufficient diffusion lengths, the adatom can diffuse to the lower layer, called interlayer diffusion.

The deposition parameters are crucial in the nucleation process.

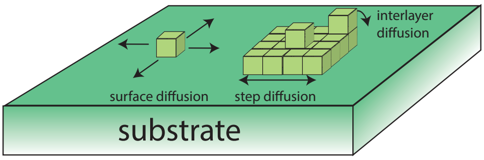

Figure 3.1: A simplified view of adatom dynamics at the substrate surface. Once attached to the surface, the adatom interacts with hill-valey potential landscape of the substrate surface, and can diffuse accordingly if this is energetically favorable. Adatoms can also form islands, the step edges of which form energetically favorable pathways for diffusion, called step diffusion, which facilitates the growth front of the island. Interlayer diffusion is also possible, which is caused by adatomic diffusion to a lower layer of the island.

In view of the vast growth parameter space, however, there is usually no unique set of growth conditions for a specific growth mode of the cuprate. For example, parameters involving the incoming energy of the ablated species, such as the laser fluency and background gas pressure play a role in the crystallinity of the film and the type of growth [140, 141]. Specifically, a higher (lower) laser fluency leads to a higher (lower) nucleation density of adatoms, while increasing (decreasing) the back- ground gas pressure decreases (increases) the landing energy of the ablated material, leading to the other growth modes. Furthermore, the substrate temperature strongly influences the diffusion constant of the adatoms, and therefore the diffusion length scales of adatoms. The temperature should be high enough to ensure adequate atomistic surface mobility at the film growth front. For this reason, an increase in temperature tends to decrease nucleation density and hence influence the growth mode. Parameters relating to the substrate surface, such as termination, miscut angle and roughness also influence the type of growth mode. For cuprate high-T_c superconductors, there is an additional parameter involving the oxygen pressure during deposition, as oxygen is crucial for stoichiometric mass transfer from target to substrate. A too low oxygen pressure can lead to the wrong oxygen stoichiometry and hence charge carrier doping of the film, or can even lead to the decay of the film.

3.1.1 Reflection high energy electron diffraction

Reflection High Energy Electron Diffraction (RHEED) is a tool that is used to in-situ monitor the type of growth mode of crystals. A high energy electron beam at a glancing angle is directed at a sample (see Fig. 3.2). The electrons are diffracted at the surface and then reach the detector, where a diffraction pattern is formed. The spot distribution information is used to analyze the surface morphology of the grown film. As a first step in understanding RHEED, we use the Ewald construction. Starting from a row of atoms along one spatial coordinate, the Fourier transform in k space of this row will be equidistant planes perpendicular to the row [142]. If a sphere is drawn in k space centered on the tip of the incident wave vector k_0, while ignoring the loss of energy and multiple scattering events in the sample surface, there will be some (e.g. k_1 and k_2) diffracted wave vectors having the same magnitude as k_0, satisfying both the elastic scattering and diffraction conditions, which lie on the intersection of the reciprocal lattice planes and the Ewald sphere, i.e. circles. In such a case, there is reflection from the family of direct lattice planes perpendicular to those reciprocal lattice vectors.

If we take the case of a two-dimensional, square lattice surface, the two rows of atoms are rotated 90 degrees from each other. Hence, its Fourier transform is an intersection of planes rotated 90 degrees from each other as well, resulting in reciprocal rods. The intersection of these rods and the Ewald sphere appears as diffraction spots on the fluorescence screen on the circles, known as Laue zones (see Fig. 3.3a). However, diffraction on real samples differs from the ideal, 2D diffraction case. For example, the 2D surface of the substrate is inclined 0.05-0.3 degrees. Furthermore, the growth of cuprates such as $La_{2\text{-}x}Sr_xCuO_4$, $Nd_{2\text{-}x}Ce_xCuO_4$ and $YBa_2Cu_3O_{7\text{-}\delta}$ additionally suffers from surface roughness, finite size domains, and 3D islands, all of which can lead to modifications of the RHEED patterns. In the case of the film having finite-sized domains, the reciprocal rods are widened by an amount which is inversely proportional to the average size of the domains. The intersections of these widened rods with the Ewald sphere are ellipses, leading to a streaked diffraction pattern (see Fig. 3.3b). When the surface is roughened with 3D islands, its reciprocal lattice is the same as that of a 3D crystal, which is a 3D array of reciprocal points. This will give an array of equidistant points in the RHEED pattern (see Fig. 3.3c).

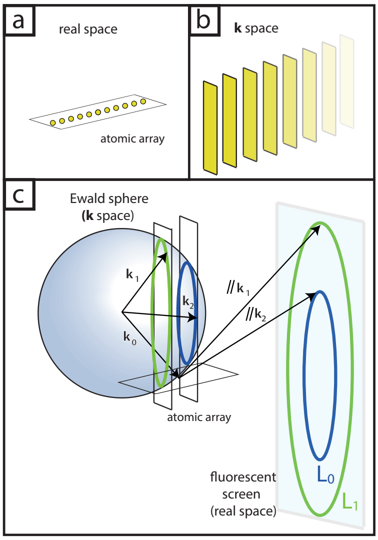

Figure 3.2: **(a)** An array of atoms, when Fourier transformed, gives rise to a series of equidistant planes, or reciprocal lattice planes **(b)**. An incoming beam of electrons of wave vector k_0 gives a diffraction pattern, based on the intersection of the reciprocal lattice planes of the 1D array with the Ewald sphere having a radius of $|k_0|$. These intersections are circles, and the wave vectors from the center of the Ewald sphere to the circles correspond to the wave vectors of the diffracted electrons, in this case k_1 and k_2. **(c)** The circles appear in real space as so-called Laue zones $L_0, L_1, L_2, ...$ when depicted on a fluorescent screen.

3.1.2 Growth modes

As described above, the spatial change of the diffraction pattern can tell something about the surface morphology of the grown film. We can also use the time-dependent change of the RHEED signal to determine what kind of growth modes are present during deposition. The principle behind this is based on diffraction of the electron waves from the surface of the sample. And as is the case for every kind of diffraction phenomenon, the path difference of different electron waves diffracted from the surface can lead to destructive or constructive interference, leading to changes in the intensity of the beam, which is monitored as a function of time. Hence, the time-dependent RHEED signal can be used to distinguish between an atomically flat surface and a stepped surface by measuring the intensity of the specular spot,

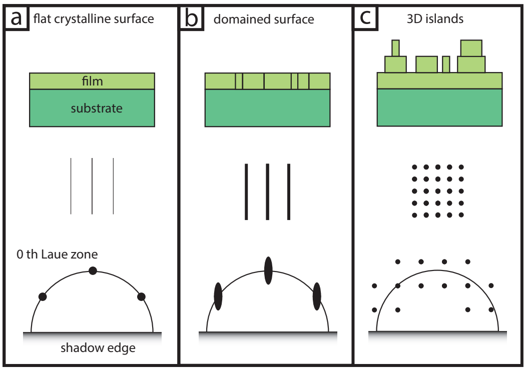

Figure 3.3: **(a)** The Fourier transform of a flat, crystalline surface, is the intersection of the reciprocal planes rotated 90° with respect to each other, i.e. reciprocal rods. The intersection of these rods with the Ewald sphere is a series of points on the 0^{th} Laue zone. **(b)** When some anomaly is introduced in the form of domains, the reciprocal rods are broadened, giving rise to ellipses when intersected with the Ewald sphere, visible as clear strokes on the fluorescent screen. Finally, in the case the surface is coarsened considerably, the diffraction pattern becomes spotty, similar to the 3D array of points in k-space of a bulk crystal **(c)**.

and can thus give an indication of the kind of growth mode present during deposition of the film material. The initial substrate surface is assumed to be flat, as seen in Fig. 3.4a. The incoming beam and the reflected, specular beam at a certain glancing and exit angle θ, are thus reflected from the same atomic plane. The two paths shown always have constructive interference, since there is no path difference between them, enhancing the intensity of the specular spot. Hence, there is an initial maximum in the spot intensity.

During the initial stages of deposition, some 2D islands of deposited material start to form. This introduce a height difference on the initial, flat surface (see Fig. 3.4b), meaning that a part of the specular beam is reflected from the substrate surface, while another is reflected from the 2D island, leading to a path difference between both parts of the beam. At a certain incident angle θ, this can result in destructive interference, leading to a decrease in specular beam intensity. The intensity reaches a minimum when there is a maximum destructive interference due to maximum surface roughness, i.e. when the fractional coverage of monolayers (ML) is 0.5. A continuation in deposition completes the first layer, and hence leads to a

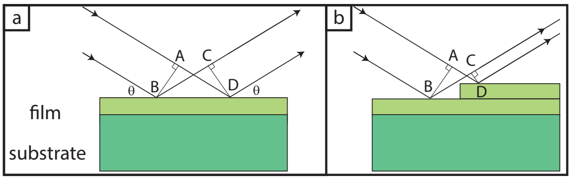

Figure 3.4: **(a)** The two paths of an incoming electron beam at an angle θ are reflected from the same atomic plane of the film. The distances traveled between points A-D and B-C are the same, leading to constructive interference in the specular beam, and hence an enhanced intensity of the specular spot. **(b)** If there is a some surface height difference is introduced by means of deposition, for example, the distances A-D and B-C are not equal anymore. If θ is chosen accordingly, this leads to the specular beam interfering destructively, leading to an decrease in intensity of the specular spot.

maximum in intensity. If we assume this growth mode to be cyclic, in which the next monolayer (ML) is initiated only after the previous layer is fully covered, oscillatory behavior in RHEED intensity is to be expected, with the period of oscillation corresponding to the deposition time needed to complete 1 ML, and more specifically to the time needed to satisfy charge neutrality of the unit cell (UC) [143]. In case of $La_{2\text{-}x}Sr_xCuO_4$, for example, this corresponds to 2 periods of oscillation. This type of growth is called layer-by-layer (Frenk-Van der Merve) growth. Layer-by-layer growth mode is stimulated in conditions of relatively high temperature and low oxygen pressure. In such conditions, the nucleation on top of a 2D island is minimized, such that adatoms can migrate to the step edges of 2D islands, and nucleation takes place on fully completed layers, i.e. when both the interlayer diffusion and mobility of adatoms are maximized. Another factor which stimulates layer-by-layer growth mode is minimizing the lattice mismatch between substrate and film.

Changing the experimental growth conditions or increasing the lat- tice mismatch can induce changes in this mode of growth to a 3D island growth mode. A low substrate temperature and high oxygen pressure pressure, diminish the interlayer diffusion and adatom mobility, leading to nucleation also on top of 2D islands. Hence, surface features will become 3D-like, leading to the absence of oscillatory behavior in the RHEED signal after the initial drop in intensity, and giving rise to the aforementioned, spotty RHEED patterns. Most growth patterns, however, are a combination of both layer-by-layer and island growth, called (Stranski- Krastanov mode). In such a case, the interlayer diffusion is limited due to limitations in surface mobility, resulting in nucleation on top of 2D islands before a UC is completed. During growth, the nucleation and insertion of adatoms at step edges happens at an increasing number of UCs, represented by an exponential dampening of the RHEED oscillations [144] (Fig. 3.5).

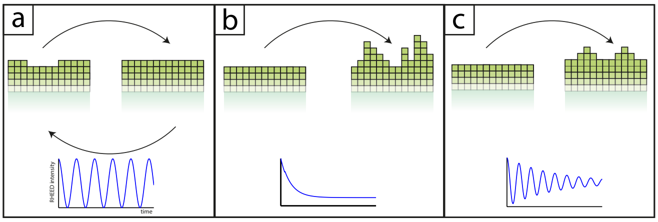

Figure 3.5: **(a)** Layer-by-layer (Frenk-Van der Merve) growth: cyclic process in which the growth of the next layer only starts when the layer before is completed. The RHEED intensity follows a similar behavior, i.e. the maximum intensity appears only when the new layer initiates. The increased adatom density leads to an increased roughness, and hence a decrease in specular beam intensity. The beam intensity recovers when the layer starts to fill up, coupled to a decrease in roughness. **(b)** 3D island growth: process in which rapid coarsening of the surface takes place, leading to the absence of oscillatory behavior in the RHEED intensity. The intensity also drops, coupled to an increased roughness of the surface, enhancing the destructive interference in the specular beam. **(c)**Stranski-Krastanov growth: a process in which the film grows both layer-by-layer and 3D island-like, leading to a dampening in the amplitude of the RHEED oscillations.

3.1.3 Pulsed laser interval deposition

The problem of coarsened surfaces presented by the Stranski-Krastanov growth mode could be easily circumvented by lowering the oxygen background pressure or increasing the deposition temperature. For cuprates, however, these parameters have to be fixed to ensure phase stability. Consequenty, other methods have been tried to manipulate growth. One such method is the Pulsed Laser interval Deposition (PLiD) [144], whereby the interlayer diffusion is optimized due to a decrease of the average island size. This, in turn is connected to increasing the number of nucleation sites by drastically increasing the ablation frequency to accommodate for the exact amount of material needed to complete a UC in a time interval comparable to the relaxation time. This is typically < 1 s at the typical deposition temperatures used for $La_{2\text{-}x}Sr_xCuO_4$, $Nd_{2\text{-}x}Ce_xCuO_4$ and $YBa_2Cu_3O_{7\text{-}\delta}$. The short-lived interval of deposition is followed by an interval of relaxation for the purpose of recrystallization. This is coupled to the rearrangement of the material, leading to a flatter surface, which in turn provides a more suitable surface for the layer-by-layer growth of the sequential UCs (Fig. 3.6). For the work done in this thesis, the PLiD technique has been used to stimulate 2D layer growth.

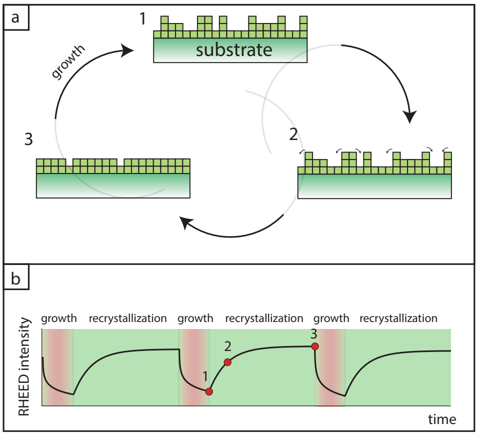

Figure 3.6: **(a)** Pulsed laser interval deposition makes use of the principle of growth interruption. At non-optimal deposition parameters, the growth of a certain amount of material deposition leads to some roughening of the surface (1), which is accompanied by a decrease of the RHEED signal **(b)**. The growth is then interrupted to allow for recrystallization of the film material (2). Eventually, the surface becomes less rough, corresponding to an increased RHEED signal (3). The flatter surface makes a suitable substrate for the next deposition session.

3.2 Pulsed laser deposition setup

All thin films were fabricated in the Thin Film Laboratory at the University of Twente, The Netherlands, using the PLD system. The laser source is KrF excimer-based (Lambdaphysik LPX 210), and has a wavelength of 248 nm, which lies in the range of wavelengths where most metaloxides have their maximum in absorption.The width of the laser pulse is 25 ns. A mask is used to select the middle part of the laser beam, which is then focused on the target substrate with a lens. The focused beam goes into to the main chamber of the PLD system and ablates the target, which serves as the evaporation source. Both the target and the heater (on which the substrate is glued) are brought in the main chamber via the load lock. Any misalignment is compen- sated by the wobble stick. The heater x, y, z, rotation and azimuth are used to move the heater to its correct position in the chamber. Before deposition starts, the top surface layers of the target material is ablated to remove contaminations. The ablated material hits a shutter instead of the substrate. After this process, the substrate is heated to the deposition temperature, while being in the desired deposition pressure of either Ar, O_2 or O_3. While depositing, the RHEED gun (electron energy of 35 keV) is aimed at the surface with an incident angle of 1 degree. The refracted electron beams are picked up by a fluorescent phosphor screen near the substrate, and is shielded from ablation plumes to reduce contamination. The heater can be rotated in order to adjust the angle of incidence of the electron beam on the substrate. The azimuthal angle can be changed by additional rotation of the heater. A CCD camera monitors the diffraction pattern (Fig. 3.7).

3.3 Growth of thin cuprate films

There are several requirements for achieving a giant proximity effect (GPE) in the *ab*-axis through ionic liquid (IL) gating. As GPE involves pseudogap physics, the first requirement is that the junction area in the *ab*-plane is in its pseudogap phase, while the leads have to be in the superconducting phase. In other words, ΔT_c has to be as high as possible. To achieve this, the junction area $T_{c'}$ has to be as low as possible, while the lead area T_c should be maximized. The former $T_{c'}$ is to be adjusted by means of the Sr and oxygen doping of the film, substrate-film interlayer coupling, and film thickness. The latter T_c is maximized by means of IL gating. We use a solid barrier to separate both the junction and lead areas from IL gating.

3.3.1 Certain considerations for lowering the T_c

In this section, the factors involving lowering the junction $T_{c'}$ are treated. An obvious factor in influencing the $T_{c'}$ of the junction area is the chemical doping of Sr and oxygen of $La_{2\text{-}x}Sr_xCuO_{4+\delta}$. As the bulk

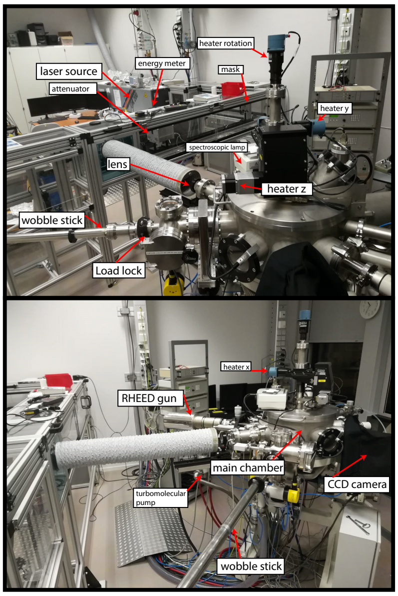

Figure 3.7: The PLD-RHEED system at the Thin Film Laboratory at the University of Twente.

Mott-insulator parent compound is doped, the La^{3+} is replaced by the less positively charged Sr^{2+}. To counteract for this, holes are formed. From $x = 0$ to $x = 0.05$, the properties of an antiferromagnetic Mott-insulator are present. For $0.05 < x < 0.25$ superconductivity appears, with a maximum bulk value of $T_c = 40$ K. For $x > 0.25$, a Fermi liquid behavior is seen [145]. Similar to Sr doping, oxygen overdoping ($\delta > 0$) leads to additional O^{2-} in the UC, which effectively hole dopes the cuprate, and can lead to superconductivity even in the parent compound La_2CuO_4 [146]. Oxygen underdoping ($\delta < 0$) has the opposite effect of effective electron doping and can induce antiferromagnetism in nominally superconducting $La_{2\text{-}x}Sr_xCuO_{4+\delta}$ films [147].

Another factor that one can make use of is the fundamental role of interlayer coupling between substrate and film, as it is known that interlayer coupling can play a similar, if not a stronger role in applying an in-plane pressure on the CuO_2 planes [148]. 'Epitaxial pressure' has been successfully applied at $HgBa_2Ca_2Cu_3O_{8+\delta}$ [149], raising the T_c from 133 K to 164 K. In the case of H_2S, hydrostatic pressures of

155 GPa were used to reach a T_c of 203 K, the highest ever reached as of yet [150]. In the case of $La_{2\text{-}x}Sr_xCuO_4$, interlayer coupling through compressive strain leads to a T_c as high as 49 K [148]. In our case, however, the goal is not to achieve a maximum T_c but a T_c that is as low as possible while still remaining in the pseudogap phase.

For heteroepitaxial growth of films, the UCs nearest to the interface are strained to accommodate to the lattice mismatch present. As the film thickness is increased, the strain is relaxed as the film thickness increases. The number of UCs that are needed to achieve this state depends on the substrate used. Hence, the film thickness dependence of the in-plane pressure induced by the lattice mismatch can be used to change the T_c of the film. In the case of $La_{1.85}Sr_{0.15}CuO_4$ ($a = 3.78$ Å), films grown on $LaSrAlO_4$ ($a = 3.76$ Å) have shown that a thickness of 500 Å is enough to achieve the same T_c as the bulk value [151], while for those grown on $SrTiO_3$ ($a = 3.91$ Å), thicknesses in the order of 3000 - 4000 Å are required to maximize the T_c [152]. For our purposes of lowering T_c, superconductivity is reported for thin films (2 UC, 26 Å, or more) of $La_{1.85}Sr_{0.15}CuO_4$ grown on $LaSrAlO_4$ [153], while the growth of $La_{1.85}Sr_{0.15}CuO_4$ on $SrTiO_3$ is reported to have superconductivity for films having a thickness of 30 UC, 400 Å, or more [152]. Another important note to be made is that changing the Sr or oxygen doping of the film can change the minimum thickness needed to achieve superconductivity considerably [152].

3.3.2 Substrate choice

$La_{2\text{-}x}Sr_xCuO_{4+\delta}$ has a pseudotetragonal structure with an in-plane lattice constant of 3.78 Å. For epitaxial film growth, its substrate coun- terpart should be having a comparable lattice constant as well. There are several possibilities, such as $(LaAlO_3)_{0.3}(Sr_2AlTaO_6)_{0.7}$ (+2.4 %), $LaSrAlO_4$ (-0.5 %), and $SrTiO_3$ (+3.4 %). Using the latter substrates leads to tensile strain in the grown films. The former substrate would lead to compressive strain. Although $SrTiO_3$ has been used as a substrate for $La_{2\text{-}x}Sr_xCuO_4$ growth [81], it can easily become conducting during processing, such as argon ion etching. For this reason, this substrate is not preferred. The substrate $(LaAlO_3)_{0.3}(Sr_2AlTaO_6)_{0.7}$ does not become conducting after etching processes, and is hence usable. An added benefit is that the Czochralski growth of the source crystals of $(LaAlO_3)_{0.3}(Sr_2AlTaO_6)_{0.7}$ generally yields a cleaner material with less defects than the flame fusion

(Verneuil) growth of $SrTiO_3$. The substrate material $LaSrAlO_4$ is the most suitable for layer-by-layer growth and maximizing the T_c of due to compressive strain induced in $La_{2-x}Sr_xCuO_4$ [152, 154]. The effect of mismatch in lattice parameters can be seen in the specular beam intensity characteristics (Fig. 3.8a). The growth of $La_{2-x}Sr_xCuO_4$ on $LaSrAlO_4$ compared to that on $(LaAlO_3)_{0.3}(Sr_2AlTaO_6)_{0.7}$ shows that RHEED oscillation amplitude is conserved for a longer time, until the 30^{th} UC. For $(LaAlO_3)_{0.3}(Sr_2AlTaO_6)_{0.7}$, however, the transition to a 3D growth mode typically happens at around the 10^{th} UC.

The $(LaAlO_3)_{0.3}(Sr_2AlTaO_6)_{0.7}(001)$ substrate is annealed at a temperature of 1050 C for 10 h under an O_2 flow of 150 ml/min. This results in clear steps on the surface, the average terrace width of which coincides with the miscut angle of the surface. The height difference between nearest neighbour terraces is 3.4 Å, which corresponds to the cubic UC parameter of $(LaAlO_3)_{0.3}(Sr_2AlTaO_6)_{0.7}$. This is an indication that the surface is mainly single terminated, as is confirmed in other reports which mention that more than 90 % of the surface belongs to the $AlO_{2-\delta}/TaO_{2-\delta}$ termination after an annealing procedure [155] (Fig. 3.8c). In the case of $LaSrAlO_4(001)$, an annealing treatment is not essential in achieving 2D layer growth [10, 156], while some reports do mention annealing treatments for the growth of $SrRuO_3$ [157] or $YBa_2Cu_3O_7$ films [158]. It must be noted that most of our $LaSrAlO_4$ have not been annealed, while those that were, were exposed to an annealing procedure at 1050 C for 10 h under an O_2 flow of 50 ml/min. Such an annealing procedure gives rise to a surface of double termi- nation, as is seen in (Fig. 3.8c). This is evident from the step heights equaling half the c axis lattice parameter (6.3 Å) of $LaSrAlO_4$.

The smaller in-plane lattice parameter of $LaSrAlO_4$ also has an effect on the superconducting properties of the film. As expected, the compressive strain leads to the film being on the verge of superconductivity for $x = 0.05$. For $(LaAlO_3)_{0.3}(Sr_2AlTaO_6)_{0.7}$, the doping has to be increased to 0.07 to get the same characteristics (Fig. 3.8b) due to substrate-film interlayer stress.

3.3.3 $La_{2-x}Sr_xCuO_{4+\delta}$ growth

$La_{2-x}Sr_xCuO_4$ films are grown at 740 C by means of pulsed laser deposition with an energy density of 1.3 - 1.65 J/cm^2, spot size of 1.36 mm^2, and a repetition rate of 1-4 Hz in an O_2 atmosphere ($p_{O_2} \approx 1.3\times10^{-1}$

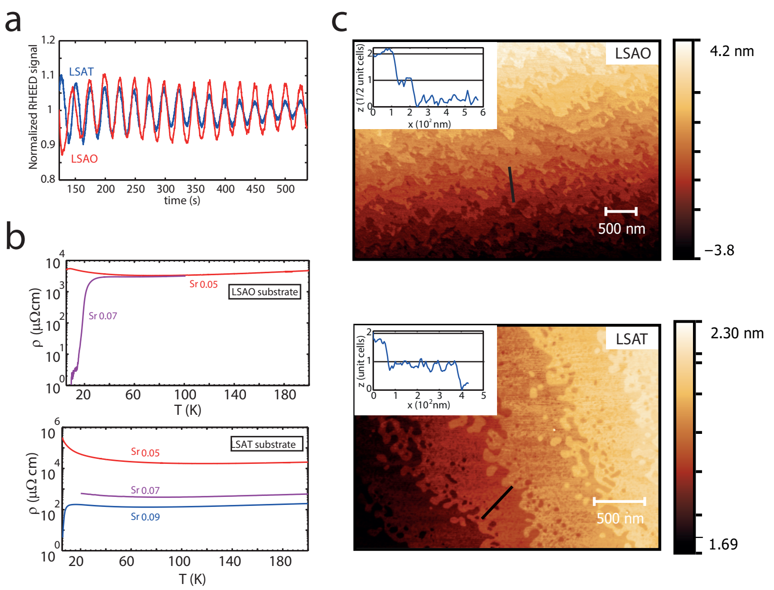

Figure 3.8: **(a)** Normalized RHEED signal vs. time for $La_{1.95}Sr_{0.05}CuO_4$ growth on $LaSrAlO_4$ (LSAO) and $(LaAlO_3)_{0.3}(Sr_2AlTaO_6)_{0.7}$ (LSAT). The RHEED oscillation amplitude in the former case is preserved over a substantially larger amount of oscillations than in the latter case. **(b,top)** $\rho(T)$ characteristics for different levels of Sr doping of a 30 UC film grown on $LaSrAlO_4$. For $x = 0.05$ the film is on the verge of being a superconducting at 4 K. Increasing the doping to $x = 0.07$ induces a superconducting transition, with a $T_{c,mid}$ of 20 K. When grown on $(LaAlO_3)_{0.3}(Sr_2AlTaO_6)_{0.7}$ (b,bottom), former two doping levels are insufficient to induce a superconducting transition, for which a doping of $x = 0.09$ is needed. **(c,top)** Atomic force microscopy (AFM) scan of an annealed surface of $LaSrAlO_4$, which has double termination. Inset: the steps indicate that the height difference between the next-neighbour terraces is equal to $\frac{1}{2}\times c$-axis lattice parameter of $LaSrAlO_4$, namely 6.3 Å. Annealed $(LaAlO_3)_{0.3}(Sr_2AlTaO_6)_{0.7}$ **(c,bottom)** typically shows full UC steps of 3.4 Å.

mbar). The target-substrate distance is kept at 47 mm, at which on average 95 pulses were needed to complete one UC, comparable to previous reports [81], as is monitored by means of RHEED (see Fig. 3.9). After deposition, the sample is kept at the deposition temperature and pressure for 15 minutes. Then, the O_2 pressure in the chamber is increased to 1 bar. This atmosphere is used to anneal the sample for 15 minutes at 600 C and 30 minutes at 450 C, while maintaining a cooldown rate of 10 K/min. The oxygen annealing are meant to give the $La_{2\text{-}x}Sr_xCuO_4$ films the correct oxygen stoichiometry, i.e. δ =0.

By adjusting the annealing times, one can either overdope ($\delta > 0$) or underdope ($\delta < 0$) the film. We have hence used oxygen doping, along with Sr doping, as means of influencing the T_c of the film [81, 147]. Table 3.1 lists some of the film properties and deposition parameters for samples with a finite T_c.

Sample number	Substrate	x	d (UC)	t at 600 C (min.)	t at 450 C (min.)	$T_c(R = 0)$ (K)
LSCO45	LSAO	0.07	13	15	30	5.7
LSCO47	LSAO	0.07	10	15	20	1.5
LSCO48	LSAO	0.07	10	15	20	3.9
LSCO57	LSAT	0.09	30	15	30	3.5
LSCO58	LSAT	0.09	30	15	30	1.0
LSCO61	LSAT	0.09	30	15	30	3.5
LSCO62	LSAT	0.09	30	15	30	2.9
LSCO64	LSAT	0.09	30	15	30	4.0
LSCO66	LSAT	0.09	30	15	30	2.0
LSCO69	LSAT	0.09	30	15	30	5.5
LSCO74	LSAT	0.09	30	15	30	1.0
LSCO80	LSAT	0.09	30	15	30	5.1

Table 3.1: List of samples having an initial T_c used for the purpose of investigating the giant proximity effect by means of IL gating. Other parameters include the substrate type $(LaAlO_3)_{0.3}(Sr_2AlTaO_6)_{0.7}$ (LSAT) or $LaSrAlO_4$ (LSAO), film thickness d, annealing times t at 600 and 450 C.

3.3.4 Growing highly crystalline $La_{2-x}Sr_xCuO_4$ films

The crystallinity of the surface is key in acquiring the optimal electrostatic charge transfer in the film, as was found in IL gated FeSe films [92]. The layer-by-layer growth of $La_{2-x}Sr_xCuO_4$ can be optimized using a metallic buffer layer, based on the recipe used by Bozovic *et al.* [10, 64]. The advantage of this metallic buffer layer is the intrinsic offset in lattice parameters of $LaSrAlO_4$ and $La_{2-x}Sr_xCuO_4$ and a difference in thermal expansion coefficients ($\alpha = 8.5 \times 10^{-6}K^{-1}$ for $La_{2-x}Sr_xCuO_4$ and $\alpha = 10.5 \times 10^{-6}K^{-1}$for $LaSrAlO_4$) that lead to a crossover of lattice constants at typical growth temperatures happens at a doping level of $x = 0.40$-0.45 [148]. The perfect match in the lattice constants of both the $LaSrAlO_4$ substrate and buffer film in turn provides excellent growth conditions for subsequent layers, as has been shown before in Ref.10.

The unbuffered film follows the double termination of the $LaSrAlO_4$ substrate surface (fig. 3.10a), which results in the formation of grain boundaries at the terraces (fig. 3.10b). This is confirmed by the broad-

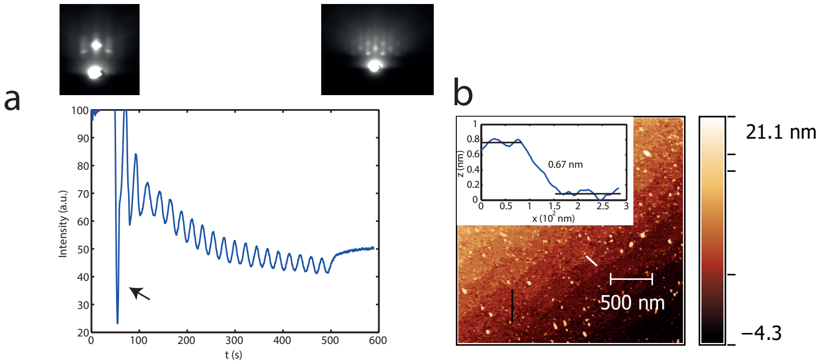

Figure 3.9: **(a)** RHEED signal vs. time for $La_{1.95}Sr_{0.05}CuO_4$ layer-by-layer growth on a non-annealed $LaSrAlO_4$ substrate, showing clear RHEED oscillations of half UC monolayers until the end of the deposition. The arrow indicates a manual increase in the beam intensity. The left and right insets show the RHEED patterns of the $LaSrAlO_4$ substrate, and of the resulting film, respectively. The final RHEED pattern appears to have extra spots next to the clear two-dimensional spots, indicating surface roughening and a transition to 3D growth. **(b)** AFM image of a 10 UC thick layer-by-layer grown $La_{1.95}Sr_{0.05}CuO_4$ film on $LaSrAlO_4$. The inset shows a step height of 6.7 Å, which is half the c axis lattice parameter of the substrate $LaSrAlO_4$, indicating layer-by-layer growth. The surface roughness is comparable to the initial substrate roughness, 4.0 Å.

ened 2D RHEED patterns, indicative of a domained surface, as is discussed in Section 3.1.2. In contrast, the insertion of a $x = 0.30$ buffer layer (due to a lack of target availability of a higher Sr doping) leads to atomically flat terraces, not containing grain boundaries and hence are not influenced by the double termination (fig. 3.10). After growth, the 2D RHEED spots are still clearly visible, indicating a crystalline, 2D surface. The crystalline quality of the films resemble the molecular beam epitaxy grown $La_{2-x}Sr_xCuO_4$ of Bozovic *et al.* [10]. Another observation is that the amount of pulses (i.e. 90) typically needed to complete the first UC of the $x = 0.30$ buffer layer is significantly higher than the pulses (i.e. 81) needed in the subsequent layers. Combined with the previous observation of flat terraces, it could be assumed that the mixed termination at the surface of $LaSrAlO_4$ containing AlO_2/(Sr,La)O, is not equally distributed at the terrace, but is dominant (∼70-80%/20-30%) in one of the two terminations. We hence suspect that the initial extra pulses needed for the completion of the metallic buffer layer involves the filling up of the non-dominant

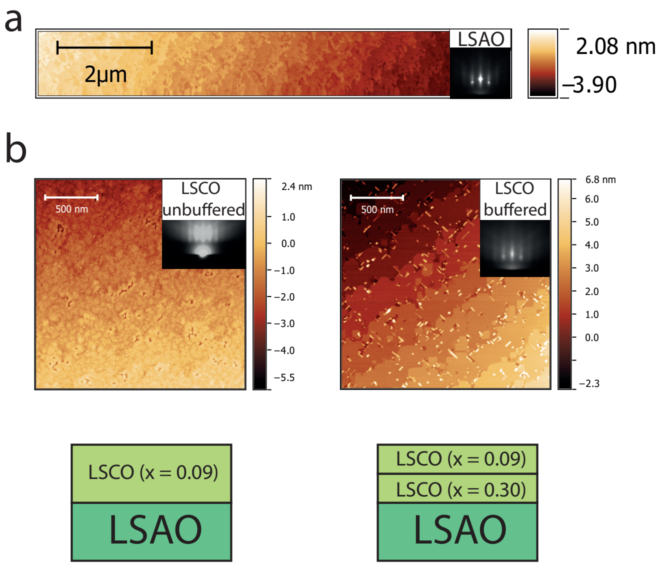

Figure 3.10: **(a)** Shows a typical AFM image of a double-terminated $LaSrAlO_4$ (LSAO) surface. The terminations of AlO_2 and (Sr,La)O are not equally distributed, but is dominant (∼70-80%/20-30%) in one of the two terminations. **(b)** The AFM images of an unbuffered and buffered $La_{2-x}Sr_xCuO_4$ (LSCO, $x = 0.09$) film. Here, the buffered film is grown on a metallic $x = 0.30$ layer of 1 UC thick. Both films have the same total thickness, in this case 7 UC. The morphology of the unbuffered films follow the double-termination of the substrate, and is hence characterized by a domained surface. This is in line with the typical broadening observed in the 2D RHEED spots, which, as discussed in Section 3.1.2, is an indication of a domained surface. In contrast, the enhanced crystalline quality of the buffered films is accompanied by the absence of grain boundaries and a domained surface, as is accompanied by clear 2D RHEED spots.

termination.

The transport properties of the layers grown with and without a metallic buffer layer tend to be different as well. Without a metallic buffer layer, the strain effects result in a semiconducting behavior, as is seen for the films of 7 UC (fig. 3.11a). Insertion of a mere 1 UC buffer layer changes the transport properties completely and superconducting transition temperatures higher than those for bulk can be observed (fig. 3.11a and b).

It is unlikely that the high T_c is caused by an overdoping of oxygen

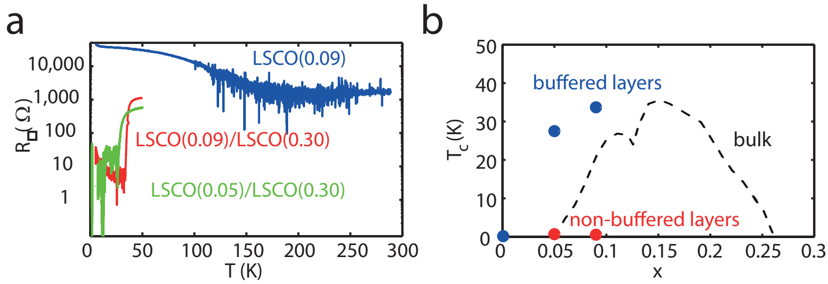

Figure 3.11: **(a)** $R(T)$ curves of various doping levels of $La_{2\text{-}x}Sr_xCuO_4$ (LSCO) of a total thickness of 7 UC. The unbuffered film shows the expected semiconducting behavior, while the insertion of a buffer layer of 0.30 leads to superconductivity. The doping levels are parenthesized. **(b)** The T_c values induced in the buffered films are much higher than attainable in the non-buffered films, or bulk material.

in the buffered films, as the recipe used during deposition is meant for optimal stoichiometric oxygen content. In theory, cation intermixing could occur [159] over distances of at most 1 UC and would give a maximum T_c for the $La_{1.7}Sr_{0.3}CuO_4/La_2CuO_4$, as the interface would then be optimally doped. This, however, is not observed.

One likely scenario is that of strain, based on the observation that a films of 3 UC or less do not become superconducting. At the same time, this shows that the large T_c cannot be caused by the $x = 0.30$ layer itself.

Another scenario deals with the preformed pairs interpretation of the pseudogap phase. In this picture, the electron pairing in the $x = 0.09$ layer cannot lead to superconductivity due to a lack of phase coherence, as the superfluid density is too low [32]. The proximity of the $x = 0.09$ layer to the phase coherent, metallic $x = 0.30$ layer then should effectively lead to a phase coherence in the $x = 0.09$ layer as well, leading to an increase in T_c. Interestingly, similar observations have been made with experiments concerning similar metallic and underdoped $La_{2\text{-}x}Sr_xCuO_4$ bilayers [23]. A future study would be needed for a more thorough investigation of these T_c raising effects in bilayers, and their relationship to the giant proximity effect.

3.4 $Nd_{2\text{-}x}Ce_xCuO_{4\text{-}\delta}$ growth

The electron doped cuprate $Nd_{2\text{-}x}Ce_xCuO_{4\text{-}\delta}$ is part of the family of electron-doped superconductors of the 214-system $Re_{2\text{-}x}Ce_xCuO_{4\text{-}\delta}$ with Re = Nd, Pr, La, Sm, Eu, or Gd. Just like its hole-doped counterpart $La_{2\text{-}x}Sr_xCuO_{4+\delta}$, the superconductivity depends on both its second rare-earth element, Ce(x), and oxygen content. The maximum T_c appears at Ce = 0.15 and $\delta = 0.04$, pointing to the fact that $Nd_{2\text{-}x}Ce_xCuO_4$ has to be oxygen reduced. For this, an in-situ post-annealing treatment in vacuum is done at 750 C for 8 minutes at a pressure of 1×10^{-7} mbar. $Nd_{2\text{-}x}Ce_xCuO_4$ has an in-plane lattice parameter of 3.95 Å, for which $SrTiO_3$ (+0.9 %) as a substrate would be most suitable for heteroepitaxial growth. However, because of the possibility of inducing oxygen vacancies during processing, we decided to use the larger mismatched annealed $(LaAlO_3)_{0.3}(Sr_2AlTaO_6)_{0.7}$ as a substrate (+2.0 %). To compensate for the stress induced by the larger mismatch of the $(LaAlO_3)_{0.3}(Sr_2AlTaO_6)_{0.7}$ substrate, undoped buffer layers have been used to release stress in the doped top layers, similar to bilayer concepts used in other works [10, 81, 154]. During deposition, the oxygen background pressure is 0.25 mbar, the sample temperature is 820 C, while the target-substrate distance is held at 52 mm. Furthermore, the laser fluence is 1.2 J/cm^2 while maintaining a repetition rate of typically 1-4 Hz. Occasionally, growth interruption was applied to stimulate layer-by-layer growth. When monitored with RHEED, only a few oscillations are observable initially, suggesting a limited 2D growth mode, quickly followed by 3D island growth, as is suggestive by the spotty RHEED patterns. When checked by AFM, the surface suggests island growth (Fig. 3.12), as has been seen before in $Nd_{2\text{-}x}Ce_xCuO_4/SrTiO_3$ films [160] and heteroepitaxial growth of other cuprates, such as $YBa_2Cu_3O_{7\text{-}\delta}$ [161].

3.5 Contact resistance and barrier characterization

The contact resistance $I(V)$ characteristics show non-linearity in the case Ti is sputtered ex-situ on $La_{1.95}Sr_{0.05}CuO_4$ (20 UC) as a wetting layer before Au deposition, indicating a non-Ohmic contact (see Fig. 3.13). The interface between a metal and a p-type semiconductor can form a Schottky-type barrier if the work function of the metal

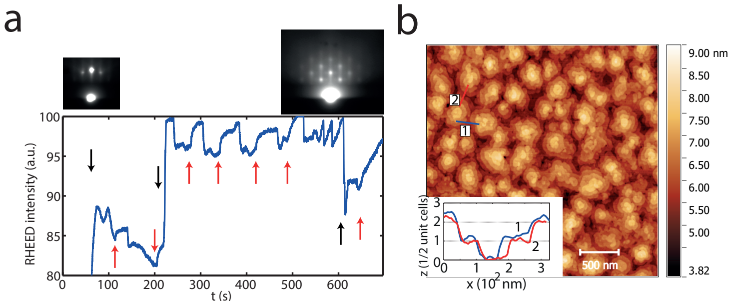

Figure 3.12: **(a)** RHEED signal vs. time for $Nd_{1.95}Ce_{0.05}CuO_4$ growth on an annealed $(LaAlO_3)_{0.3}(Sr_2AlTaO_6)_{0.7}$ surface. The black and red arrows represent manual augmentation of the beam intensity, and growth interruption, respectively. The RHEED data in between the arrows show slight oscillatory behavior, typical of the island-like growth exhibited by $Nd_{1.95}Ce_{0.05}CuO_4$. The initial substrate surface of annealed $(LaAlO_3)_{0.3}(Sr_2AlTaO_6)_{0.7}$ shows clear two-dimensional spots, while the spotty behavior of the RHEED pattern after growth is another indication of the presence 3D islands. **(b)** The AFM image of a 30 UC thick $Nd_{1.95}Ce_{0.05}CuO_4$film on $(LaAlO_3)_{0.3}(Sr_2AlTaO_6)_{0.7}$, the surface of which is island-like. The inset shows height steps corresponding with half the c axis lattice parameter of $Nd_{1.95}Ce_{0.05}CuO_4$, 6.5 Å.

is larger than that of the semiconductor. Since $La_{2\text{-}x}Sr_xCuO_4$ is a p-type conductor and has a relatively large work function (5.06 eV for Sr 0.05 doping) [162], most metals like Ti (4.33 eV) do not form an Ohmic contact with the cuprate. The contact is worsened by the fact that Ti can draw away oxygen from the cuprate, as it is prone to form TiO_2. Oxygen-deficient $La_{2\text{-}x}Sr_xCuO_4$ can lose its superconductive properties, hence rendering such a sample unusable. Exposure to air during transport from the PLD setup to the sputtering setup can either cause an adsorbate layer to form on the cuprate, or can cause the CO_2 and H_2O in the air to react with the top layer [163], causing a so-called dead layer. The $I(V)$ curve can be fitted using a polynomial of the form $I(V) = \alpha V + \gamma V^3$, based on Simmons model for metal/insulator/metal junctions for low voltages [164]. Here, J is the current density $\alpha = A\left(\frac{e}{h}\right)^2 \frac{\sqrt{2m_e\phi}}{d} e^{-\beta\sqrt{\phi}}$, and $\frac{\gamma}{\alpha} = \frac{(\beta e)^2}{96\phi} - \frac{\beta e^2}{32\sqrt{\phi}}$. Here, A, e, h, m_e represent the metal/insulator/metal junction contact area, the electron charge, Planck constant and the electron mass. Furthermore, ϕ is the average barrier height across the barrier thickness d, while $\beta = 4\pi A\sqrt{2m_e}d/h$. The fitparameters d and ϕ correspond to 1.1

nm and 0.61 eV. These numbers roughly correspond to the thickness of the Ti adhesion layer (1-2 nm), and the difference in work function of Ti and $La_{2\text{-}x}Sr_xCuO_4$ (0.73 eV).

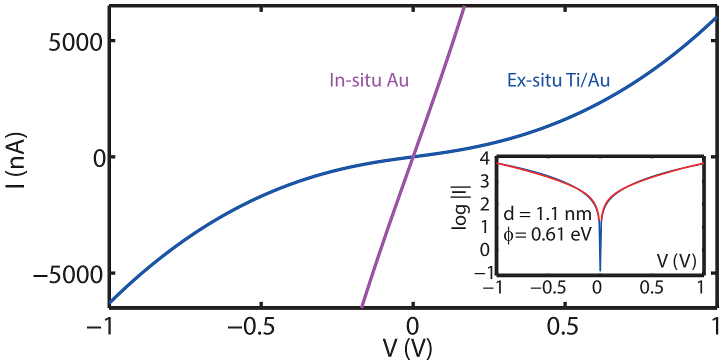

Figure 3.13: Two-point $I(V)$ curves for $La_{1.95}Sr_{0.05}CuO_4$ (20 UC) for which the contacts were applied by means of ex-situ Ti/Au (blue) and in-situ Au (purple) deposition. Inset: log|I| plot for the Ti/Au contacts. The fitparameters are based the Simmons model, corrected for the junction contact area of Ti to $La_{2\text{-}x}Sr_xCuO_4$ (approx. 1 mm^2)

The barrier has an insulating behavior when cooled down to low temperatures, and typically rendered the sample unmeasurable below 100 K. To counter this problem, we have tried sputtering without Ti adhesion layer, as Au has a work function that is sufficiently high (5.1 eV) [165]. However, the adsorbate layer formed during ex-situ transporta- tion makes it difficult for Au to adsorb at the surface of the cuprate, resulting in the removal of the sputtered Au during the lift-off process. We solve this by depositing Au in-situ by means of PLD, following the cuprate deposition. As the Au covers the whole substrate, structuring the sample to expose the $La_{2\text{-}x}Sr_xCuO_4$ surface for ionic liquid gating should involve removing the parts of the Au. This can be done by Ar ion etching, as is done by [10]. This is cumbersome, and can risk damaging the cuprate layer, and removing oxygen from its lattice structure, rendering it non-superconducting. Using a $KI/H_2O/I_2$ solution in 4:1:40 mass ratio induces a ionization reaction of Au, which subsequently dissolves in the solution, but leaving the $La_{2\text{-}x}Sr_xCuO_4$ layer intact. Compared with the non-linear $I(V)$ characteristic of ex-situ deposited Ti/Au, the typical $I(V)$ characteristic of samples prepared with in-situ Au deposition is nearly perfectly linear and metallic.

3.6 Methods related to ionic liquid gating

As described in Chapter 2, the electric double layer concept of IL gating has major advantages when compared to standard oxide field effect transistors. However, ILs can be contaminated quickly, as impurities from the air such as H_2O and O_2 easily dissolve in the IL, even in hydrophobic ones. These molecules are electroactive and affect gating performance, and their removal from the IL is essential before any voltammetric measurement. The electroactive nature of H_2O and O_2 shift the cathodic (anodic) limiting potential of the sample towards the positive (negative) potential, essentially limiting the electrochemical window (EW) of the IL.

Hence, the partial pressure of these molecules has to be minimized. For this, in our experiments we developed the practice that the bottle in which the IL is kept, is stored in a N_2 atmosphere of a glove box, while the IL interaction time with ambient air is kept at a minimum, typically a minute or so. Furthermore, with the sample in place the IL is vacuum dried at pressures varying between 1×10^{-5} and $\times10^{-6}$ mbar for 15 minutes or more, making p_{O_2} and p_{H_2O} in the order of $\times10^{-7}$ mbar.

Yet another way of optimizing IL gating of a material is to have its surface free of contaminations as much as possible. If the surface is contaminated with residuals from structuring processes, a barrier between the IL and the material surface is formed, effectively increasing the electric double layer distance, and hence the field effect induced. Before any gating experiments, the surface of the material is cleaned by an alcohol wetted lens tissue or by means of irradiation with UV light from a mercury lamp under air. The 184.9 nm wavelength generated by the lamp is adsorbed by oxygen, leading to generation of ozone, while the 253.7 nm wavelength is adsorbed by ozone. Hence, ozone is continually formed and destroyed, an intermediate product of which is atomic oxygen. Atomic oxygen is a strong oxidizing agent, which reacts with the molecules that originate from any process residuals, such as PMMA or photoresist. This process, can give clean surfaces without affecting the oxygen doping of the cuprate itself. We have observed no changes in superconducting properties of $La_{2-x}Sr_xCuO_4$ films for illumination times as long as 90 minutes. Although the oxygen concentration in the $La_{2-x}Sr_xCuO_4$ films can also be modified by the ozone exposure, this requires the treatment to be done at elevated temperatures [113].

3.7 Introducing an *ab*-axis Josephson junction

To prevent the junction area from being gated along with the lead areas, a barrier is necessary. The barrier needs to fulfill a number of requirements. Firstly, the barrier should be insulating, so no parallel conduction path is formed. Secondly, IL gating across the barrier should not influence the layer below it electrostatically. For this, the induced charge carrier density in the layer beneath has to be minimized, defined as

$$\sigma = \int_0^{V_g} \frac{\epsilon_0 \epsilon_I(V)}{d} dV \tag{3.1}$$

Here, ϵ_0 is the dielectric constant of free space, ϵ_I is the dielectric constant of the insulator, d is the thickness of the insulator, and V_g is the gate voltage. To minimize σ, the main parameter that can be tweaked is d, which has to be maximized. As the electric double layer separation in IL gating experiments is typically 1 nm [122], if the barrier thickness is added to this separation, the field effect can quickly become negligibly low. In contrast, V_g in theory should be kept at a minimum, but is typically is not kept at a minimum. Furthermore, ϵ_I is preferably kept as low as possible, while not much flexibility exists in this parameter space, as typical oxide insulator materials such as $SrTiO_3$, TiO_2, $(LaAlO_3)_{0.3}(Sr_2AlTaO_6)_{0.7}$, $LaAlO_3$ and Al_2O_3 have a relatively large dielectric constant (310, 170, 22.7, 23.5, ~9, respectively, at room temperature).

Thirdly, the barrier should be electrochemically neutral towards the junction area. In many cases of off-stoichiometric growth of the barrier material, the unbalance is compensated by diffusion of certain species from the junction area to the barrier. As an example, some oxide and nitride barriers such as SiO_2 [81] and SiN_3 tend to influence the oxygen doping of the material when not grown stoichiometrically, leading to unintentional changes in the T_c of $La_{2-x}Sr_xCuO_4$, as the T_c of $La_{2-x}Sr_xCuO_4$ is dependent on its oxygen content. This process is usually a very slow one, making the junction unmeasurable in a time period of an order of a week. Lastly, the barrier should be impermeable to ions, such as oxygen, but also the anions and cations of the ionic liquid. For example, the oxide material $PbBa_2Cu_3O_7$ as a barrier has been proven to facilitate oxygen migration between the cuprate $YBa_2Cu_3O_7$ and ionic liquid [63].

Taking all of these considerations into account, we have chosen to primarily work with Al_2O_3, although, as we will see in Chapters 8 and 9, there are still some issues which make it problematic as a barrier material. Although this material has a large dielectric constant as is mentioned before, the reports of its impermeability to oxygen ion diffusion [63] made it an attractive material to work with. Some reports mention oxygen diffusion from the $La_{2\text{-}x}Sr_xCuO_4$ when Al_2O_3 is grown at elevated temperatures (300 C) in combination with a cooling procedure in 1 bar of O_2 [81]. To limit any such interaction between oxygen in the Al_2O_3 and $La_{2\text{-}x}Sr_xCuO_4$, the deposition of AlO_x is done at room temperature.

Depending on the kinetic energy of the ablated species, pulsed laser deposition growth of AlO_x can lead to a number of morphological phases of AlO_x (see Fig. 3.14a), expressed in $\sqrt{p}d$ in Ref. 166, where p is the oxygen background pressure and d is the target-substrate distance. Provided the kinetic energy is low (high O_2 background pressure, large target-substrate distance, and small laser fluence), the grown AlO_x is open and porous, for which x is close to the stoichiometric value of 1.5. When deposited at 2×10^{-1} mbar of O_2 pressure, $d = 60$ mm and $E = 1.5$ J/cm^2, $\sqrt{p}d$ becomes 0.33 Pa$^{0.5}$m, which is a transitional regime between both ends of the morphology spectrum. As expected, the typical film morphology is relatively coarsened and possibly porous, as shown in the AFM image (see Fig. 3.14b,i). As shown in Fig. 3.14c, the AlO_x layer has little influence on the T_c and general $R(T)$ characteristics of the $La_{2\text{-}x}Sr_xCuO_4$ film. However, because of its possible porous character, it is not recommended for IL gating experiments.

Lowering the background pressure to 1×10^{-2} mbar and minimizing d to 42 mm leads to a substantial increase of the kinetic energy of the incoming species. In this case $\sqrt{p}d = 0.03$ Pa$^{0.5}$ m, which is sufficiently low for dense film growth (see Fig. 3.14). The dense film surface shows the same roughness as the substrate on which it is grown when scanned by AFM, suggestive of a very flat film, to such an extent that the film morphology follows the terrace steps of the $(LaAlO_3)_{0.3}(Sr_2AlTaO_6)_{0.7}$ substrate (see Fig. 3.14b,ii). Although the dense film has a stoichiometric value close to 1 [166], it has little influence on the $R(T)$ characteristics of the $La_{2\text{-}x}Sr_xCuO_4$ film, suggestive of limited oxygen diffusion out of the film. Hence, the inherent dense film properties and its limited influence on $La_{2\text{-}x}Sr_xCuO_4$ make it an ideal barrier material for IL gating.

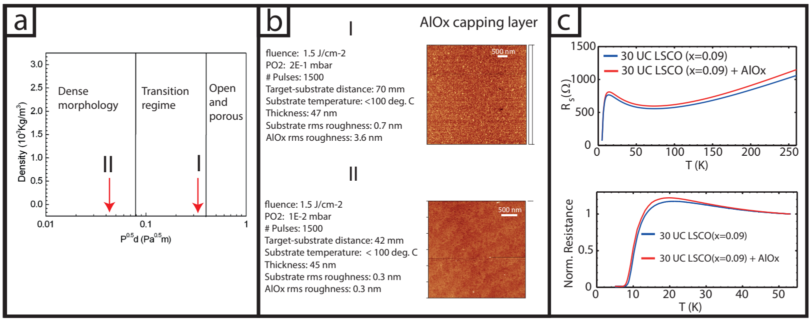

fluence: 1.5 J/cm-2
PO2: 2E-1 mbar
Pulses: 1500
Target-substrate distance: 70 mm
Substrate temperature: <100 deg. C
Thickness: 47 nm
Substrate rms roughness: 0.7 nm
AlOx rms roughness: 3.6 nm

fluence: 1.5 J/cm-2
PO2: 1E-2 mbar
Pulses: 1500
Target-substrate distance: 42 mm
Substrate temperature: < 100 deg. C
Thickness: 45 nm
Substrate rms roughness: 0.3 nm
AlOx rms roughness: 0.3 nm

Figure 3.14: **(a)** Film density vs. $\sqrt{pd}$ for different morphological regimes of AlO_x, based on Ref.166. For high kinetic energy of the incoming particles, the film is dense, whereas an open and porous film is obtained for low kinetic energies. **(b)** AFM images of AlO_x layers I and II grown in the intermediate and dense regime, respectively. Layer I shows a coarsened surface, while layer II shows a flat surface. Both layers I (**c,top**) and II (**c,bottom**) do not affect the $La_{2\text{-}x}Sr_xCuO_4$ substantially in T_c.

3.8 Attaining $SS'S$ junctions by means of etched bilayers

As is mentioned in Section 1.4, obtaining a giant proximity effect through etched bilayers requires a few conditions to be met. Firstly, a $T_{c'}$ should be present in the bottom film, which preferably should be as low as possible. Secondly, the T_c of the top layer should be as high as possible. These requirements are similar to those of the IL-induced giant proximity effect, except that in this case, the T_c difference is already present and is exploited by means of an etched structure. This method allows the top layer to be different than the bottom layer. Hence, bilayers have been made by (1) making use of different Sr levels of $La_{2\text{-}x}Sr_xCuO_4$ and (2) making use of $YBa_2Cu_3O_{7\text{-}\delta}$ as the top layer, while maintaining $La_{2\text{-}x}Sr_xCuO_4$ as the bottom layer. The first type of bilayer is grown as described in Section 3.3.3, and leads to limited ΔT_c. We concentrated most of our efforts in the second type of bilayer, as $YBa_2Cu_3O_{7-\delta}$ is known to have a substantially higher T_c than $La_{2-x}Sr_xCuO_4$ (bulk values of 93 K [133]), with which ΔT_c can be maximized. An etched bilayer sample is made by first growing the bilayer by means of PLD, followed by a electron beam lithography process to define the areas which are to be etched.

The bilayers are grown on $LaSrAlO_4$ substrates to facilitate layer-by-layer growth of the initial, $La_{2-x}Sr_xCuO_4$ layer (see Fig. 3.15a(top)). The deposition parameters of $La_{2-x}Sr_xCuO_4$ are the same as those described in Section 3.3.3. The growth of $La_{2-x}Sr_xCuO_4$ is followed by that of $YBa_2Cu_3O_{7-\delta}$ at a slightly higher temperature and oxygen background pressure, 780 C and 2.0×10^{-1} mbar, respectively. Growing $YBa_2Cu_3O_{7-\delta}$ at a slightly lower temperature of 720 C stimulates a-axis growth of $YBa_2Cu_3O_{7-\delta}$, which is unwanted. The laser fluence is 1.3 J/cm^2 with a repetition rate of 1 Hz, while the target-substrate distance is held at 50 mm. As can be seen in Fig. 3.15a(top), the clear oscillations facilitated by a 2D growth mode is dampened considerably with the growth of $YBa_2Cu_3O_{7-\delta}$, suggesting a 3D growth mode. RHEED oscillations are typically unobservable after the completion of the 4^{th} UC, accompanied by a spotty RHEED pattern. The 3D growth is likely to be formed by limited mobility of the ablated material on arrival at the substrate surface [167].

To maintain 2D growth for a maximum amount of time, growth interruption in most bilayers is used after the completion of every UC, as is shown in Fig. 3.15a(bottom). This allows for recrystallization and reversing the coarsening of the surface. With this method, up to the 30^{th} UC can be observed by RHEED. At each laser pulse, the intensity of the specular beam drops, accompanied by the increased disorder on the surface. This is immediately followed by an exponential rise due to recrystallization of the initially disordered material (see Fig. 3.15c). The characteristic time of this process, τ, is the decay time of the adatom density on the terraces, as is determined from the recovery of the RHEED intensity. If we take the diffusion length to be limited by the average terrace size of the used substrate (100 nm for a typical miscut angle of 0.2 degrees), the maximum limit of the diffusion constant $D \approx l_t^2/\tau = 2.9\times10^{-12}$ cm^{2}s, as τ is approximately 35 s. This value is in line with known values for $YBa_2Cu_3O_{7-\delta}$ growth on $SrTiO_3(001)$ substrates [168]. The RHEED patterns typ-

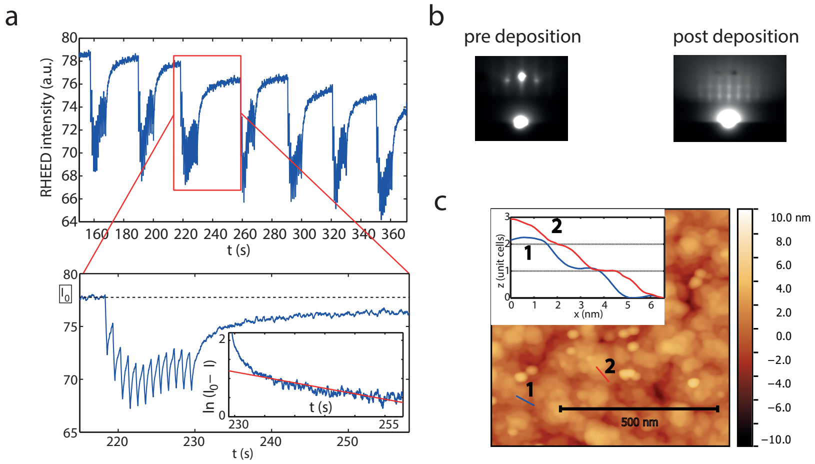

Figure 3.15: **(a)** RHEED vs. time of $YBa_2Cu_3O_{7\text{-}\delta}$ growth using growth interruption after the completion of every UC. After every pulse of the laser, the increased disorder induces a drop in the RHEED intensity, which recovers according to an exponential behavior, representing surface crystallization. The time delay connected to this process is 35 s, which is typical of cuprate films grown at this temperature. **(b)** The initial RHEED pattern of the substrate surface changes and becomes spotty after the growth of 30 UCs of $YBa_2Cu_3O_{7\text{-}\delta}$. **(c)** A typical AFM image of a $YBa_2Cu_3O_{7\text{-}\delta}$ film. The film is coarsened, with individual islands locally showing step heights corresponding to the $YBa_2Cu_3O_{7\text{-}\delta}$ c axis lattice parameter, 11.7 Å.

ically show 3D spots on 2D streaks (see Fig. 3.15a). Although the $YBa_2Cu_3O_{7\text{-}\delta}$ surface is coarsened (the typical roughness is around 1.4 nm, whereas the substrate roughness is 0.3 nm), it is possible to see UC step heights on the surface of the 3D islands (see Fig. 3.15b).

The main parameter with which the T_c of the $YBa_2Cu_3O_{7\text{-}\delta}$ layer is tweaked is the oxygen annealing time at 600 and 450 C, which can vary from 15 to 30 minutes at both annealing temperatures. Table 3.2 gives a summary of the range of thicknesses and T_c's of all bilayers that were used.

The first four $YBa_2Cu_3O_{7\text{-}\delta}/La_{2\text{-}x}Sr_xCuO_4$ bilayers show a low T_c of the $YBa_2Cu_3O_{7\text{-}\delta}$ layer, the bulk value of which is 93 K. These were subjected to a 15 min oxygen annealing at both 600 and 450 C. To test whether this is an inherent growth problem, we grew a single $YBa_2Cu_3O_{7\text{-}\delta}$ layer film of 30 UC on an $LaSrAlO_4$ substrate which was annealed for 30 minutes at both temperatures. The T_c of this

Top layer (2)/Bottom layer (1) (Sample number)	t_1 (UC)	t_2 (UC)	$T_{c,1}$ (K)	$T_{c,2}$ (K)	ΔT_c
LSCO(0.15)/LSCO(0.07) (1)	40	7	5	18	13
YBCO/LSCO(0.15) (2)	20	20	28	38	10
YBCO/LSCO(0.15) (3)	20	30	28	35	7
YBCO/LSCO(0.15) (5)	25	31	21	31	10
YBCO/LSCO(0.15) (6)	25	31	17	59	42
YBCO/LSCO(0.07) (8)	30	30	10	78	68

Table 3.2: List of bilayer parameters: sample number and bilayer composition, thickness, T_c of the top and bottom layers, and the corresponding ΔT_c. The doping levels of $La_{2\text{-}x}Sr_xCuO_4$ (LSCO) are parenthesized. Here, YBCO stands for $YBa_2Cu_3O_{7\text{-}\delta}$.

+

film was 86 K, which is close to the bulk value. Hence, the low T_c is interpreted as the consequence of non-optimal δ in the $YBa_2Cu_3O_{7\text{-}\delta}$ film, presumably caused by an insufficient time for oxygen to diffuse into the film. Hence, the final $YBa_2Cu_3O_{7\text{-}\delta}/La_{2\text{-}x}Sr_xCuO_4$ bilayer is annealed for 30 minutes at both temperatures, and shows an improved T_c , albeit still lower than optimal, but sufficiently high T_c for giant proximity effect studies. As a note, a suppression in T_c of the $YBa_2Cu_3O_{7\text{-}\delta}$ layer can also be caused by interfacial strain effects, as 100 nm thick $YBa_2Cu_3O_{7\text{-}\delta}/La_{2\text{-}x}Sr_xCuO_4$ bilayers show a T_c of 90 K in previous reports [20].

Finally, after fabrication of a resist mask by e-beam lithography, Ar ion bombardment at an acceleration voltage of 350 - 500 V is used to etch away a trench in the top layer at a rate of 6 - 7 nm/min. For this, the PMMA layer used for writing the areas that are to be Ar etched needs to be relatively thick (240 nm). PMMA which has been exposed to Ar ion bombardment tends to change in its properties and is much harder to remove with standard lift-off in acetone and ethanol. Instead, an ethanol wetted lens tissue is used to remove the contaminants.

Chapter 4

On the formation of a conducting surface channel by ionic liquid gating of an insulator

Ionic liquid gating has become a popular tool for tuning the charge carrier densities of complex oxides. Among these, the band insulator $SrTiO_3$ *is one of the most extensively studied materials. While experiments have succeeded in inducing (super)conductivity, the process by which ionic liquid gating turns this insulator into a conductor is still under scrutiny. Recent experiments have suggested an electrochemical rather than electrostatic origin of the induced charge carriers. Here, we report experiments probing the time evolution of conduction of* $SrTiO_3$ *near the glass transition temperature of the ionic liquid. By cooling down to temperatures near the glass transition of the ionic liquid the process develops slowly and can be seen to evolve in time. The experiments reveal a process characterized by waiting times that can be as long as several minutes preceding a sudden appearance of conduction. For the conditions applied in our experiments we find a consistent interpretation in terms of an electrostatic mechanism for the formation of a conducting path at the surface of* $SrTiO_3$*. The mechanism by which the conducting surface channel develops relies on a nearly homogeneous lowering of the surface potential until the conduction band edge of* $SrTiO_3$ *reaches the Fermi level of the electrodes.* [1]

---

[1] The work in this chapter is accepted as: On the formation of a conducting surface channel by ionic liquid gating of an insulator, Hasan Atesci, Francesco Coneri, Maarten Leeuwenhoek, Jouri Bommer, James R. T. Seddon, Hans Hilgenkamp and Jan M. Van Ruitenbeek, *Ann. Phys. (Berlin)*.

4.1 Introduction

The carrier density in materials is the central factor in all electron transport properties. Controlling this carrier density by externally applied gate potentials permits the study of transport and electron-electron interaction effects as a continuous function of this density. Applying an electrostatic potential by means of metallic gates separated by a dielectric from the material under study allows covering only a limited range of carrier densities. Using ionic liquids (ILs) or ionic gels as dynamic dielectrics between the gate and the device gives access to a much wider range of carrier densities [169–171]. When a potential difference is applied across the IL, the entire potential drop is concentrated at the IL/electrode surfaces, where electric double-layers (EDLs) are formed between a sheet of ions of one dominant polarity and a sheet of induced charges just below the surface of the material. These charge layers are separated by a distance as small as 1 nm, thereby producing extremely large electric fields. This makes it possible to induce carrier densities as high as 8×10^{14} cm^{-2} at the liquid/solid interface for a material that is otherwise a deep insulator [169]. These carrier densities are large enough to permit controlling fundamental phenomena such as magnetic order, phase transitions and superconductivity by means of a gate potential. [55, 170, 172–175]

Among the materials used for such studies strontium titanate, $SrTiO_3$, stands out as one of the most widely studied and best characterized systems [176]. It is a band insulator with an indirect bandgap of 3.25 eV, which can be converted into a good conductor at its surface, and even into a superconductor [177]. Disorder plays a role, and at low densities the conductance is best described by variable range hopping and the formation of percolation paths for the electrons in the disorder potential [178]. The origin of this disorder could be intrinsic to $SrTiO_3$ [176], or it may result from density fluctuations in the ionic liquid [179, 180]. The role of the ionic liquid also comes into play when discussing the nature of gating in terms of a purely electrostatic effect, or (partially) as a result of electrochemical modifications of the surface. For sufficiently strong electric fields and field gradients at the interface one should anticipate inducing disorder and chemical modifications at the surface. Indeed, experiments have shown the influence of IL gating on the oxygen content of complex oxides [181–183], while others have shown an unusually high buildup of charges [184], characteristic of induced electrochemical reactions. For the material of interest here, $SrTiO_3$, several reports have given conflicting views on the mechanism of IL gating being either electrochemical [182] or electrostatic [171, 177, 179] in origin.

More recently, the dynamics of the formation of conducting surface channels has received attention from several groups [185–187]. The standard descriptions borrowed from electrochemistry, in terms of homogeneous Helmholtz or Gouy-Chapman layers at the interface with the solid, may not be applicable [186]. A concrete model of the dynamic evolution of a conducting channel was proposed by Tsuchiya *et al.* [185], in terms of a gradual spreading of the conducting channel over the surface of the solid, starting from the source and drain contacts. Here we address this question of how the electric double layer forms on an insulator. We therefore seek to investigate the development and underlying mechanism of conductivity across the surface of $SrTiO_3$ in the time domain. To this end, we slow down the gating process by lowering the temperature at which the gate potential is applied, to temperatures just above the glass transition of the ionic liquid. This allows us to follow the process of gating in time and elucidate the role of the ionic liquid in the process. We were further motivated to investigate the charging dynamics at low temperatures because under such conditions unwanted electrochemical processes are more easily suppressed. Our observations show that, at variance with the interpretation by Tsuchiya *et al.*, [185] the surface conducting channel on $SrTiO_3$ develops homogeneously. The observed time delay of conductance after switching on the gate potential is attributed to the time required for bringing the surface potential to the conduction band edge of $SrTiO_3$. The subsequent evolution of the conductance of the channel is consistent with a percolation description of the two-dimensional electron system.

4.2 Experimental techniques

All of the sample processing was done on pristine undoped $SrTiO_3$ (001) crystal substrates with a miscut angle of < 0.1 degrees, as obtained from Crystec GmbH. The contacts to the $SrTiO_3$ surface were defined by means of photolithography, as is shown in Fig. 4.1a. After development of the photoresist the patches on the surface onto which the electrodes were to be structured were first treated by Ar ion milling

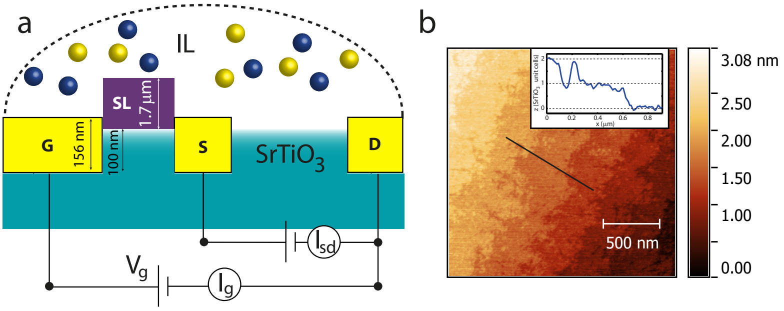

Figure 4.1: **(a)** A schematic cross section of the sample. Yellow and blue spheres represent TFSI(-) and DEME(+) ions, respectively. The gate (G), source (S) and drain (D) electrodes have a thickness of 6 nm Ti plus 150 nm Au. For the areas onto which the Ti/Au layer is deposited, the $SrTiO_3$ is ion milled to about 100 nm depth. The separator layer (SL) is 1.7 μm thick. **(b)** AFM image of a typical $SrTiO_3$ surface after an oxygen plasma treatment. Clear terrace steps can be observed. The inset shows the profile indicated by the black line, showing step heights corresponding to the $SrTiO_3$ unit cell height.

(500 V, 0.4 Pa), such as to ensure low-resistance ohmic contacts between the metal electrodes and the $SrTiO_3$ surface. After this process, layers of 6 nm Ti and 150 nm Au were deposited by sputtering. In order to reduce leakage currents, in a second photolithography step the sample surface was covered by a separator layer (SL) in the form of an insulating photoresist (purple in Fig. 4.1a), except for the electrical contact pads, the gate electrode, and the surface channel area. Chemical cleaning in an oxygen plasma (10 Pa, 13 W) was used for removing any residuals of the photolithographic process on the bare $SrTiO_3$ surface. The resulting surfaces present flat terraces with step heights corresponding to the $SrTiO_3$ unit cell parameter of 0.391 nm, as was verified by atomic force microscopy (AFM), Fig. 4.1b. We have tested patterns defined on the chip consisting of a single channel with multiple contacts, permitting four-probe measurements and voltage measurements transverse to the current direction (Layout 1, see Fig. 4.2a), as well as patterns defining many channels of various lengths in two-probe configurations. Typically a channel is 20 μm wide and between 10 and 500 μm in length (Layout 2, see Fig. 4.2b).

After fabrication the sample was placed inside a glovebox under pure N_2 atmosphere (< 0.1 ppm O_2, H_2O), where it was heated to

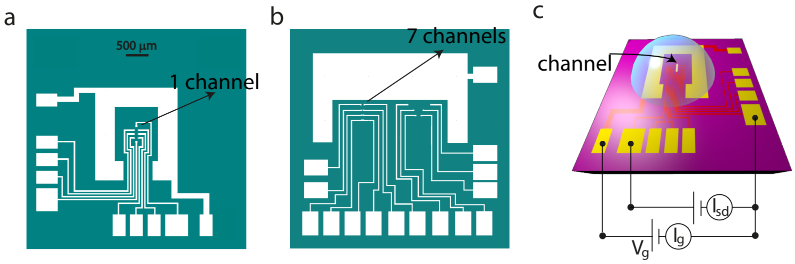

Figure 4.2: **(a)** Schematic representation of the electrodes and channel of Layout 1, consisting of 1 channel of dimensions 60×300 μm^2. **(b)** The same for Layout 2, consisting of 7 channels of the same width (20μm) and varying lengths (5, 10, 20, 50, 100, 200 and 500 μm). (c) A Schematic top view of the sample designed according to Layout 2. Except for the large Au gate electrode around the center of the sample, the Au contacts at the sides of the samples, and the channel area near the center, the whole surface is covered by a hard-baked photoresist layer (purple). For the pattern illustrated here, the contacts at the sides are connected to a Hall bar configuration for measuring the electronic properties of the channel area of $SrTiO_3$. A bias voltage $V_{\rm sd}$ between source and drain electrodes is applied, while simultaneously measuring the source-drain current $I_{\rm sd}$. The gate electrode (G), has an exposed area of more than 100 times the area of the exposed $SrTiO_3$ channel. The potential difference $V_{\rm g}$ is applied between the gate and drain electrodes, while the gate current $I_{\rm g}$ is measured simultaneously.

120 C for 1 hour in order to remove adsorbates from the surface. The ionic liquid used here is N,N-diethyl-N-(2-methoxyethyl)-N-methylammonium bis(trifluoromethylsulphonyl)-imide (DEME-TFSI), which was tored in a closed bottle. Special care was taken in keeping the ionic liquid free from oxygen and water as much as possible. Before use, the bottle was opened in the glove box and the IL was pretreated by heating it to 60 C for a period of 72 hours. A metal needle was then inserted into the bottle in order to pick up a small droplet at the tip of the needle. This droplet was applied on top of the sample such as to cover the Au gate electrode and the channel area, as illustrated schematically in Fig. 4.2c, followed by the transportation of the sample to the sample chamber of the Oxford Instruments Cryofree Teslatron cryogenic measurement system. Before starting the measurements this chamber was thoroughly flushed with high-purity He gas and pumped to 10^{-4} Pa to evacuate contaminations from the atmosphere before cool-down of the sample.

We have used two Keithley 2400 SourceMeters for the experiments, one of which was used for setting up a source-drain bias voltage of $V_{\mathrm{sd}} \leq 250$ mV while simultaneously measuring the source-drain current I_{sd}. We verified that the results are independent of this setting using compliance values as low as 20 mV. The initial, insulating state of $\mathrm{SrTiO_3}$ has a resistance above our measurement limit of 25 GΩ. The other SourceMeter was used for applying the desired gate voltage V_{g}, and for simultaneously monitoring the gate current I_{g}.

We have tested only positive gate voltages, leading to electron doping of the $\mathrm{SrTiO_3}$ surface, in accordance with previous experiments. In order to minimize electrochemical carrier doping of the channel the gate voltages V_{g} were limited to a maximum of 3.2 V [183]. Furthermore, the temperatures at which the gate potential was first applied, which we will refer to as the charging temperatures, were chosen to be close to the glass transition temperature $T_{\mathrm{g}} \approx 182$ K of DEME-TFSI [188].

4.3 Experimental results

We start the experiments by stabilizing the sample at a temperature T above the glass temperature of the IL, after which at $t = 0$ the gate potential V_{g} is switched from zero to a chosen fixed value, and the gate current is recorded simultaneously with the channel conductance. We observe the following: After switching the gate potential a waiting time t_{d} elapses before we observe any measurable response in the conductance of $\mathrm{SrTiO_3}$, as shown in Fig. 4.3 for $T = 195$ K and several settings of V_g. [2] When the gate is switched back to zero the decay of the conductance takes place on a much shorter time scale. We introduce a waiting time of at least 10 minutes before a new gate voltage is set.

The delay time of the main signal strongly increases for lower temperatures (as illustrated for a different sample in Fig. 4.4, Layout 2) and becomes very long (> 1000 s) when the temperature approaches the glass transition temperature of about 182 K of the ionic liquid. After the conductivity onset, the current approaches a nearly exponential increase, as shown by the blue dotted curves in Fig. 4.4a. The current $I_{sd}(t)$, here plotted on a linear scale, is closely described by

---

[2] The small current signal decaying immediately after $t = 0$ is part of the gate current that flows through the source contact. The gate current is discussed in more detail further down in the text.

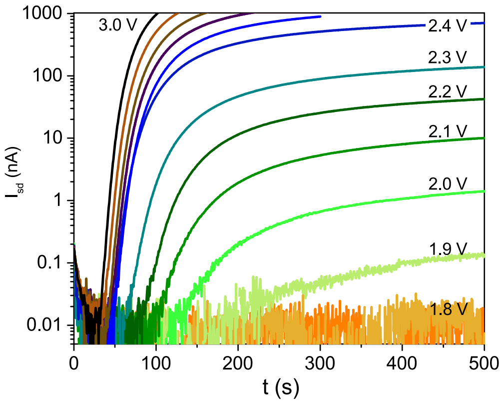

Figure 4.3: Time evolution of the source-drain current for a channel, 10×20 μm^2, Layout 2, at a bias voltage of $V_{\mathrm{sd}} = 250$ mV. After stabilizing the temperature at $T = 195$ K and at $V_{\mathrm{g}} = 0$ the gate voltage V_{g} is switched at $t = 0$ instantaneously to the values indicated by the labels for each of the curves. A time t_{d} elapses before the current suddenly rises above the noise floor of about 10 pA, and the current increases nearly exponentially.

a single exponential function $I_{sd}(t) = I_0(1 - \exp(-(t - t_{\mathrm{d}})/\tau)$, which defines our time constants t_{d} and τ. These time constants are plotted as a function of temperature in Fig. 4.4b, showing that the times rapidly grow for temperatures approaching the glass transition, and that the two times are of similar magnitude.

The gate current, on the other hand, switches instantaneously, followed by a smooth decay, as shown in Fig. 4.5. We have scaled each of the gate currents by the applied gate potentials, ranging from 1.4 V to 3.0 V, and the resulting curves perfectly collapse to a universal time dependence. The lack of voltage dependence in the scaled gate current provides strong support for a purely electrostatic charging process. The curves in Fig. 4.5 are closely described by a combination of two exponentially decreasing functions, with time constants τ_{g1} and τ_{g2}, as illustrated by the red broken curve. The absence of long-time tails in the gate current with $\sqrt{t}$ dependence further testifies for the absence of electrochemical contributions to the charging process [183]. We find that the precautions taken to prevent oxygen and water from interacting with the ionic liquid are critical for this result. For example, when pumping the sample chamber of the cryo-

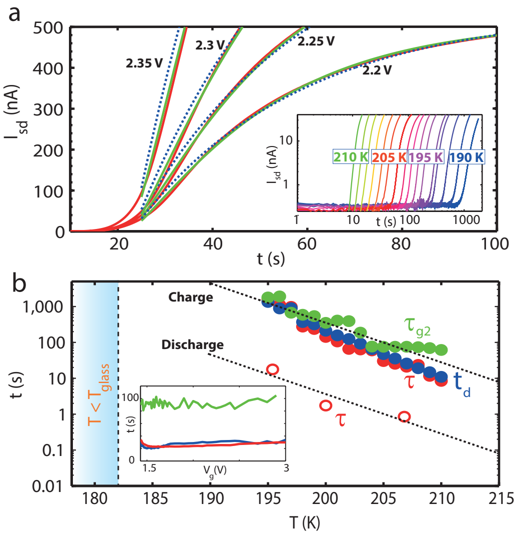

Figure 4.4: Time delay in the response of the conductance of a $SrTiO_3$ channel ($10{\times}20$ μm^2, Layout 2) upon application of a gate potential. (a) Source-drain current as a function of time after switching to a fixed gate voltage as indicated, for a charging temperatures of 205 K. The blue dotted curves show the single-exponential fits (see text). The green curves give the fits based on the percolation model. The inset shows the source-drain current on a log scale for a range of temperatures and for $V_g = 2.5$ V. (b) Time delay t_d (blue) and time constants τ (red) as obtained from the fits to the time-evolution of the source-drain current in (a) for $V_g = 2.5$ V, plotted as a function of the charging temperature. For a few temperatures we also show the discharge time constants, which are much faster. The green points represent the time constant τ_{g2} for the decay of the gate current. The time constants increase nearly exponentially when approaching the glass temperature of the ionic liquid at 182 K, as illustrated by the straight dashed lines. The inset shows that the time constants are nearly independent of the gate voltage, for $T = 205$ K, where we use the same color coding as in the main panel.

genic system to only 1 Pa we observe strong deviations from purely exponential decay of the gate current, the scaling of the gate current with gate voltage breaks down (Fig. 4.5 inset), and the saturation value of the source-drain current becomes only weakly dependent on the gate potential.

The time constant τ_{g2} is also shown in Fig. 4.4b, and has a similar magnitude and temperature dependence as found for t_d and τ. The time constants are nearly independent of the gate potential to within 20%, as shown in the inset.

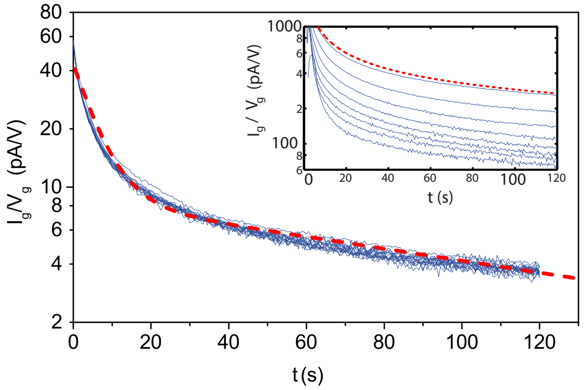

Figure 4.5: Time evolution of the gate current I_g, scaled by the gate potential, upon application of 15 different gate potentials ranging from 1.4 V to 3.0 V at a charging temperature of 205 K. The curves perfectly collapse to a single smooth time evolution, which is closely described by a combination of two exponential functions with time constants τ_{g1} and τ_{g2} (red broken curve). The inset shows the curves between 2.3 V to 3.0 V at a charging temperature of 220 K, typical of experiments performed at a minimum pressure of 1 Pa. In such circumstances, the curves no longer are described by a universal time dependence, and show clear V_g dependence. The individual curves are better described with a Faradeic term. The red, broken curve is a single $t^{-1/2}$ term fit of the data belonging to $V_g = 3.0$ V ($R^2 = 0.9814$).

4.4 Discussion

The fact that all time constants, t_d, τ, and τ_{g2}, have very similar values and that they depend in the same way on temperature suggests that the processes are intimately linked, and are dominated by the ionic conduction in the liquid. The ionic conductivity becomes very small close to the glass transition and limits the charging time of the total capacitance C_{tot}. The ionic conductivity can be described by the Vogel-Fulcher-Tamman (VFT) equation [189],

$$\rho = A\sqrt{T}\exp\frac{B}{T-T_0}. \tag{4.1}$$

Here, A and B are constants related to the ion density and the activation energy for ion transport, respectively, and T_0 is the ideal glass transition temperature. The temperature dependence of the time constants in Fig. 4.4b agrees with this nearly exponential dependence, as indicated by the broken lines in the figure, although the temperature interval explored here is not wide enough for testing the full expression.

The time delay in the source-drain current I_{sd} and the fact that the gate current in Fig. 4.5 does not show a single-exponential decay as expected for the simple charging of a capacitor could be due to the charging properties of the IL. Yuan *et al.* [190] have analyzed the dynamic capacitance of the system of the DEME-TFSI ionic liquid in contact with a ZnO surface as a function of temperature and frequency. They find that the system can be represented by two resistor-capacitor systems in series. One of these represents the charging of the surface capacitance, and the other the geometric response of the ionic liquid. However, the latter produces a response on time scales that are two or three orders of magnitude shorter than those observed for the initial fast decay of the gate current, as can be read from Fig. 5 in Ref. [190] and such processes, if present, would not be resolved on the timescale of our experiments. In our case the two time scales find a natural explanation in terms of the voltage dependence of the surface capacitance of $SrTiO_3$.

Given the fact that $SrTiO_3$ is a wide band gap insulator the delay time in the source-drain current I_{sd} can be attributed to the role of the threshold potential V_{th} required for bringing the electrochemical potential at the surface of $SrTiO_3$ to the edge of the conduction band. After switching on the gate voltage the potential at the $SrTiO_3$ surface is expected to rise exponentially in time. At equilibrium the potential in the ionic liquid near the surface of $SrTiO_3$ is given by the division of the potential over the series connection of the capacitance at the gate and the capacitance to the outside world. Since the former is orders of magnitude larger, the potential at the surface reaches nearly the full gate potential. In the process of building up this surface potential as a function of time the conduction band of $SrTiO_3$ is locally pulled down until, at a threshold potential V_{th} the chemical potential of the electrons in the Au leads is aligned with the bottom of the conduction band. This condition is met after a time delay t_{d}, and from this moment on a two-dimensional electron system (2DES) can develop at the surface of $SrTiO_3$. As the ionic surface charging continues towards saturation the density of carriers in the 2DES grows and the conductivity increases. This interpretation of the delay time is consistent with the fact that we observe no substantial conductivity for gate voltages smaller than 1.8 V.

The integrated gate current after saturation gives the total charge Q and we find that this scales linearly with the gate potential, in agreement with the scaling in Fig. 4.5. The proportionality constant between Q and V_g gives the total capacitance, $C_{\text{tot}} = Q/V_{\text{g}}$, for which we obtain 1.4 nF, for the sample configuration of the data in Figs. 4.4 and 4.5. This capacitance is larger than expected for a capacitance associated with an individual channel. For the channel with size $20 \times 10\mu\text{m}^2$ used for the measurements presented above, and a specific capacitance at high gate voltage at the SrTiO_3 surface of 13 $\mu\text{F/cm}^2$ [185], the expected capacitance is 26 pF. The larger value of the capacitance obtained from the gate current reflects the fact that the capacitance associated with the gate current is the total capacitance of the ionic liquid droplet to the outside world and includes the capacitive coupling to the other channels on the sample. Estimates based on the total exposed area of SrTiO_3 gives 2.3 nF, which agrees within a factor of two with observation.

The fact that the capacitance is dominated by the interface with SrTiO_3 implies that the capacitance must be voltage dependent. The delay time observed in the source-drain current implies that this capacitance switches to a larger value as soon as the potential at the surface brings the Fermi energy up to the conduction band edge. We take this effect into account by a simplified model through a combination of two time constants, $I_g(t) = I_1 \exp(-t/\tau_{\text{g}1}) + I_2 \exp(-t/\tau_{\text{g}2})$, and the fit to this expression is shown by the broken curve in Fig. 4.5. The second time constant is the one associated with the charging of the surface capacitance in the regime of a finite conducting surface charge density. The cross over between the two regimes occurs at a time that is similar to the delay time observed in the source-drain current. The initial time constant $\tau_{\text{g}1}$ is attributed to the residual capacitance, dominated by the Au contacts to the channels.

The discharge curve for the source-drain current, recorded when switching the gate potential back to zero, is again closely described by a single exponential. This represents the relaxation of the EDL and we observe that this process is much faster than the build-up of the double layer, as shown in Fig. 4.4b. As was discussed in Ref. [187] the difference in charging and discharging times can be understood as the competition between two driving forces. When charging the EDL the cations are driven towards the interface by the electric field, but the concentration gradient drives them in the opposite direction. When discharging, the electric field of the charge layer works in the same direction as the concentration gradient, resulting in a larger combined driving force for the current. From these observations we conclude that the ionic conductivity obtained from the process of charging and discharging of the EDL may deviate from the bulk conductivity.

Nevertheless, we can use the experimental values for τ for estimating the ionic resistivity ρ taking into account the geometry and size of the electrodes according to Layout 2. We take the channels as approximately one-dimensional, and combine the contribution to the charging current from all channels on the sample. The resistivity can then be approximated by $\rho = \pi RL/\ln(W/a)$, where $R = \tau/C$ is the resistance obtained from the time constant and the capacitance, $L = 910\,\mu$m is the total length of the channels, $a = 10\,\mu$m is half the width of the channels, and $W \simeq 1$ mm is the radius of the ionic liquid droplet. The values for ρ thus obtained are accurate to within a factor of two as limited by our knowledge of the geometry of the droplet (represented by the errorbars), and are plotted in Fig. 4.6 along with the known literature values [188, 191]. The curve fit is based on the VFT equation (4.1) [189]. The fit parameter T_0 is the ideal glass transition temperature, which is typically 30 to 50 K lower than the T_g measured by means of differential scanning calorimetry [189], as is the case for DEME-TFSI [188]. In our case the VFT function gives a good fit, with $T_0 = 151\pm7$ K, demonstrating that our interpretation of the delay time produces values for the ionic liquid conductivity that are in good agreement with the available literature data. Note that our data points appear to be slightly above an extrapolation of the literature values, which may result from the fact that our resistivity data are obtained from the properties of the EDL and thus be influenced by the concentration gradient.

In order to connect the charging/discharging dynamics in the ionic liquid with its effect on the electrical conductivity of the channel we now turn to the properties of the 2DES, notably its conductivity extrapolated to long times, σ_∞. Despite the metallic characteristic at high charging voltages [177], the 2DES cannot be viewed as a normal metal because we find that the conductivity strongly depends on the length of the channels, decreasing for channel lengths running from 10 to 500 μm. As another indication of this anomalous character the conductivity of the 2DES remains well below the conductance quantum, $\sigma_\infty \ll e^2/h$. These observations are consistent with an interpreta-

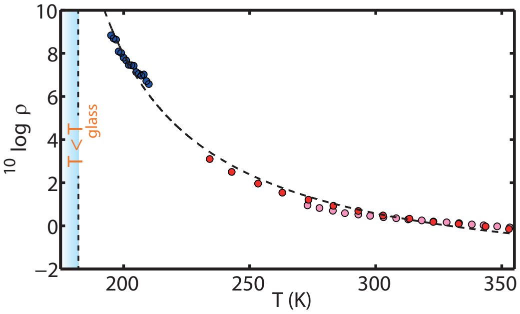

Figure 4.6: Plot of the ionic liquid resistivity as a function of temperature. The blue points are obtained in this work as calculated from the observed delay times. Red and pink points represent literature values for ρ, as taken from Refs. 188 and 191. The fit curve is based on the Vogel-Fulcher-Tamman equation. The fit parameters are: $T_0 = 151 \pm 7$ K, $A = 4.8 \times 10^{-3}$ Sm^{-1}K$^{-0.5}$ and $B = 1.3 \times 10^3$ K ($R^2 = 0.994$).

tion of the conductivity in terms of Anderson localization and the formation of percolation networks of conducting paths [178].

This observation appears to be contradicting the nearly perfect exponential growth of conductance with time seen in Fig. 4.4. In a 2DES percolation model the conductance is expected to be controlled by the charge density n according to [192],

$$\sigma = A\,(n - n_{\mathrm{c}})^{4/3}\,, \tag{4.2}$$

where A is a system specific constant and n_{c} is the two-dimensional critical density for forming a percolation path. Assuming a sharp conduction band edge, the charge density at the surface is controlled by the local electrostatic potential V created by the ionic liquid at the surface of the $SrTiO_3$ crystal, as

$$n(V) = c\,(V - V_{\mathrm{th}})\,, \tag{4.3}$$

where V_{th} is the threshold voltage determined by the position of the conduction band edge, and c is the capacitance per unit area. From the discussion above we conclude that after the delay time the local potential V follows a simple exponential law for the charging of a capacitor $V(t) = V_{\mathrm{g}}(1 - \exp(-t/\tau))$. Combining this with Eqs. (4.2),(4.3) we expect a time evolution for the conductivity,

$$\sigma(t) = \sigma_\infty\,(\alpha - \exp(-t/\tau))^{4/3}\,. \tag{4.4}$$

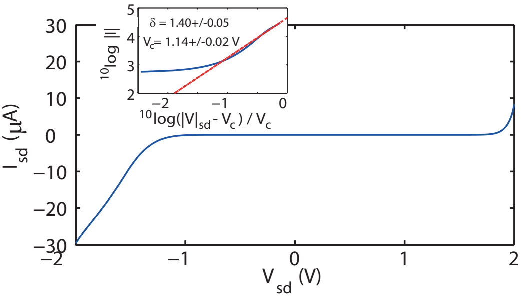

Figure 4.7: $I(V)$ of the channel for $V_{\mathrm{g}} = 2.5$ V taken at $T = 20$K. The curve is non-linear and can be described by the RRTN percolative model, where $I_{\mathrm{sd}} \propto (V_{\mathrm{sd}} - V_{\mathrm{c}})^{\delta}$. The inset shows the corresponding log-log plot of the negative V_{sd} part of the data. The red, broken line shows the fit to the data with $V_c = 1.2$ V, and $\delta = 1.30 \pm 0.02$.

Here, $\sigma_{\infty} = A(cV_{\mathrm{g}})^{4/3}$, and $\alpha = 1 - V_{\mathrm{th}}/V_{\mathrm{g}} - n_{\mathrm{c}}/(cV_{\mathrm{g}})$ is a constant of order unity. This functional form fits the observed time dependence very well, as demonstrated by the green solid curves in Fig. 4.4.

The close match between the fit and the observed time dependence of the conductance supports the interpretation that the conductance is just controlled by the local electrostatic potential of the ionic liquids at the surface.

For 2D percolative systems, e.g. random-resistor-tunneling-networks [193], certain I(V) characteristics are expected. When a voltage is applied between the source and drain electrodes, no current flows below a critical voltage V_c. For $V > V_c$ a certain scaling behavior is to be expected, according to $I_{sd} \propto (V - V_c)^{\delta}$ [194], for which the value δ corresponds to the same 4/3 [193], also found in $\mathrm{SrTiO_3}$ [195]. We find similar, non-linear behavior at low temperatures for gated channels (Fig. 4.7). The channel gated at $V_{\mathrm{g}} = 2.5$ V shows scaling behavior with $\delta = 1.30 \pm 0.02$ and $V_{\mathrm{c}} = 1.2$ V at $T = 20$K.

Any electrochemical influence of the surface charge density would involve diffusion of the reaction species towards and away from the surface and is expected to show up as a time dependence $t^{-1/2}$ [183, 196]. This would be seen as a lack of saturation at long times, which we encounter in our experiments when we relax the conditions for treatment of the ionic liquid, so that oxygen (or water) contamination starts playing a role. For example, when evacuating the sample space at the start of the experiments to only 1 Pa we observe a break down of the scaling in Fig. 4.5 and the 2DES conductivity does not saturate. Remarkably, poorer vacuum conditions often lead to higher maximum 2DES conductivities, but for longer gating times the conductivity starts degrading and becomes dependent on the gating history.

Apart from the methods employed in this work to illustrate the difference between electrostatics and electrochemistry, other methods can also be employed to further illustrate this contrast through enhancement of electrostatic gating. An example of this is the usage of monolayer separator layers such as hexagonal boron nitride [179] or other insulating materials to prevent direct contact between the ionic liquid and the surface of $SrTiO_3$. Although such although the increased double layer distance limits the polarization and changes the Coulomb scattering and mobility properties of the 2DES, measurements of the onset of conduction with such a separator layer in place could provide a further means of minimizing any possible contribution of electrochemistry to the gating process here.

In the analysis of the time dependence we have ignored delays in charging times due to the finite conductivity of the 2DES. In analyzing time delays similar to those reported here for experiments on $SrTiO_3$ with a solid electrolyte Tsuchiya *et al.* [185] proposed a model of charge build up that evolves gradually over the surface of the solid, initiated from the contact electrodes. Initially the $SrTiO_3$ surface is assumed to be a perfect insulator. Near the electrodes the build up of an electrostatic potential in the ionic liquid pushes the chemical potential to the conduction band edge, allowing local charging of the $SrTiO_3$ surface. This charged surface then serves as the contact electrode for the next section of the surface.

If this model were correct the time delay would depend linearly on the channel length. We have tested this in two ways. First, for fixed channel length in Hall bar configuration we measured the conductivity across the channel at two points, using small capacitors to connect to the side contacts and an ac lock-in resistance measurement technique. The coupling by small capacitors prevents the side contacts from forming nucleation points for the formation of a 2DES. When switching the dc source-drain bias we find that the conductance along the channel and at two points across the channel develop nearly simultaneously. The noise on the ac signal limits our accuracy in determining the delay times, but they are equal to within 20%. In addition, we tested on another sample a series of channels in 2-point configuration with lengths of 10, 20, 50, 100, 200 and 500 μm. The observed time delays show a variation by about 50%, but no systematic systematic dependence. In fact, the shortest channel showed the longest delay time. We conclude that the charging of the surface occurs nearly homogeneously, and we tentatively attribute the small variation in delay times to variation in the geometries and positions on the sample.

The absence of a length dependence in the delay times suggests that the conductivity of the 2DES is not a limiting factor in the formation of the EDL. We picture the charging process as follows. When a gate potential is applied a standard EDL forms at the surfaces of the gate and at the Au contact electrodes. Since the area of the gate is much larger, the voltage drop concentrates at the surface of the small source and drain contacts. Towards equilibrium the potential would assume a homogeneous level inside the ionic liquid, and this would approach the potential of the gate. Since the surface of the $SrTiO_3$ crystal is in contact with this ionic liquid it feels the rising of the potential of the ionic liquid towards that of the gate over its entire surface. Only when this potential brings the conduction band edge to the level of the Fermi energy the EDL starts to form, and electrons flow in from the electrodes. At that moment the conductance is already well above the conductance of bulk $SrTiO_3$ in equilibrium. When the resistance of the 2DES drops below our detection limit of about 25 GΩ, the estimated RC time for a channel of $10 \times 20\,\mu$m, using the quoted specific capacitance of 13 μF/cm^2, is only 0.6 s, much smaller than the observed time delays. We conclude that the observed time dependence is entirely dominated by the ionic conductivity of the IL.

In conclusion, we have demonstrated that IL-gating on insulators, *i.c.* $SrTiO_3$, at charging temperatures close to the glass temperature T_{g} produces a delayed transition to a conducting surface state. The delay time is strongly dependent on the temperature and diverges near T_{g}. The time delay and time evolution of the conductance can be described by a process of homogeneous charging of the surface, and is determined by the band gap of the insulator. The conductance that results is consistent with a percolation model of transport. We provide a method of distinguishing between electrochemical and electrostatic processes by using the scaling behavior of the gate current, which is of crucial importance in this rapidly developing field of research. We find no evidence of charge doping by electrochemical reactions when charging close to the glass temperature of the IL, provided we maintain strict conditions during handling of the ionic liquid.

Chapter 5

On the nature of ionic liquid gating of $Nd_{2\text{-}x}Ce_xCuO_4$ thin films

Recently, ionic liquid gating has been used to modulate the charge carrier properties of metal oxides. In this chapter, we report experiments on doped and undoped Nd_2CuO_4*. We find major resistance drops of the bilayer coupled to observations of the presence of a considerable Faradeic component in the gate current and of the appearance of charge transfer peaks in the cyclic voltammetry data. In contrast the work on* $SrTiO_3$ *described in the previous chapter, trace amounts of contaminations present in the ionic liquid cannot be excluded, and we propose a mechanism of gating based on irreversible electrochemical reactions. This work is in line with previous reports confirming the presence of irreversible electrochemistry in ionic liquid gated electron-doped cuprates.*[1]

---

[1] The work in this chapter was published as: On the nature of ionic liquid gating of $Nd_{2\text{-}x}Ce_xCuO_4$ thin films, Hasan Atesci, Francesco Coneri, Maarten Leeuwenhoek, Hans Hilgenkamp and Jan M. van Ruitenbeek, *Low Temperature Physics* **43**, 290, 2017.

5.1 Introduction

Since its discovery in 1986 [197], high temperature superconductivity (HTS) in doped Mott-insulator cuprates has generated much interest [198]. Although the mechanism of pairing remains illusive [199–202], many of its characteristics have been firmly established. Cuprate HTS can be either hole-doped or electron-doped, and typically shows a dome-shaped phase diagram as a function of chemical doping [203]. However, chemical doping induces disorder in the Mott-insulator compound[8], which can be avoided by electrostatically doping the HTS using an oxide gate dielectric [204–207]. Oxide gate dielectrics have successfully achieved changes in the critical temperature of cuprates [208]. But, due to the break down electric field [209, 210], the induced charge carrier density is limited to $\sim 10^{13}$ cm^{-2}, having only a relatively small influence on the changes on the conductive properties of the cuprate [211]. This is due to the fact that the charge carrier density in Mott insulator cuprates requires an areal density of up to 10^{14} cm^{-2} in order to go through the phase diagram of HTS cuprates. To overcome this problem, ionic liquids (ILs) have recently been used as gate media to generate high carrier accumulation [109, 212]. ILs consist entirely of ions, and when a voltage is applied across the IL, Helmholtz electric double layers are formed. These layers consist of ions of one kind of the IL and the induced charge carriers of the solid and are separated ~1 nm from each other. With IL gating, carrier densities of up to 8×10^{14} cm^{-2} are achievable [109], substantially higher than what is attainable with their conventional dielectric counterparts, making it possible to induce insulator-to-superconductor transitions [59, 60, 213].

In this work, we attempt to address two points of interest. Firstly, most of the IL experiments on cuprates have been done on hole-doped cuprates [10, 59, 61], whereas for electron-doped compounds only $Pr_{2\text{-}x}Ce_xCuO_4$ and $NdBa_2Cu_3O_{7\text{-}\delta}$ have been tested with ILs [65, 66, 214]. Hence, IL gating on electron-doped cuprate compounds is important for obtaining a more complete picture of its effects on cuprates and high-temperature superconductors in general. Secondly, there is an increasing number of articles stating that the effect of IL gating in cuprates and other oxides is related to electrochemistry [11, 49, 67–69, 214], indicating that the ideal picture of EDL electrostatics suggested in some articles [10, 59, 60, 213] might not be valid.

5.2 Experimental details

We have applied the IL gating technique at the pulsed laser deposition (PLD) grown electron-doped cuprate of single layers of undoped Nd_2CuO_4 (NCO) and bilayers of 0.10 Ce doped $Nd_{2\text{-}x}Ce_xCuO_4$ ($x = 0.10$) (NCCO) and NCO (NCCO/NCO). We have used a deposition temperature of 820 C and O_2 pressure of 2.5×10^{-1} mbar. The NCO and NCCO targets are ablated using a laser fluence of ~ 1.2 J/cm^2 and repetition rate of 4 Hz. The cuprate is grown on substrates formed by a pristine $(LaAlO_3)_{0.3}(Sr_2TaAlO_6)_{0.7}$ (001) (LSAT) crystal. The cuprate and substrate have lattice parameters of 3.94 Å and 3.87 Å, leading to some epitaxial strain in NC(C)O. For the reason of lowering the epitaxial strain of the upper layers, we have grown the bilayers [10, 153, 215, 216].

By varying the lens and mask positions and the energy of the laser beam, we can influence the spot size of the laser beam, while keeping the laser fluence constant at 1.2 mJ/cm^2. We observe that a lower spot size and a lower energy leads to a lower growth rate of the compound per pulse, and is in general more suitable for layer-by-layer growth. For our system, we find a growth rate of 0.5 Å per pulse using optimized settings (spot size of 2.2 mm^2 and an energy of 29.3 mJ) for layer-by-layer growth. To monitor the in-situ growth of the cuprate, we have used Reflection High Energy Electron Diffraction (RHEED) Fig. 5.1a. The intensity of the specular reflected beam shows clear oscillations for the first unit cells of the compound. The amplitude of these oscillations quickly dies out, indicating a transition from layer-by-layer growth to island-like growth fashion. For the thicknesses of the films we are interested in, the resulting morphology of the films is characterized by screw dislocations, showing the spiral growth mode of the cuprate grains Fig. 5.1b, and is similar to what is found for cuprates grown on substrates having lattice mismatches [160, 161].

We have tested a total of 22 samples, where the NCO single layers have thicknesses varying from 12 to 48 unit cells, while NCCO/NCO bilayers have bottom layers that are 24 to 46 unit cells thick and top layers that are 4 to 12 unit cells thick. We show that IL gating has an effect in lowering the resistance of a bilayer of the compound, and we argue that this is caused by electrochemical reactions, likely because of trace amounts of impurities present in the IL. The results shown in this paper are for a particular NCCO/NCO bilayer of 20 unit cells thick NCO and 5 unit cells thick NCCO, and is reproducible for the

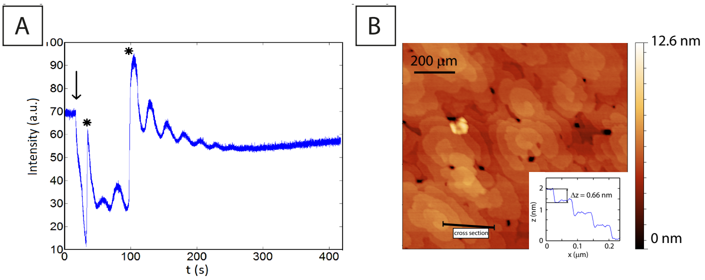

Figure 5.1: **(a)** RHEED intensity vs. time graph which shows the oscillations of the specular reflected beam for the first few unit cells of the cuprate, after which the amplitude of the oscillation goes to zero, indicating an island-like growth fashion. The arrow indicates the start of the PLD process, while the asterisks show the instances where the electron beam intensity has been increased manually. **(b)** The AFM data shows the screw-island growth mode of a typical cuprate film on LSAT. The step heights coincide with half a unit cell of NC(C)O (1.2 nm).

other samples, unless stated otherwise.

After the PLD process, we use photolithography to define areas on the sample that will be maintained, while the rest is removed by argon ion milling. In order to decrease the contact resistance, all of the remaining bilayer is covered by sputter deposition of Ti/Au, apart from the bilayer of the channel area. It is to be noted that Ti/Au deposition on NC(C)O does not lead to a non-Ohmic contact, which is not true in the case of $La_{2\text{-}x}Sr_xCuO_4$, as has been pointed out in Chapter3. In order to prevent unnecessary leakage currents, the substrate surface is then covered by an insulating photoresist layer, except for the gate electrode and channel (Fig. 5.2a). The exposed areas are chemically etched in an oxygen plasma (100 mTorr, 13 W) which removes any residuals of the photolithographic process.

The sample is then placed inside a N_2 atmosphere glovebox (<0.1 ppm O_2 , H_2O),where it is heated to 120 C to remove any water on top of the surface. The ionic liquid bottle containing N,N-diethyl-N-(2-methoxyethyl)-N-methylammoniumbis(trifluoromethyl- sulphonyl)-imide (DEME-TFSI), is kept in the same atmosphere. Before any usage of the IL, it is preheated at 60 C for a period of more than 72 hours. With the insertion of a needle in the IL bottle, a small droplet is formed at the end of the needle, which is then put on top of the gate electrode and the bilayer channel area (Fig. 5.2b). Next, the sample

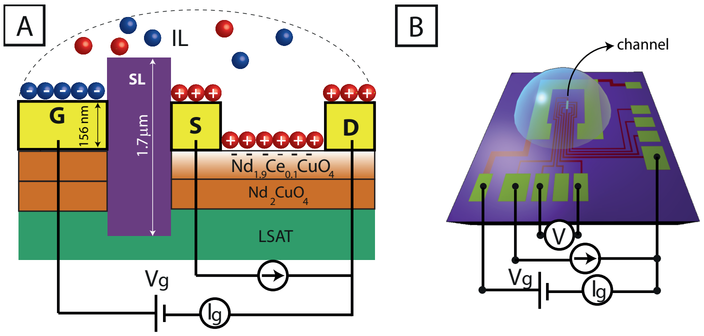

Figure 5.2: **(a)** A schematic cross section of the sample. Here, yellow and blue spheres represent TFSI(-) and DEME(+) ions, respectively. The gate (G), source (S) and drain (D) electrodes are 6 nm (Ti) + 150 (Au) nm thick and are made using photolithograpy after deposition of the bilayer. A separator layer (SL) ensures only the bilayer channel at the surface of the NCCO between the source and drain electrodes in contact with the ionic liquid droplet. Applying a voltage between the gate and drain electrodes leads to a charge buildup in the channel. **(b)** A schematic top view of the sample. Except for the large Au gate electrode around the center of the sample, the Au contacts at the sides of the samples, and the channel area near the center, the whole surface is covered by a hard-baked photoresist layer. The contacts at the sides are connected to a Hall bar configuration of electrodes on the channel to measure electronic properties of the channel area of the bilayer, which is freed from photolithographic residuals by oxygen plasma etching. A current is sent through the source (S) and drain (D) electrodes. In combination with voltage probes placed at one side of the sample, the four-point resistance of the channel is measured, having an area of 50 x 300 μm^2. The gate electrode, has an exposed area of more than 100 times the area of the exposed NCCO channel.

is transported to the insert chamber of the measurement setup, which is flushed with He gas and pumped several times to a pressure of 1 Pa to remove contaminations (O_2 and H_2O) from the atmosphere of the sample.

We use two Keithley 2400 SourceMeters for the experiments. One SourceMeter is used to measure the four terminal resistance of the channel. To this end, we apply a current bias between the source and drain electrodes (500 nA), while limiting the maximum voltage V_{sd} to 250 mV. We use the other SourceMeter for the application of a gate voltage V_g and monitoring the gate current I_g. In order to limit electrochemical processes influencing carrier doping of the channel, the maximum V_g applied is 2.5 V, which lies well within the potential window of the liquid [122, 217]. Furthermore, the experiments are performed at a suitable charging temperature of 210 K [218], above the melting point of DEME-TFSI of 184 K [219].

Our measurement comprises five cycles of two sub measurements. The first sub measurement is in-situ cyclic voltammetry (CV) in order to test for possible chemical reactions in the Au/IL/bilayer system [220]. During the CV, I_g is measured while modulating V_g from 0 V to 2.5 V and back to 0 V again at a scan rate of 5 mV/s. The second sub measurement records the $I_g(t)$ and four terminal resistance $R(t)$ characteristics of the channel after switching the gate voltage from zero to +0.5 V, +1.0 V, +1.5 V, +2.0 V and +2.5 V for 15 minutes. After the second sub measurement is finished, the Keithley instruments are reset to zero for approximately 30 minutes. The relaxation time of the charges in the IL can be estimated by $R_{IL}C_{EDL}$, where R_{IL} is the resistance of the IL, approximated to be in the order of 10^9 Ω [98]. The electric double layer capacitance is estimated as 2 nF, since the channel area is 1.5 $\times 10^{-4}$ cm^2 and the specific capacitance is 13 μFcm^{-2}. Thus, the RC time is in the order of seconds, making the waiting time of 30 minutes sufficiently long to cancel any memory effect of the ions.

5.3 Experimental results and discussion

The CV data in Fig. 5.3 indicates the presence of irreversible reactions. This is based on the fact the the first cyclic voltammogram does not show any peaks, indicating that the IL is clean and that no electrochemical reactions take place in the initial stages of the experiment.

The subsequent CVs do show peaks, denoted as peaks I (cathodic), II and III (both anodic). Peak I is located between 1.35 and 1.95 V and indicates an initial reduction. Peak II and III are located between 1.1 and 1.44 V, and 0.29 and 0.55 V, respectively. If peak I would be caused by a reversible reaction, only one anodic peak would be expected. However, we see two anodic peaks, indicating the oxidation of either the product(s) or a part of the product(s) of this reduction. Furthermore, if peaks I and II are part of the same reversible reaction, the Nernst equation would dictate that for reversible electrochemistry the difference in potential of the anodic and cathodic peaks lies within 0.059 V [221]. Moreover, one would expect that both peaks are equal in amplitude. The CV data shows however, that the potential separation of both peaks (I and II) is $0.27 < \Delta V < 0.51$ V, while the magnitude of peak I is approximately 3 to 10 times larger than peak II for all CV scans.

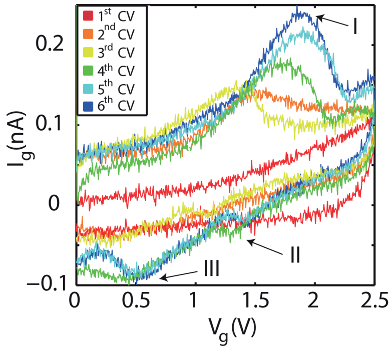

Figure 5.3: Plots showing 6 CV scans. The first cyclic voltammogram does not show any peaks and indicates a chemically pure IL, while the others show peaks increasing in amplitude as a function of the cycle number. As the number of CV scans increases, several peaks (I, II and III) start to appear. Peak I is located between 1.35 and 1.95 V and indicates an initial reduction. Peak II and III are located between 1.1 and 1.44 V, and 0.29 and 0.55 V, respectively. We observe that the potential separation between peaks I and II is $0.27 < \Delta V < 0.51$ V. Furthermore, the amplitude of peak I is a factor 3 to 10 higher than that of peaks II and III.

The presence of irreversible electrochemistry is further supported by AFM data. Fig. 5.4a shows an image of the surface of a freshly prepared sample, with structure typical for island growth of the films. The importance of this observation is that the edges of the islands ex-

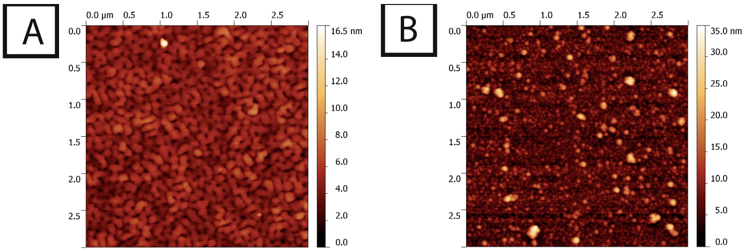

Figure 5.4: AFM images of the surface of the bilayer before and after IL gating experiments. **(a)** Before the experiments, the AFM image shows that NCCO has a topography which is island-based. The roughness of the sample is 0.87 nm. **(b)** After the experiments, the surface lost the former characteristics, and has a higher roughness of 2.35 nm.

pose sites with higher reactivity, which could act as possible seeding locations for electrochemical reactions. Before the experiment, the sample surface topography showed a root mean squared (rms) roughness value of 0.87 nm (Fig. 5.4a). After the IL gating experiments, the surface is altered dramatically, having a substantially higher rms roughness value of 2.35 nm (Fig. 5.4b).

Another argument for electrochemistry is based on our gate current vs. time data. After switching the gate voltage to the set value at the start of the second sub measurement, the gate current data shows a rapid initial decrease, followed by a slowly decaying function, a typical graph of which is shown in Fig. 5.5. In case the charging process is strictly electrostatic, the total accumulated charge would be given by $Q = ACV_g$. Here, A is the total NCCO area and C is the specific capacitance, being equal to 1.5 $\times 10^{-4}$ cm^2 and 13 μFcm^{-2} [222], respectively, making the expected charge roughly 5 nC for the highest gate voltages used. The observed charge, calculated as the integral of I_g, however, is typically one to two orders of magnitude higher for all measurements, suggesting other mechanisms, notably electrochemical reactions, play a role.

We find that the $I_g(t)$ characteristic cannot be fitted with only an exponential term, indicative of electrostatic charging of the bilayer. Rather, we need to add a Faradeic, diffusive, term with a certain proportionality constant K, i.e. $I(t) = K/\sqrt{t}$ to fit the whole curve,

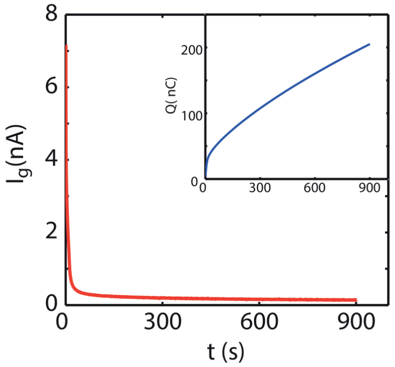

Figure 5.5: $I_g(t)$ curve for a V_g of 2.5 V at 210 K. The inset shows the total accumulated charge Q vs. time, calculated by integrating $I_g(t)$. The total accumulated charge Q exceeds the value that one would expect for a purely electrostatic charge of the NCCO layer, i.e. roughly 5 nC.

with

$$K = \frac{cAF\sqrt{D}}{\sqrt{\pi}}. \tag{5.1}$$

Here, c is the concentration of the substance taking part in the electrochemical reaction A is the area of the bilayer surface, F is the Faraday constant, and D is the diffusion coefficient of the reactive species. We find that the proportionality constant for all of the curves is between $0.04 < K < 1.4$ nA $\mathrm{s}^{\frac{1}{2}}$. The large spread in this parameter is due to the fact that it is gate voltage dependent, where a larger applied gate voltage would lead to higher gate currents and therefore higher proportionality constants. If we assume the cations and anions of the IL are taking part in the reaction, we come to the conclusion that the desired diffusion constant of the species should be $10^{-\beta}$ cm^2/s, with β = 14-18. In this calculation, we take an approximate value for the density of the IL to be 1.5 g/cm^{-3}. The obtained value of D, however, is many orders of magnitude below the expected literature values for DEME-TFSI, which is $10^{-\beta}$ cm^2/s, with β = 8.6 - 10.6 [223, 224]. Because of this difference in diffusion coefficient values, it is not plausible that the anions and cations of the IL take part in the irreversible reaction. A more likely scenario is that trace amount of impurities like hydrogen and oxygen present in the IL react with the surface. Indeed, it has been shown that impurities of hydrogen can lead to major gating effects in oxides [69, 97, 225], while oxygen impurities can lead to either the doping of oxygen [106], or the generation of oxygen vacancies [49, 67, 70]. Although it has been shown that both hydrogenation [226] and (de)oxygenation [227] are applicable to NCCO, it is not possible to deduce which of these processes are present in the present system with our current techniques.

In Fig. 5.6a we show that the resistance R decreases an amount ΔR when a positive gate voltage is applied. Here, ΔR is the difference between R at $t = 0$ s (R_0) and the value of the tangent line at $t = 0$ s of R at $t = 900$ s. In the next figure, the relative change of R is plotted as a function of cycle number and V_g (Fig. 5.6b). The conductance gains in the first cycle are limited and the relative change in R is 5 % at the highest V_g of +2.5 V. However, as the cycle number is increased, the relative change in R shows a systematic increase as a function of both V_g and the cycle number, having a relative change close to 25 % at +2.5 V. This clearly shows the irreversibility of the gating effect, while reversibility is expected in case the gating would be electrostatic. This behavior is typical for single-layered channels of NCO as well. We also observe that the relative change of R is larger for samples that have been tested with a lower degree of purification of IL, again indicating that impurities play a major role in the effect. In Fig. 5.6c we plot the normalized resistance vs. temperature of the gated bilayer. In this figure, we observe semiconducting behavior down to 10 K. For gate voltages up to +2.0 V we observe a systematic decrease of the resistance, but no onset of superconductivity. The application of a higher gate voltage ($V_g \cong 2.5$ V) leads to sample degradation.

5.4 Conclusions

In summary, we have applied IL gating on the single layers of NCO and bilayers NCCO/NCO. We observe that repeated gating leads to the appearance of peaks in the cyclic voltammogram. These reactions have a substantial influence in the resistance of the NCCO layer, especially after a prolonged period of gating, which goes hand in hand with pronounced distortions of the NCCO surface. Together with these observations, we see that accumulated charge in the system that far exceeds the expected electrostatic accumulation. All of these point to the presence of irreversible electrochemical reactions. The fitting

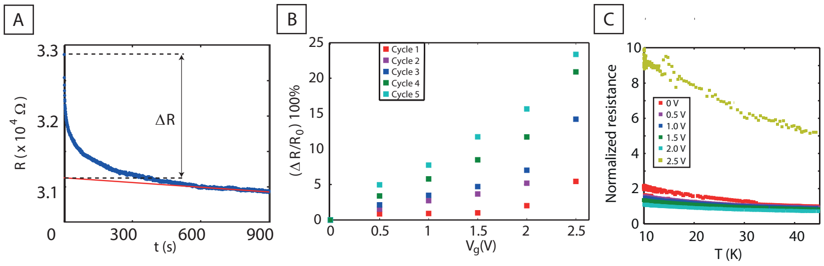

Figure 5.6: **(A)** $R(t)$ curve recorded when at $t = 0$ s a V_g of 0.5 V is applied. The curve shows a change ΔR, defined as the difference between R at $t = 0$ s (R_0) and the value of the tangent line at $t = 0$ s of R at $t = 900$ s. **(B)** The observed relative change in R as a function of gate voltage and cycle number at 210 K. The change in R is systematic and becomes larger as V_g and the number of cycles increases. **(C)** Normalized resistance of the NCCO/NCO channel plotted as a function of T for $V_g = 0$ V, +0.5 V, +1.0 V, +1.5 V, +2.0 V and +2.5 V. The behavior is semiconductor-like, and shows a systematic decrease of the resistance up to a gate voltage of +2.0 V. However, applying a gate voltage of +2.5 V leads to sample degradation.

of the gate current data indicates that these are caused by traces of impurities in the ionic liquid. With the present technique of PLD growth of the material and the choice of substrate, we have found that it is not possible to obtain layer-by-layer growth, which would help prevent electrochemical reactions happening in the compound. This work confirms previous work done on electron-doped cuprates of $\mathrm{NdBa_2Cu_3O_{7\text{-}x}}$ and $\mathrm{Pr_{2\text{-}x}Ce_xCuO_4}$. In the former material, IL gating has been found to produce oxygen vacancies. In $\mathrm{Pr_{2\text{-}x}Ce_xCuO_4}$, gate voltages above + 2.5 V lead to irreversible electrochemical reactions [65]. Similarly, using gate voltages below + 2.5 V leads to a relatively little gating effect, not enough to induce a superconducting transition [66].

Chapter 6

On the nature of ionic liquid gating of $La_{2\text{-}x}Sr_xCuO_4$

Ionic liquids have recently been used as means of modulating the charge carrier properties of cuprates. The mechanism behind it, however, is still a matter of debate. In this paper we report experiments on ionic liquid gated ultrathin $La_{2\text{-}x}Sr_xCuO_4$ *films. Our results show that the electrostatic part of gating has limited influence in the conductance of the cuprate in the gate voltage range of* 0 *V to* -2 *V. A non-electrostatic mechanism takes over for gate voltages below* -2 *V. This mechanism most likely changes the oxygen concentration of the film. The results presented are in line with previous X-ray based studies on ionic liquid gating induced oxygenation of the cuprate materials* $YBa_2Cu_3O_{7\text{-}x}$ *and* $La_{2\text{-}x}Sr_xCuO_4$*.* [1]

6.1 Introduction

Changing the charge carrier density by means of gating is the crux of today's technology, where fields of up to 10 MV/cm are used in transistors to change semiconductor properties. Recently, ionic liquids (ILs) have been used in oxide semiconductors for the application of fields of up to two orders of magnitude higher than that for their conventional solid-state counterparts. ILs consist entirely of ions and form Helmholtz electric double layers at the interfaces with the electrodes

---

[1] The work in this chapter was published as: On the Nature of Ionic Liquid Gating of $La_{2\text{-}x}Sr_xCuO_4$, Hasan Atesci, Wouter Gelling, Francesco Coneri, Hans Hilgenkamp and Jan M. van Ruitenbeek, *Int. J. Mol. Sci.* **19**, 566, 2018.

when a voltage is applied across the IL. One layer consist of anions or cations of the IL, while the other layer comprises the induced charge carriers of the solid. With a ~ 1 nm separation within the double layer charge carrier densities of up to 8×10^{14} cm^{-2} are achievable [109], making it possible to induce insulator-to-superconductor [8, 59, 213] and metal-to-insulator transitions [11, 67, 228].

This technique is driven by an electrostatic mechanism, and holds for many materials [71, 229]. However, when applied to correlated oxide systems [67, 70] there is substantial evidence that electrochemical processes related to interstitial oxygen is crucial in the gating process [64]. As for cuprate high temperature superconductors such as $YBaCu_3O_{7\text{-}x}$, several reports suggested that the superconducting transition can be induced by (de)oxygenation of these materials by means of IL gating [62, 63], while others suggested an electrostatic mechanism [60]. Dubuis *et al.* [64] argued that the electric field of the electric double layer drives a redistribution of the oxygen atoms in the basal planes of the cuprate in an electrostatic fashion, while others have suggested an electrochemical process leading to oxygenation of the cuprate [62, 63]. In this work, we attempt to address the mechanism of the IL gating of the cuprate material of $La_{2\text{-}x}Sr_xCuO_4$.

6.2 Experimental details

The $La_{2\text{-}x}Sr_xCuO_4$ films are grown on single crystalline $LaSrAlO_4(001)$ or $(LaAlO_3)_{0.3}(Sr_2AlTaO_6)_{0.7}(001)$ substrates (0.05-0.3° miscut), for these have a small mismatch in the lattice constants with respect to $La_{2\text{-}x}Sr_xCuO_4$ (0.5 %). The substrates were annealed at a temperature of 1050 °C for 10 or 12 hours under a flow of O_2 of 50 mL/min to remove any organic materials on the surface of the substrate and to allow reconstruction of surface defects. When scanned with atomic force microscopy (AFM), the substrate surface shows clear steps of half a unit cell (UC) height (Fig. 6.1a), which is expected for a double termination of the substrate lattice, and has a root mean square (rms) roughness of 0.23 nm.

We use Pulsed Laser Deposition combined with Reflection High Energy Electron Diffraction (RHEED) to grow the cuprate and monitor the growth in-situ. During growth the substrates are kept at a deposition temperature of 740 C and O_2 pressure of 0.13 mbar. The target is ablated using a laser fluence of ~ 1.65 J/cm^{-2} and repe-

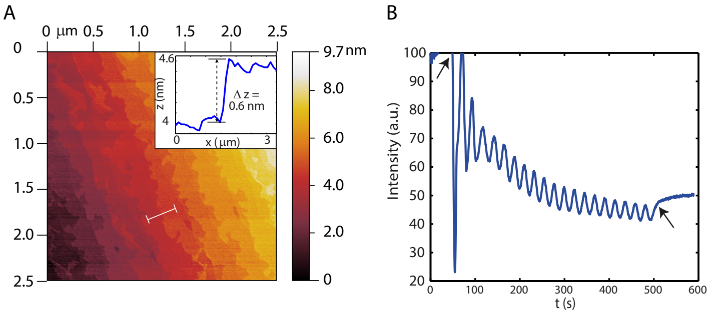

Figure 6.1: (**a**) Example of an AFM image of an annealed $LaSrAlO_4$ (001) substrate (1050 C, 10 hours) showing clear steps. The inset shows the height profile of one step, indicating the step height is half a UC. This is due to the double termination of the substrate UC. The rms roughness is 0.23 nm. (**b**) Graph of RHEED intensity vs. time which shows the oscillations of the specular reflected beam for the growth of a 10 UC thick $La_{1.95}Sr_{0.05}CuO_4$ (Sr doping is 0.05) on $LaSrAlO_4$. The oscillations are typically preserved up to the 20^{th} RHEED oscillation and are indicative of layer-by-layer growth of the cuprate. The arrows indicate the start and end of the deposition process.

tition rate of 4 Hz. The RHEED oscillations, as seen in Fig. 6.1b, indicate layer-by-layer growth, where two RHEED oscillation periods indicate the growth of 1 UC [60, 143]. The thickness of the grown $La_{2-x}Sr_xCuO_4$ film is between 10 and 30 UCs, while x varies from 0.05 to 0.09. When Au for the electrodes is deposited ex-situ by a photolithographic process the adhesion of the Au electrodes is poor and the Au layers detach with the lift-off step. To prevent this we have attempted to introduce a thin Ti adhesion layer before depositing Au. However, this introduces high contact resistances, about 100-1000 times the sheet resistance and further diverging at low temperatures, rendering measurements at low temperatures problematic. We suspect that the deposition of Ti leads to oxidization, inducing oxygen diffusion from the $La_{2-x}Sr_xCuO_4$ layer to the Ti layer. In turn, this leads to a decrease of charge carriers, which is detrimental for the conductive properties. Another reason may be the difference in work function of Ti (4.33 eV) and $La_{2-x}Sr_xCuO_4$ (5.02-5.23 eV [230]), leading to a Schottky-like barrier. The problem was resolved by *in-situ* deposition of a full Au layer with a typical thicknesses of 50 - 90 nm immediately following $La_{2-x}Sr_xCuO_4$ deposition, at an Ar pressure of 2×10^{-2} mbar, using a laser fluence of ~ 4 - 4.5 J/cm^2 and a repetition rate of 4 Hz, see Fig. 6.2a(I). The second process involves a photolithographic step in which areas are defined separating the

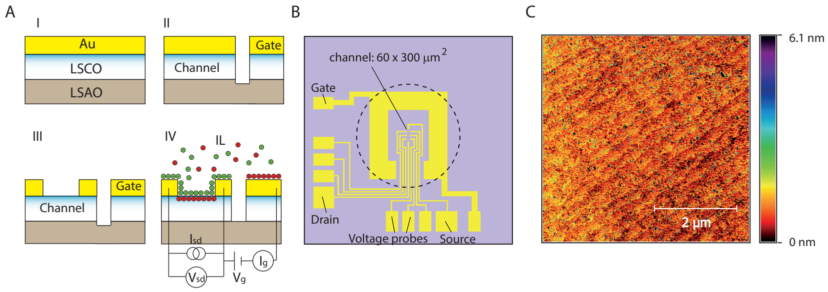

Figure 6.2: (**a**) Schematics of the sample preparation. I) After in-situ pulsed laser deposition of 10 to 30 UC of $La_{2\text{-}x}Sr_xCuO_4$ (LSCO) on a $LaSrAlO_4$ (LSAO) substrate, followed by Au deposition. II) After dry etching of the areas defined by photolithography. III) After wet etching of the excess Au between the source and drain electrodes using a $KI/I_2/H_2O$ solution. IV) Schematic representation of the electronic circuit of the IL/$La_{2\text{-}x}Sr_xCuO_4$ system. (**b**) Schematic representation of the used electrodes and channel layout (60×300 μm^2). Here, the voltage probe separation at the channel area is 60 μm. The dashed circle represents the approximate cross sectional area of the IL droplet at the sample surface. (**c**) An example of an AFM image of the surface of the $La_{2\text{-}x}Sr_xCuO_4$ channel (10 UC) after fabrication, before adding the IL. The film rms roughness is 0.49 nm, and clear steps of the film are visible.

gate from the active device area, followed by an dry etching step in an Ar^+ ion beam at 500 kV, see Fig. 6.2a(II). During this step, the areas for the Au electrodes needed for measurement and wire bonding, together with the $La_{2\text{-}x}Sr_xCuO_4$ channel area are protected by the photoresist. Exposing the channel area requires a third process, illustrated in Fig. 6.2a(III), in which the Au on top of the channel is etched away selectively using a $KI/I_2/H_2O$ solution (mass ratio 4:1:40). We find that this wet etching process preserves the quality of the $La_{2\text{-}x}Sr_xCuO_4$ film and surface.

In most cases, processes I, II and III leave behind photoresist residuals on the $La_{2\text{-}x}Sr_xCuO_4$ surface. To remove these residuals, we have attempted to etch the samples in an oxygen plasma (13-16 W, 100 mTorr). However, we find that this process modifies the properties of the cuprate film, inducing an n-type FET transistor-like behavior upon IL gating. In other words, the conduction increases at positive gate voltages and decreases at negative gate voltages, while the opposite, p-type transistor behavior is expected for $La_{2\text{-}x}Sr_xCuO_4$. This problem can be circumvented by gently cleaning the surface using an ethanol wetted lens tissue, resulting in an atomically clean surface of the $La_{2\text{-}x}Sr_xCuO_4$, as is shown in Fig. 6.2c.

A typical layout of the IL/$La_{2\text{-}x}Sr_xCuO_4$ sample, which is electrically wire bonded to a sample holder of the cryogenic insert, is shown in Fig. 6.2a(IV). We have used two Keithley 2450 SourceMeters for the experiments, one of which is used to apply a gate voltage V_g between the gate and drain electrodes, while simultaneously measuring the gate current I_g used for cyclic voltammetry, i.e. measuring the gate current I_g as a function of V_g in order to check for the presence of Faradeic processes characterized by charge transfer peaks. The gate voltages used in the experiment described in this work lies between -5.5 V and 0 V. The other Keithley SourceMeter is used for setting up an excitation current of 1 μA between the source and drain electrodes, while measuring the four-terminal resistance over the voltage leads. The $La_{2\text{-}x}Sr_xCuO_4$ channel has dimensions of 60×300 μm^2 and the voltage lead separation is identical to the channel width (see Fig. 6.2b), leading to a simple conversion factor for the sheet resistance. It is to be noted that the gate electrode surface area exposed to the IL is approximately 100 × the combined area exposed to the IL of the channel and electrodes (voltage probes, source and drain), in order for the entire gate voltage to fall over the IL/channel interface.

Before any usage of the IL for experiments, the bottle containing the liquid, i.e. N,N-diethyl-N-(2-methoxyethyl)-N-methylammonium bis(trifluoromethylsulphonyl)-imide (DEME-TFSI, IoLiTech, 99 %), is heated at 60 C overnight and then permanently stored in a N_2 glovebox ($\leq$ 0.1 ppm O_2/H_2O). In terms of electrochemistry, we observe that a mere exposure of the IL to pressures of a mere 10^{-1} mbar for 15 minutes is enough to completely remove the Faradeic peaks within the electrochemical window seen in ambient circumstances. Similarly, the same order of magnitude of pressure and the same IL used for FET experiments in the IL/ZnO system revealed no breakdown of the IL [109]. Still, the experimental atmosphere is pumped until a pressure of 1×10^{-4} to 10^{-6} mbar [231] to ensure that electrochemical processes due to water or oxygen present in the IL are minimized even further. To accommodate for the high, negative values of V_g used, we have lowered the temperature at which the gating is performed (charging temperature), based on the Ref.109, where it was found that this effectively widened the electrochemical window of the IL. In our experiments, the charging temperature is between 210 – 225 K, as low as possible, but above the melting point of 183 K of the IL. At these temperatures, we can apply a V_g as negative as -5.5 V without device degradation and dielectric breakdown, linked to the decreased electrochemical activity of the IL. The typical polarization times used in this work are 15 minutes.

6.3 Experimental results

We first present $R(T, V_\mathrm{g})$ curves for films grown on $\mathrm{LaSrAlO_4}$. We observe that IL gating induces superconductivity in $\mathrm{La_{1.95}Sr_{0.05}CuO_4}$, even when the film has a thickness of 30 UC (Fig. 6.3a). At 0 V, the curve shows the expected characteristic for a Sr doping of 0.05, for which the sample at 1.5 K is at the verge of superconductivity. At gate voltages down to -3.5 V, there is no substantial change with respect to the reference curve. However, when the gate voltage is -4.0 V or below, a superconducting state emerges, with the T_c extendable up to 12.0 K (onset) or 19.5 K (midpoint) at $V_\mathrm{g} = -5$ V. The inset of Fig. 6.3a shows an $I(V)$ curve (T = 1.6 K, $V_\mathrm{g} = -5.0$ V) having a critical current of approximately 0.3 mA. Thinner samples (10 UC) demonstrate an initial critical temperature T_c already before gating which we attribute to the compressive stress exerted on the film (Fig. 6.3b). As is the case for 30 UC films, the reference midpoint T_c of 13.5 K is barely altered at gate voltages down to -3 V. The T_c can only be increased with sufficiently large negative gate voltages of -4 V or lower, where the gate lowest gate voltage of -5 V results in a superconducting midpoint temperature of 30.4 K.

A first step towards investigation of the gating mechanism involves measuring the sheet resistance $R(V_\mathrm{g})$ characteristics, as is shown in Fig. 6.4 for a typical 30 UC film of $\mathrm{La_{1.91}Sr_{0.09}CuO_4}$ grown on the substrate $\mathrm{(LaAlO_3)_{0.3}(Sr_2AlTaO_6)_{0.7}}$. We make two main observations on the charging loop, namely the absence of hysteresis (apart from a small instrumental time delay) and a linear response of the resistance of the film as a function of gate voltage. The first observation is characteristic of an electrostatic mechanism, as has been observed before, e.g. in IL-gated indium tin oxide films [64]. This is also consistent with the linear response of the resistance. We can quantify the effects of gating by assuming that the sample can be thought of as having a top and bottom layer. The latter is not affected by gating and has a fixed charge carrier density n_0. The top layer is in contact with the IL and has a charge carrier density n_t which is V_g dependent,

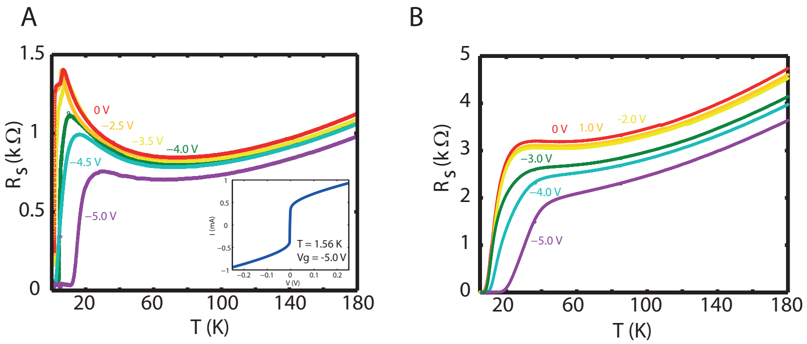

Figure 6.3: (**a**) Sheet resistance R_S plotted against temperature T for various V_{g} for a 30 UC thick $\mathrm{La}_{1.95}\mathrm{Sr}_{0.05}\mathrm{CuO}_4$ sample. At V_{g}=0 V, the $R(T)$ characteristic shows that the sample is nearing superconductivity at the lowest T of 1.6 K. This pattern persists for V_{g} down to $V_{\mathrm{g}}= -3.5$ V. Applying a lower V_{g} leads to the emergence of superconductivity with T_c growing to 12.0 K when $V_{\mathrm{g}} = -5$ V is applied. The inset shows an $I(V)$ curve at T=1.6 K and V_{g}=−5 V. (**b**) Similar data for a thinner sample of 10 UCs, where the superconducting state is extended in T_{c} only for V_{g} below −3 V.

and we expect this dependence to be linear, $n_t(V_{\mathrm{g}}) = n_0 - \beta V_{\mathrm{g}}$. This relationship has a negative slope due to the fact that $\mathrm{La}_{2\text{-}x}\mathrm{Sr}_x\mathrm{CuO}_4$ is a hole-doped material. The proportionality constant β is positive and is proportional to the gate efficiency between the IL and the top layer. Here, $\beta = \eta \frac{C_{\mathrm{EDL}}}{e d_t}$, where η is the electrostatic gate efficiency, while C_{EDL} is the specific capacitance of the interface to DEME-TFSI, e is the electron charge and d_t is the top layer thickness. Under ideal circumstances, $\eta = 1$. Since the observed resistance change is small we take the resistance to be proportional to the charge density and linearize around $V_{\mathrm{g}} = 0$, which results in $R(V_{\mathrm{g}}) = R_0 \left(1 + \frac{\beta d_t}{n_0 d} V_{\mathrm{g}}\right)$. Specifically, R_0 is the value of the resistance of the $\mathrm{La}_{1.91}\mathrm{Sr}_{0.09}\mathrm{CuO}_4$ channel without applying a gate voltage. Using the slope of the curve, $\frac{\Delta R}{\Delta V_{\mathrm{g}}} \simeq 2.4\Omega/\mathrm{V}$, we obtain an indication of the gate efficiency η, defined as $\eta = \frac{\Delta R}{\Delta V_{\mathrm{g}}} \frac{e n_0 d}{R_0 C_{\mathrm{EDL}}}$. The sample thickness corresponding to the curve in Fig. 6.4 is 30 UCs (50 nm), while the carrier density $n_0 = 9.6 \times 10^{20}$ cm^{-3} [232] and $C_{\mathrm{EDL}} = 13$ $\mu\mathrm{Fcm}^{-2}$ [222], resulting in $\eta = 0.15$. In other words, while the IL gating is electrostatic in this range, the efficiency of gating is only at about one seventh of its optimal efficiency. This means that a large part of the charge build-up in the electric

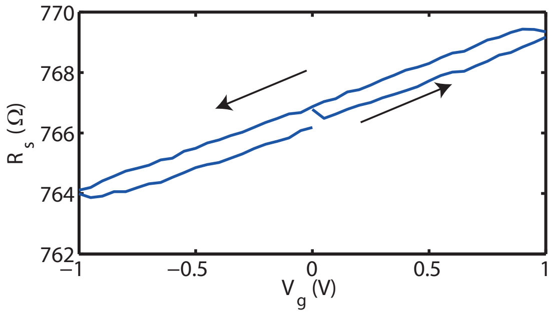

Figure 6.4: Typical sheet resistance R_S plotted against gate voltage V_g for a 30 UC $La_{1.91}Sr_{0.09}CuO_4$ film grown on $(LaAlO_3)_{0.3}(Sr_2AlTaO_6)_{0.7}$. In the given V_g range, hysteresis is absent (apart from a small instrumental time delay) and we observe a linear relationship having a positive slope, coinciding with hole (electron) doping for negative (positive) gate voltages. The sweep rate is 50 mV/s, while the polarization temperature is 225 K.

double layer does not translate to conductivity. We suspect that this is due to the finer details of crystalline quality of the $La_{2-x}Sr_xCuO_4$ film, such as the roughness and presence of grain boundaries. This is supported by reports of IL gating on different crystalline qualities of FeSe films in Ref.233. Here, the authors state that an improved crystallinity and an atomically flat surface can lead to a more optimal charge transfer during the gating process. In a preliminary series of experiments we found that the smoothness of the film surface can be improved following the recipe by Bollinger *et al.* [10]. By introducing a 1 UC buffer layer of nominally metallic $La_{1.70}Sr_{0.30}CuO_4$ $La_{2-x}Sr_xCuO_4$ films of thicknesses of up to 7 UC show an improved smoothness of the surface in the AFM images, and a substantially higher gating efficiency up to $\eta = 0.65$.

The gating mechanism was investigated further by altering the gate voltage in steps, while measuring the sheet resistance of a 30 UC $La_{1.91}Sr_{0.09}CuO_4$ film grown on $(LaAlO_3)_{0.3}(Sr_2AlTaO_6)_{0.7}$ as a function of polarization time, typical results of which are illustrated in Fig. 6.5a. Two processes are observed upon switching the gate voltage in a step-wise fashion to higher negative values: 1) a nearly instantaneous process which results in the drop of the sheet resistance of the film, and 2) a relatively slow process, requiring several hours to stabilize, becoming most pronounced in the gate voltage regime of −3 V and lower. The first process requires less than 1 second and only produces a limited drop in sheet resistance of $\sim 2\ \Omega/\mathrm{V}$ for the gate voltages used, which agrees with the rate found on the basis of Fig. 6.4. The second process only becomes prominent at gate voltages below −3 V, and produces a very pronounced effect in the sheet resistance of the film of up to hundreds of Ω.

Both processes are nearly reversible. After returning to zero gate potential the sheet resistance relaxes to within a percent of the initial value. However, a new cycle of increasing steps of negative gate potential shows that the slow process has become more active. The enhancement of the slow process continues in subsequent cycles, but the changes become smaller and the lowest attained resistance saturates. Fig. 6.5b shows that the slow decrease of the resistance is associated with a gradual shift of the superconducting transition temperature, confirming that it involves a process of hole doping of the copper oxide layer. For higher negative gate potentials at longer polarization times the resistance starts to increase, leading to an irreversible deterioration of the film.

6.4 Discussion

At the polarization temperature at which these measurements were performed (225 K) the build-up time of the electric double layer on the channel should occur within an RC time determined as $R_{\mathrm{IL}}C_{\mathrm{EDL}}$. Here, R_{IL} is the electrical resistance of the IL, which is of the order of $10^8\ \Omega$ [98]. The electric double layer capacitance C_{EDL} is determined by the specific capacitance of the IL (13 $\mu\mathrm{Fcm}^{-2}$) and area of the $\mathrm{La}_{2\text{-}x}\mathrm{Sr}_x\mathrm{CuO}_4$ channel ($300 \times 50\ \mu\mathrm{m}^2$), giving $C_{\mathrm{EDL}} \simeq 2$ nF. The estimated RC time becomes of the order of 1 second. Hence, we conclude that the relatively quick process in the resistance behavior is the contribution of the electrostatic mechanism of gating. The second, much slower process does not behave according to this electrostatic RC time.

Some processes which can be capacitive or Faradaic in nature tend to be considerably slower compared to the EDL charging time. These are often related to the reconstruction phenomena and ordering effects of the ions of the EDL [234, 235]. Furthermore, the processes of this origin tend to become extremely slow at the used charging tempera-

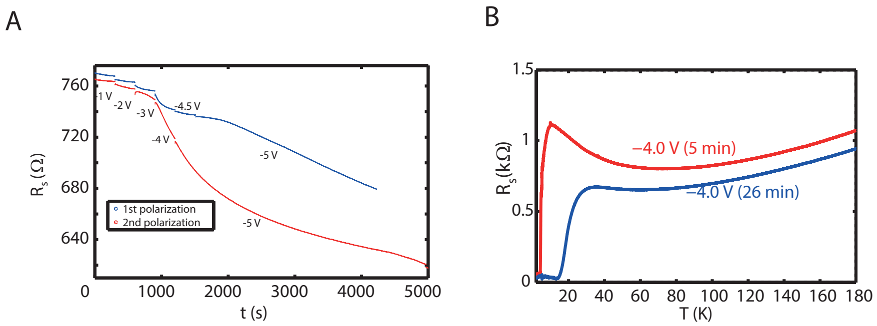

Figure 6.5: (**a**) Evolution of the sheet resistance R_S of a 30 UC $La_{1.91}Sr_{0.09}CuO_4$ film grown on $(LaAlO_3)_{0.3}(Sr_2AlTaO_6)_{0.7}$ as a function of time, while the gate voltage is switched to increasing negative values at the points indicated. (**b**) Temperature dependence of the sheet resistance R_S for different polarization times and for the first and second polarization at $V_g = -4$ V. The midpoint T_c increases from 5 K to 17 K for polarization times of 5 and 26 minutes, respectively.

tures [190], many orders of magnitude slower than what is observed in our experiments. We therefore conclude that the observed slow process involves another, non-electrostatic mechanism.

Since the Sr doping of the film is constant, the change in T_c could be caused by an increased interstitial oxygen doping of the film, as interstitial oxygen is well-known for its role in changing the charge carrier density in the CuO_2 planes and hence superconductive properties of $La_{2\text{-}x}Sr_xCuO_4$ [6, 147]. This behavior has been reported before in the IL-gating of $YBa_2Cu_3O_{7\text{-}x}$ films [62, 236], where it was interpreted as an electric field driven slow redistribution process of the oxygen atoms in the copper oxide planes of the film [63, 236].

We observe a crossover at around −2 V, where both components have the same contribution in resistance change. For more negative gate voltages the non-electrostatic component starts to dominate. The non-electrostatic component can lead to a substantial change of the onset of T_c (13.7 K to 25.0 K) as a function of the polarization time at a constant gate voltage of −4 V (Fig. 6.5b). In case only electrostatics would be at play in the gating of $La_{2\text{-}x}Sr_xCuO_4$, no change in T_c is expected, as the polarization time for both curves is beyond the RC time of the system.

The interpretation of the slow process as an ionic process is further supported by $I_g(t)$ measurements, a typical example of which is shown in Fig. 6.6, taken at $V_g \leq -3$ V. In the case of a diffusion-limited charge transfer processes it is known that the gate current under potentiostatic conditions varies according to the Cottrell equation $I_g(t) = FcA\sqrt{D}/\sqrt{\pi t}$. Here, F is Faraday′s constant, while c is the concentration of the electroactive species, A is the electrode area and D is the diffusion constant of the particles. As observed in Fig. 6.6, after an initial fast process the gate current eventually follows the $t^{-\frac{1}{2}}$ dependence of the Cottrell equation, the slope of which is 5.2×10^{-9} As$^{-1/2}$. Let us assume that the added oxygen is provided from the lower layers of the film. The concentration in the active top layer after a given time can be estimated from the observed optimal $T_c = 25$ K (onset) at this gate potential of $V_g = -4$ V. Using the known variation of T_c with hole doping for this compound the oxygen content is estimated as $\delta \approx 0.10$ [147]. Using the density of the cuprate material, c then becomes approximately 1.7×10^{-3} mol cm^{-3}. Accordingly, through the Cottrell equation we obtain a number for the diffusion constant, $D = 1.6 \times 10^{-14}$ cm^{2}s, which is similar to values known in the literature for electrochemical oxidation of La_2CuO_4 at room temperature [237, 238]. Alternatively, when assuming that the added oxygen is added from outside the film, i.e. from the ionic liquid, c becomes very small, $c \sim 1 \times 10^{-14}$ mol cm^{-3}, since the partial pressure of oxygen in the IL is limited by high vacuum conditions. As a result the diffusion constant becomes anomalously high, $D \sim 1 \times 10^2$ cm^{2}s, inconsistent with the viscous state at the used polarization temperatures near the glass transition.

Other electrochemical processes can cause a change in the doping of a material. For example, hydrogen doping is known in La_2CuO_4, $YBa_2Cu_3O_7$ [239], and other oxides such as VO_2 [69]. Protonation is also reported in TiO_2[225] and WO_3 [97]. Although trace amounts of both hydrogen and protons can be present in the IL, both processes are unlikely to happen. Protonation would diminish the hole density of the film and thus decrease the T_c, which is not observed, whereas hydrogenation would also decrease the T_c for the Sr doping used in this study [239].

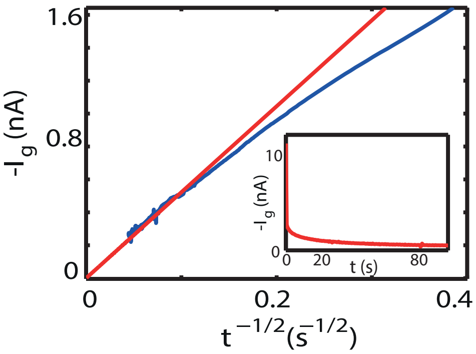

Figure 6.6: Plot of the gate current I_g against against $t^{-\frac{1}{2}}$. The behavior follows the Cottrell relationship for diffusion-limited electrochemistry. Inset: $-I_g$ vs. t. The polarization temperature is 210 K at $V_g = -4$ V.

6.5 Conclusions

In summary, our results emphasize the role of electrostatic and non-electrostatic processes in different gate voltage regimes and different crystalline qualities of $La_{2-x}Sr_xCuO_4$ films. Compared to the IL-gating of the band insulator $SrTiO_3$, for example, the electrostatic mechanism has a negligible effect in the total charge induction in the films, amounting to less than 15 %. We suspect that this small electrostatic contribution is primarily controlled by the surface crystalline quality parameters such as surface roughness and presence of grain boundaries. The non-electrostatic process is significantly slower than the expected RC times of the system. From this we conclude that this process most likely involves oxygen doping of the film. The diffusion constants extracted for this process support an interpretation in terms of the oxygen being provided from the lower layers of the film, rather than from the outside. These results are in line with previous IL gating and x-ray absorption measurements [63, 64], and will be important in forming a proper understanding for further exploration of this rapidly developing field.

Chapter 7

Etched junctions

In this chapter a new method of making (quasi) ab-axis Josephson junctions is explored, for which bilayers of $YBa_2Cu_3O_{7-\delta}/La_{2-x}Sr_xCuO_4$ *are used. Etching away the top layer ensures that the flow of electrons between both* $YBa_2Cu_3O_{7-\delta}$ *leads is through the* $La_{2-x}Sr_xCuO_4$ *area. The results show first indications of a long-range proximity effect.*

7.1 Introduction

Since its discovery, cuprate high-temperature superconductivity continues to be a field of interest in condensed matter physics. Several questions are still unanswered, most notably the pseudogap phenomenon. The characteristic energy gap present in cuprate superconductors persists above the critical temperature T_c. Although the nature of the pseudogap is under debate, the most prominent interpretations are that it results from, first, a pairing of the charge carriers with the superconducting coherence being suppressed due to phase fluctuations [240], or, second, a gap structure of spin/charge density wave order that competes with superconductivity [241]. Interestingly, junctions made of a cuprate barrier material in its pseudogap phase have shown anomalous properties in the form of an extended Meissner state [7], and most notably the giant proximity effect (GPE)[6, 18, 20] leading to Josephson coupling many orders of magnitude larger than the nominal coherence length [5, 6]. While many interpretations have been proposed [20, 42], the question remains whether the GPE can be related to pseudogap physics and more specifically whether a statement can be made regarding the importance of phase coherence in the pseudogap state.

Until now, *c*-axis junctions have made the compelling cases in the experimental tests of this effect. The advantage is that these can be grown without secondary-phase participates and with an rms roughness below the thickness of the barrier material. For example, in junctions formed between superconducting $\mathrm{La}_{2\text{-}x}\mathrm{Sr}_x\mathrm{CuO}_4$, with a barrier made from the undoped compound $\mathrm{La_2CuO_4}$ [6, 7], supercurrents have been observed for barrier thicknesses up to 10 nm, roughly two orders of magnitude larger than the c-axis coherence length ξ_c, i.e. $0.1 - 0.2$ nm. The coherence length in the coplanar axes, ξ_{ab}, is typically in the order of a nanometer, which in principle could lead to a supercurrent preservation over a distance of several hundred nanometers [6, 242]. Hence, for such distances, the strict design and interface roughness criteria that hold for the *c*-axis geometry no longer are present. Although there have been many reports of *ab*-axis GPE [13, 14, 16], most of the devices were suspected to be plagued by microshorts [243, 244], leading to ambiguous findings of the GPE in this junction geometry.

The typical *ab*-axis junction geometry initially employed grain boundaries grown on bilayer crystals [245], or ramp junctions [246]. More recently, focused He-ion beam techniques [247] have been used to change the superconducting (S) properties of $YBa_2Cu_3O_{7\text{-}\delta}$ and induce superconductivity at a lower $T_{c'}$ (S'), or metallic (N) and insulating (I) properties. Combined with advanced lithographic techniques[248], the authors of Ref. 247 have shown to successfully produce SNS or SIS Josephson junctions. This was done with a 500 pm wide ionized beam, ensuring much smaller widths of the junction needed for SNS/SIS ab-plane configurations, as the $YBa_2Cu_3O_{7\text{-}\delta}$ coherence length in this configuration is ~ 2 nm. Interestingly, while the authors were able to decrease the T_c of the barrier material at will by adjusting the dose of the ion bombardment and hence make $SS'S$ junctions, they do not mention whether such a junction configuration induces any long range coherence lengths. Whereas the authors of Ref. 247 have used He-ion beam to change the properties of the layer into S', where S' is the same material, we have a bottom layer S' which is a different material than the top S layer. Ion irradiation (Ar+ instead of He+) is then used to completely remove the top S layer to end up with a $SS'S$ junction. More specifically, the ion irradiation is applied for bilayers of $La_{2\text{-}x}Sr_xCuO_4/YBa_2Cu_3O_{7\text{-}\delta}$ and we report supercurrent preservation in a quasi $ab-$axis geometry of ion etched junctions over distances of ~ 50 nm. Magnetic field measurements support the Josephson junction-type behavior of the devices.

7.2 Experimental details

Obtaining a giant proximity effect through etched bilayers requires a few conditions to be met. Firstly, a $T_{c'}$ should be present in the bottom film, which preferably should be as low as possible. Secondly, the T_c of the top layer should be as high as possible. Hence, bilayers have been made by (1) making use of bottom layers of less-than-optimal Sr levels (i.e. 0.09) of $La_{2\text{-}x}Sr_xCuO_4$ and (2) making use of $YBa_2Cu_3O_{7\text{-}\delta}$ as the top layer, as $YBa_2Cu_3O_{7\text{-}\delta}$ is known to have a substantially higher T_c than $La_{2\text{-}x}Sr_xCuO_4$ (bulk values of 93 K [133]), with which ΔT_c can be maximized. The T_c difference between both layers is then exploited by creating a junction that effectively removes the top layer locally by dry etching.

The bilayers are grown by means of pulsed laser deposition (PLD) with a KrF excimer laser on $LaSrAlO_4$ substrates (miscut angle of 0.2 degrees). The lattice mismatch (+0.5 %) facilitates layer-by-layer growth of the initial $La_{2\text{-}x}Sr_xCuO_4$ layer (see Fig. 7.1a(top)), monitored by reflection high energy electron diffraction (RHEED). The deposition of which is done with at 740 C at an O_2 pressure of 1.3×10^{-1} mbar and a laser fluence of 1.3 J/cm^2 at 4 Hz. The growth is maintained until the completion of the 30th unit cell (UC). The growth of $La_{2\text{-}x}Sr_xCuO_4$ is followed by that of $YBa_2Cu_3O_{7\text{-}\delta}$. The latter is grown at a slightly higher temperature and oxygen background pressure, 780 C and 2.0×10^{-1} mbar, respectively. Growing $YBa_2Cu_3O_{7\text{-}\delta}$ at a lower temperature near 720 C stimulates a-axis growth of $YBa_2Cu_3O_{7\text{-}\delta}$, which is unwanted. The laser fluence is 1.3 J/cm^2 with a repetition rate of 1 Hz, while the target-substrate distance is held at 50 mm. As can be seen in Fig. 7.1a, the clear oscillations for the first layer facilitated by a 2D growth mode are suppressed considerably with the growth of $YBa_2Cu_3O_{7\text{-}\delta}$, suggesting a 3D growth mode for this second layer. RHEED oscillations are typically unobservable after the completion of the 4th UC, accompanied by a spotty RHEED pattern. The $3D$ growth is likely due to limited mobility of the ablated material on arrival at the substrate surface [167]. After deposition, the bilayer is left at 700 C for 15 min at deposition pressure, followed by an oxygen annealing treatment at 600 and 450 C, both for 30 min at a cooldown rate of 10 K/min. The $YBa_2Cu_3O_{7\text{-}\delta}$ surface is coarsened (the typical roughness is around 1.4 nm, whereas the substrate roughness is 0.3 nm), and it is possible to see unit cell step heights on the surface of the 3D islands (see Fig. 7.1b).

The deposition steps of the bilayer are shown schematically in Fig. 7.2 a,1,2. This is followed by a Au deposition process at 100 C for minimal contact resistance (Fig. 7.2 a,3), as introduced in Chapter 6. The subsequent processing step involves spinning a layer of photoresist (Fig. 7.2 a,4) which is used to mask off a part of the Au (Fig. 7.2 a,5) against the subsequent wet etching process of the exposed Au by a $KI/I_2/H_2O$ solution (4:1:40 mass ratio) (Fig. 7.2 a,6). The residual photoresist is removed by a short rinse in an ethanol and aceton bath (Fig. 7.2 a,7). Next, the sample covered is by a PMMA layer (Fig. 7.2 a,8), and a small part of it, coinciding with the red areas in Fig. 7.2 b, is exposed to an electron beam and developed (Fig. 7.2 a,9). The sample is then Ar ion milled using an acceleration voltage of 500 V. The PMMA layer, being 240 nm thick, acts as an ion stopping layer and only the developed areas are etched away in the process (Fig. 7.2 a,10) and a subsequent aceton and ethanol rinse step (Fig. 7.2 a,11)

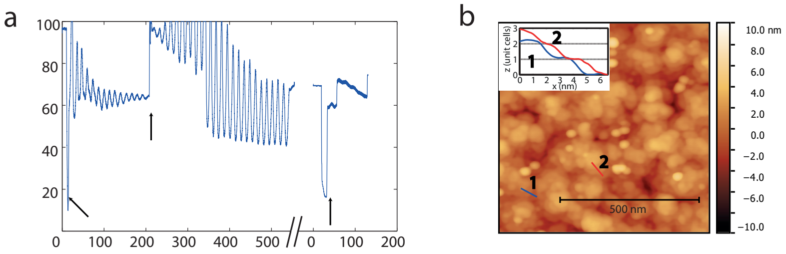

Figure 7.1: **(a)** RHEED specular intensity vs. time of 30 UC (60 RHEED oscillations) growth of $La_{1.91}Sr_{0.09}CuO_4$ and 6 UC of $YBa_2Cu_3O_{7\text{-}\delta}$. The initial $La_{1.91}Sr_{0.09}CuO_4$ grows layer-by-layer, as is indicated by the relatively large amplitude of the RHEED oscillations and the presence of the initial RHEED spots after completion of the layer. The growth of $YBa_2Cu_3O_{7\text{-}\delta}$ is characterized by a relatively small amplitude of the RHEED oscillations. The initial spots disappear and are replaced by transmission spots in the diffraction pattern, which indicate a coarsened surface. The arrows indicate the moments of electron beam current amplification, and the switch from deposition of $La_{1.91}Sr_{0.09}CuO_4$ to $YBa_2Cu_3O_{7\text{-}\delta}$ takes place at the break in the horizontal axis. **(b)** A typical AFM image of a bilayer film. The film is coarsened, with individual islands locally showing step heights corresponding to the $YBaCu_3O_{7\text{-}\delta}$ c axis lattice parameter, 11.7 Å.

concludes the sample fabrication process. The etch depth is homogeneous for all junctions being 32 ± 1 nm. Note that the ion irradiation also damages a volume extending beyond the etched volume, possibly making the $SS'S$ junction quasi planar, meaning that the current between both electrodes has a c-axis component along with its ab-axis component.

7.3 Experimental results and discussion

We observe an $R(T)$ which shows two superconducting transition temperatures, coinciding with the upper and lower layers of the bilayer. This shows that the supercurrent between both $YBa_2Cu_3O_{7\text{-}\delta}$ leads (34 nm) goes through the $La_{1.91}Sr_{0.09}CuO_4$ layer (39 nm). In the example shown in Fig. 7.3b, even though the etched depth is smaller than the thickness of $YBa_2Cu_3O_{7\text{-}\delta}$, the non-superconducting $YBa_2Cu_3O_{7\text{-}\delta}$ extends several nm beyond the etched depth due to ion irradiation damage, marked as red in Fig. 7.3b. The observation of two T_cs suggests that this non-superconducting layer extends into the bottom layer. Furthermore, some of the lower UCs of $La_{1.91}Sr_{0.09}CuO_4$

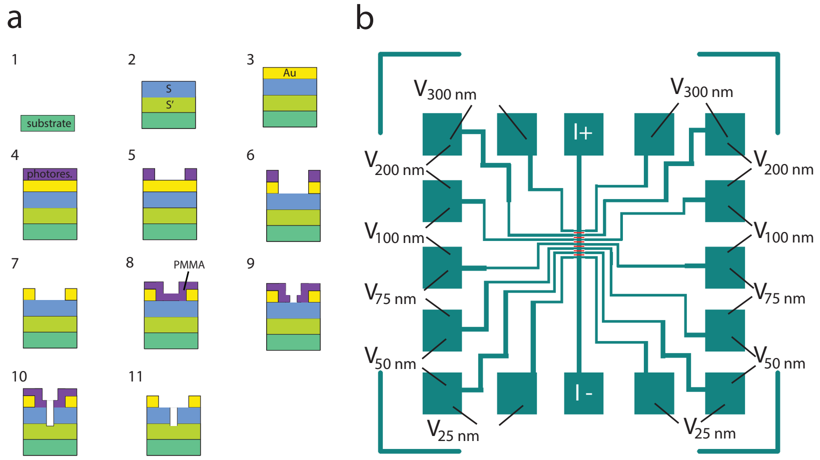

Figure 7.2: **(a)** Fabrication steps of quasi-coplanar etched junctions. 1) An initial substrate is used to 2) grow the bilayer of $La_{1.91}Sr_{0.09}CuO_4$ (*S'*) and $YBa_2Cu_3O_{7-\delta}$ (*S*), followed by 3) in-situ deposition of Au. 4,5,6,7) Photolithographic and wet etching techniques are used to open up the channel area. 8,9) A subsequent electron beam lithographic process is used to write and develop the junction areas. 10,11) A final Ar ion etching process is used to etch the exposed area. 11) A final aceton and ethanol rinse step is used to remove any lithographic residuals on the surface. **(b)** Photolithographic mask design of the sample used in the fabrication process. The red areas are exposed to the electron beam in a separate process. The chip in this example contains 7 junctions of nominal widths 25 nm, 50 nm, 75 nm, 100 nm, 200 nm, and 300 nm, that are formed in the *S* superconductor that extends from the I^- to the I^+ lead. The labels at the other contact pads indicate the positions of the voltage probes at either side of a junction of given width.

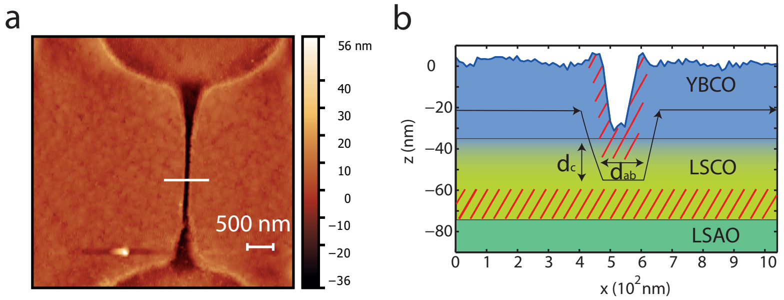

Figure 7.3: **(a)** AFM image of a typical ion milled junction geometry. The electrodes make contact with the top layer of $YBa_2Cu_3O_{7-\delta}$(the elevated plateaus left and right in the image). The gap between in the center of the image has a length of approximately 5 μm and the width slightly varies, having its narrowest part in the middle, which in this case is 47 nm wide over a length of approximately 3 μm long. The height profile of the white bar is shown in **(b)**. The etched depth is 30±1.0 nm in this case, which means that the $YBa_2Cu_3O_{7-\delta}$ is not completely removed. The volume of non-superconducting material as modified by the ion bombardment, however, extends up to and beyond the $YBa_2Cu_3O_{7-\delta}/La_{1.91}Sr_{0.09}CuO_4$ interface, shaded as red. The first UCs of bottom layer are also non-superconducting due to strain effects, which is illustrated by the red shading as well. The critical current of the leads in such a setup has both an c- and ab-axis components, indicated as d_c and d_{ab}.

are non-superconducting as well due to strain relaxation effects, estimated to be $d_{LSCO} \sim 10$ UC $= 20$ nm. This estimate is based on experimental data of strained $La_{1.91}Sr_{0.09}CuO_4$ films on $LaSrAlO_4$, which are semiconducting at least up to 7 UCs (see Section 3.3.4). Hence, the estimated c-axis depth (d_c) of the supercurrent path is between 0 and 20 UCs of the bottom layer, i.e. 26 nm. Future experiments aimed at obtaining the exact number should be done by using the same Ar ion method at $La_{1.91}Sr_{0.09}CuO_4/LaSrAlO_4$ films that are sufficiently thick. The change in critical current density then is representative of the effective reduced thickness of the superconducting layer of the film.

In Fig. 7.4a an $R(T)$ is shown for a junction width of 100 nm that is representative for the curves corresponding to all used junction geometries. The inset depicts $dR/dT(T)$ of the $R(T)$ to indicate the superconducting transition temperatures. The lower T_c measured as $d^2R/dT^2 = 0$ of 6.9 K agrees with that of $La_{1.91}Sr_{0.09}CuO_4$, while the upper T_c resembles that of $YBa_2Cu_3O_{7-\delta}$. The $R(T)$ dependence for $T \leq 25$ K is shown in Fig. 7.4b. We observe a remarkable junction width dependence of the T_c, depicted in the inset of Fig. 7.4b. For the 300 nm wide junction, $T_c = 6.8$ K, while the narrowest junction of 50 nm has the highest T_c of 9.0 K.

Next, the lowest T_c of 6.8 K is taken as a fair representation of the intrinsic T_c of the $La_{2\text{-}x}Sr_xCuO_4$ layer, which we will indicate as T_1. Although the mask design does not offer the capability to do reference measurements, these were performed separately on 7 $La_{2\text{-}x}Sr_xCuO_4$ layers of the same doping, thickness and preparation methods, which show similar values of T_c of 6.3±2.2 K. The modulation of the T_c in the junctions is taken as an anomalous effect. The anomalous effect is most pronounced for the 50 nm junction, having a $T_c = T_2$ of 9.0 K and a critical current of the junction that is 30 times larger than the critical currents observed in the wider junctions of 100 nm and 300 nm at 1.6 K.

The enhanced coupling between both superconducting leads over 50 nm is exceptional, even in a quasi-planar junction geometry. More specifically, the total path is approximately $2d_c + d_{ab}$, with d_c and d_{ab} the perpendicular and lateral distances of the current path, respectively. Although, d_c is unknown, $d_{ab} \approx 50$ nm ($\sim 20\xi_{ab}$) (see Fig. 7.3b). A more realistic value is larger than 50 nm due to ion damage not only in the lateral direction.

In experiments on junctions formed by only ion bombardment of $YBa_2Cu_3O_{7\text{-}\delta}$ [17], similar anomalous results were found over an array of Josephson junctions over distances of up to 960 nm. The authors claimed that the results might be explainable by enhanced Josephson coupling through percolating superconducting islands between two superconducting leads that are separated by a a distance much longer than the coherence length [36, 249]. The chain of superconducting islands might form a single Josephson junction, much like a percolative form of transport.

In contrast, for our bilayer junctions the role of a percolation path is much less likely, as all junctions show two superconducting transitions, which indicates that the flow of electrons goes through both layers. However, if some superconducting $YBa_2Cu_3O_{7\text{-}\delta}$ remains and forms a percolation path, one would expect to see a higher T_c for the shorter junction. The etched depth for the various junction geometries is identical within 1 nm, making this option unlikely, but not an impossibility.

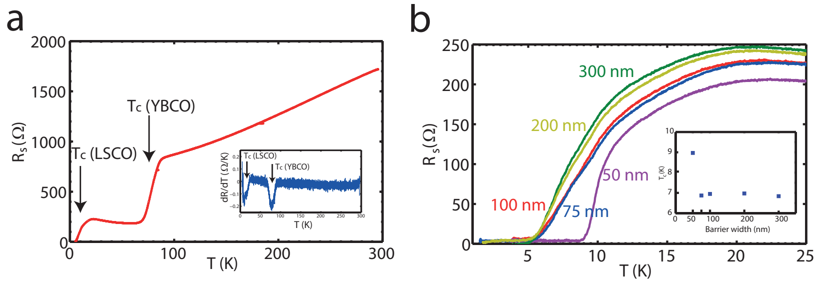

Figure 7.4: **(a)** $R_s(T)$ curve across a 100 nm wide junction which shows two transition temperatures of $\mathrm{La}_{2\text{-}x}\mathrm{Sr}_x\mathrm{CuO}_4$ (LSCO) and $\mathrm{YBa}_2\mathrm{Cu}_3\mathrm{O}_{7\text{-}}\delta$ (YBCO), as is indicated in the inset by the $dR/dT(T)$ curve. **(b)** $R(T)$ curve for $T \leq 25$ K for used junction geometries. The inset shows T_c given by $d^2R/dT^2 = 0$ as a function of junction width.

We aim to test whether the effect can be attributed to homogeneous Josephson coupling by means of magnetic field dependence of the critical current through the junction. The measurements were performed for the 50 and 300 nm wide junctions, with the magnetic field oriented perpendicular to the plane of the layers the data of which is shown in Fig. 7.5a. For a rectangular geometry and a homogeneous coupling we expect an oscillatory behavior in the critical current as a function of the magnetic field as a result of phase difference between both superconducting leads (Fraunhofer pattern) [250]. Measured values of the critical current for these measurements were done using a 1μV criterion. The expected oscillation period ΔB is equal to $\Delta B = \Phi_0/A$. Here, Φ_0 is the magnetic flux quantum and A is the junction area. Based on AFM images, the junction geometry is estimated to be 47 nm×5 μm, leading to $\Delta B \sim$8 mT.

For $T \leq T_1$ the complete bilayer is superconducting, and no oscillatory behavior is to be expected as no phase difference is formed between both ends of the junction. The behavior that is observed shows a persistent critical that is reduced by only about a factor of 2 at 20 mT for both widths of the junction (for the 50 nm junction the data below T_1 are only shown for positive fields). Remarkably, a different type of behavior is seen for the 50 nm junction that also has the enhanced T_c, and only in the range for $T_1 \leq T \leq T_2$ (Fig. 7.5b). The critical current in this range is very sensitive to the applied magnetic field, and shows a clear maximum at zero field along with structure

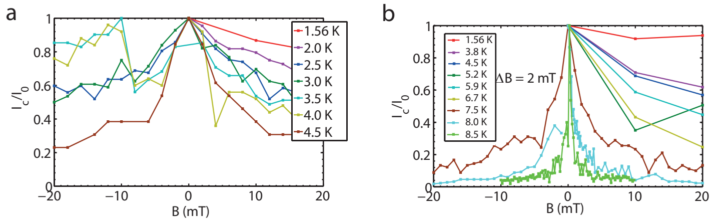

Figure 7.5: **(a)** Normalized I_c vs. magnetic field B for the 300 nm wide junction for different temperatures within the range $T \leq T_1$. The same is shown for the 50 nm for temperatures within the range $T \leq T_2$ in **(b)**.

suggesting side lobes with an oscillation period of ∼2 mT. Note that this period and the width of the central peak is comparable to the estimate given above, but smaller by about a factor of 4. For the effective area we need to include the London penetration depth of the $YBa_2Cu_3O_{7\text{-}\delta}$ superconductors on both sides, which is about 140 nm. Including the field penetration into the area we arrive at a new estimate of $\Delta B \simeq 1.2$ mT, which agrees quite well with the observed width of the peak. The fact that no more than 2 side lobes are visible per curve is an indication that the junction geometry is not sharply defined, which is also seen from the curved edges in the AFM images of Fig.7.3a. Given the limitations in the accuracy of the geometry, the agreement is quite good, and the experiment supports an interpretation of the junction as a Josephson coupling between the two $YBa_2Cu_3O_{7\text{-}\delta}$ superconductors, over a distance of 50 nm.

7.4 Conclusions

In summary, we report experiments on ion etched arrays of junction in bilayers of $La_{2\text{-}x}Sr_xCuO_4/YBa_2Cu_3O_{7\text{-}\delta}$ of widths varying from 50 to 300 nm. We show that it is possible to fabricate quasi *ab*-axis junctions by means Ar ion etching. A large T_c increase of the barrier material from 6.8 K to 9.0 K in the junction width of ∼ 50 nm is observed. The supercurrent in this junction geometry is preserved over a distance coinciding with ∼ 200 times the combined coherence lengths in the c and ab axes. The magnetic field measurements indicate clear difference in behavior of $I_c(B)$ between the 50 and 300 nm wide junctions, the former showing a clear main peak and several side lobes. These results support the Josephson junction-type behavior of the devices. The limitations in the accuracy by which the junction fabrication parameters, notably the etch depth profile, are known form the main obstacle for a more quantitative analysis.

Chapter 8

Towards an ionic liquid induced *ab*-axis giant proximity effect in continuous $La_{2\text{-}x}Sr_xCuO_4$ junctions

The giant proximity effect has been an unconventional and puzzling part of high temperature superconductivity. It can lead to proximitized coupling between two superconducting leads over distances much larger than allowed by the conventional proximity effect. In this chapter, we report techniques and preliminary results of ionic liquid-induced long-range proximity effect on a continuous $La_{2\text{-}x}Sr_xCuO_4$ *film. Our results show that the proximity effect in the ab axis can extend over two orders of magnitude larger than the coherence length of the cuprate.*

8.1 Introduction

Cuprate superconductors have brought many controversies. Notably, the proximity effect in specific cuprate Josephson junctions has initially been observed to behave differently [13–16] than in their conventional superconductor Josephson junction counterparts. With the advent of advanced growth techniques [5], this anomaly has been confirmed [6, 7] and consequently termed the giant proximity effect (GPE). It is suggested that its explanation can be coupled to another controversial topic, namely the pseudogap, seen by some as a precursor to superconductivity [251], while others view it as a competition of different phases with the superconducting phase [252].

The GPE seems to appear in $SS'S$ junctions, with the S' barrier having a lower $T_{c'}$ than the S leads by means of doping, as shown in $La_{2\text{-}x}Sr_xCuO_4/La_2CuO_{4+\delta}/La_{2\text{-}x}Sr_xCuO_4$ c-axis [6]. In such a setup, a supercurrent could be measured at $T_{c'} < T < T_c$ over a distance of up to two orders of magnitude larger than the normal coherence length of S', being 0.25 nm. No such long-range proximity effect was observed for $\delta = 0$. Long-range effects have also been observed in the vicinity of Pb islands on a Pb/Si(111) [21]. With spectroscopic methods using Scanning Tunneling Microscopy, the Pb monolayer locally was found to have a proximity-induced superconducting order parameter above its own bulk critical temperature.

Our interest is twofold. First, the coherence length in $La_{2\text{-}x}Sr_xCuO_4$ along the ab-axis is 3.2 nm [82]. Hence, the expected proximity length is expected to last 100s of nm. Second, we want to induce this effect using novel ionic liquid (IL) gating techniques. The advantage of using ILs lies in the formation of an electric double layer on the channel surface. The anion/cation separation when applying a gate voltage over the IL is $\sim$ 1 nm, leading to a huge electric field, enough to induce charge carrier densities of 8×10^{14} cm^{-2} [109], comparable to the 2D charge carrier densities in cuprates. Hence, this techniques has been used to induce superconductivity in cuprates [10, 66]. This method would then allow us to induce this GPE without having to make a discontinuity in the film. In this chapter we present techniques and preliminary results of a long range effect on a continuous $La_{2\text{-}x}Sr_xCuO_4$ film along the ab-axis using IL gating.

8.2 Experimental details

We use pulsed laser deposition (PLD) in combination with reflection high energy electron diffraction (RHEED) for the growth of the S' layer $La_{2\text{-}x}Sr_xCuO_4$ ($x = 0.05/0.09$) on $(LaAlO_3)_{0.3}(Sr_2AlTaO_6)_{0.7}$ or $LaSrAlO_4$. The deposition proceeds in an oxygen pressure of 0.13 mbar, while the laser fluency used is 1.5 J/cm^2 (Fig. 8.1a,1). To stimulate the growth to become layer-by-layer, we pause the deposition at each unit cell (UC) for 30 to 60 seconds for the layers to recrystallize before the next deposition of the next UC [143]. By doing so, RHEED oscillations can be observed up to the eventual film thickness of 30 UCs. As the sample is oxygen deficient at deposition, we increase the oxygen pressure after deposition to 0.6 mbar and cool the sample down at a rate of 10 C per min, while waiting at 600 C (15 min) and at 450 C (30 min) (Fig. 8.1a,2). Next, the cuprate film is in-situ covered by a 70 nm layer of Au, again by means of PLD (Fig. 8.1a,3). For this process, we use a deposition pressure of 0.2 mbar of Ar and a laser fluency of 4.0 J/cm^2. Photolithography (Fig. 8.1a,4+5) in combination with a $KI/I_2/H_2O$ (mass ratio 4:1:40) solution is used for the exposure of the channel (50 x 300 μm^2) by wet etching the exposed Au layer (Fig. 8.1a,6). The subsequent steps involve e-beam lithography, as shown in the inset, used to design the AlO_x line that will form the barrier. The design of the AlO_x layer starts with an electron beam step involving an electron dose exposure of 300 μC/cm^2 in the PMMA layer of approximately 240 nm thick (Fig. 8.1a,6,ii). The exposure involves two rectangular shapes (2 x 48 μm^2)) connected by a line that will form the barrier (0.025-0.3 x 4 μm^2), as shown in the schematic topview of the channel area (Fig. 8.1a,6,iii). After development, the written structures are checked by Atomic Force Microscopy (AFM), followed by another process involving the deposition of AlO_x (Fig. 8.1a,6,iv) and a lift-off step (Fig. 8.1a,6,v). After the lift-off (Fig. 8.1a,7), the thickness and width of the narrowest part of the AlO_x layer are again checked by AFM and subsequent photolithographic steps (Fig. 8.1a,8+9) are used to define areas that are to be dry etched (Ar, 500 V) (Fig. 8.1a,10). The lift-off of the resist is followed by a final check of the barrier by AFM, a typical result of which is shown in (Fig. 8.1b). As a final step, the sample is wirebonded and an IL droplet is put on the channel and gate electrodes. The IL is treated in vacuum conditions in the experimental setup and is pumped until a pressure of 1×10^{-4} to 10^{-6} mbar is reached before doing any measurements. This is to ensure that electrochemical processes due to water or oxygen present in the IL are minimized. For the same reason, the temperature at which gating (charging temperature) is performed is held between $210 - 225$ K, as low as possible, but above the melting point of DEME-TFSI (N,N-diethyl-N-(2-methoxyethyl)-N-methylammonium bis(trifluoromethylsulphonyl)-imide) of 183 K. We use two Keithley SourceMeters (2450) to apply a fixed current of 1 μA between the source (S) and drain (D) electrodes, while simultaneously measuring the voltage drop between these two electrodes, either by means of a two-probe or a four-probe configuration. Unless stated otherwise, the measurements performed in this work were based on the four-probe configuration. The distance between the voltage probes is such that the resistance of the channel is equal to the sheet resistance. The other SourceMeter is used to apply a gate voltage (V_g) between the gate and drain electrodes (Fig. 8.1a,11).

8.3 AlO$_x$ barrier characterization

We deposit a certain amount for the AlO$_x$ layer, which nominally coincides with an approximate thickness of 95 nm. For various barrier widths, the observed width and thickness of the AlO$_x$ barrier is plotted with respect to the designed width of the barrier in Fig. 8.2. We observe that both the observed width and thickness of the barrier do not agree with and vary approximately linearly with the designed width. The reduced AlO$_x$ deposition rate is mainly influenced by the aspect ratio between the thickness of the PMMA layer and the width of the structure developed into the PMMA layer, which is ~0.1 for the 25 nm wide barrier. The observed thickness of the AlO$_x$ barrier at the barrier with a width of 25 nm is 6.0 nm. In contrast, the aspect ratio is close to unity for the widest barrier for which the thickness is 65 nm, close to the maximum possible thickness. Furthermore, we observe a typical widening of the structure vs. the designed barrier width. Remarkably, the widening is not constant but increases as a function of designed width. This is probably due to an excessive electron dose which could lead to some widening effects during the writing or the development processes.

It is crucial for any IL-induced long-range Josephson junction effect to verify whether this is caused by a genuine giant proximity

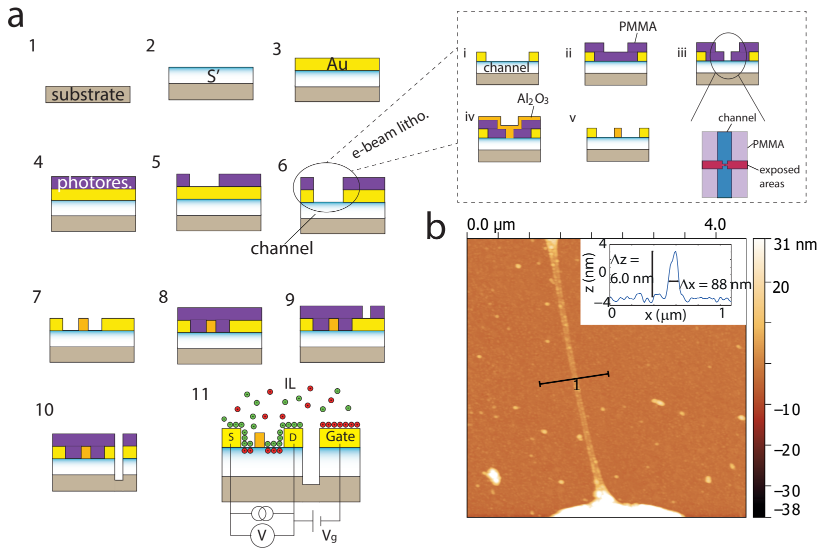

Figure 8.1: **(a)** A schematic overview of the sample fabrication and device setup. 1,2,3) PLD is used to grow La$_{2\text{-}x}$Sr$_x$CuO$_4$ and Au. 4,5,6) Photolithographic and wet etching techniques are used to open up the channel area. i,ii,iii,iv,v) Next, e-beam lithography is used to define the barrier. 7,8,9,10) The next photolithographic steps are used to define areas that are to be dry etched. 11) After this process, a lift-off step is followed by wirebonding. The sample is then covered by an IL droplet. **(b)** An AFM image of a 6.0 nm thick barrier of AlO$_x$ for a design width of 25nm.

effect. The IL gating could, in principle, also affect the barrier area in an unwanted way, for example when ion/oxygen diffusion from or to the barrier area starts to play a role. Firstly, the alumina layer should be sufficiently thick to increase the EDL separation under the barrier as the induced charge carrier density should scale inversely with the barrier thickness. The layers used in this work have a sufficiently large thickness, as the literature suggest a thickness of 2 [63] to 5 nm [72] is enough to minimize the electrostatic charge doping under the barrier area.

The stoichiometry of the AlO$_x$ could play a role in oxygen diffusion processes which could affect the $T_{c'}$ of the La$_{2\text{-}x}$Sr$_x$CuO$_4$ layer under the barrier in an unwanted way. The stoichiometry of the alumina is determined by the deposition parameters of oxygen pressure and target substrate distance [166]. Hence, we make sure that AlO$_x$ is de-

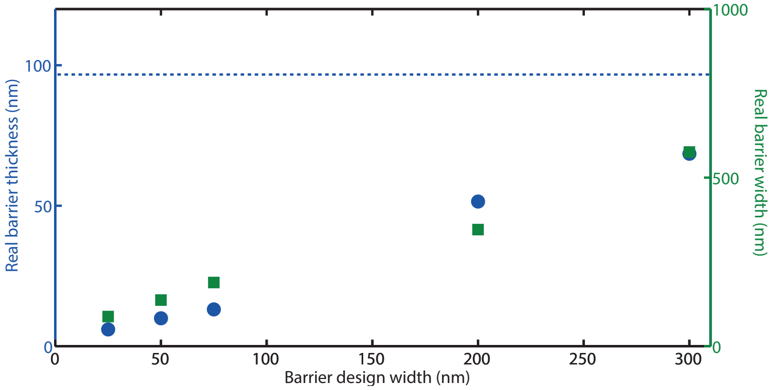

Figure 8.2: The real barrier thickness and width plotted vs. barrier design width using 1500 pulses, which nominally coincides with 95 nm (dotted blue line).

posited in a high oxygen pressure of 0.2 mbar along with a maximized substrate-target distance of 60 mm for optimal stoichiometric deposition to prevent oxygen diffusion from the film towards the AlO_x, as is the case with SiO_2 or SiN_3. We have observed that samples covered by the latter materials become deep insulators within a time span of days, presumably having to do with the capping layer inducing some oxygen gettering process from the cuprate lattice, rendering it an insulator. Alumina does not have this issue, as AlO_x films as thin as 2 nm have been recorded to be near-impermeable for oxygen diffusion [63].

Next, we show experimental data to suggest that IL gating does not influence the layer beneath. For this, a 35 UC $La_{1.95}Sr_{0.05}CuO_4$ channel is structured in a Hall bar configuration. Using electron beam lithography methods, one part of the channel is covered by a 100 nm layer of AlO_x (see Fig. 8.3a). Without any IL gating applied, the samples shows no superconductivity (see Fig. 8.3b) when measured over the area having no AlO_x top layer. Applying a gate voltage of -5.0 V approximately 30 minutes at 210 K, the resistance of the film is observed to be 30 % lower near the gating temperature and a superconducting transition is induced at lower temperatures, having a T_c ($R = 0$) of 18 K. In terms of IV characteristics, there is a clear difference when measuring the voltage drop at 1.6 K with and without the AlO_x barrier (see inset of Fig. 8.3b) below the T_c of the gated film. In the latter case, a critical current of approximately 450 μA is observed, while a linear response is measured in the former case. In other words, except for the area of film under the AlO_x barrier the whole film has turned superconducting, suggesting that the gating does not affect this area, at least not enough to induce superconductivity along with the rest of the film.

To investigate this further, we deposit a 100 nm thick layer of AlO_x on one side of a $La_{1.91}Sr_{0.09}CuO_4$ channel connected to a Hall bar electrode configuration (see Fig. 8.3c). We observe that minor changes are present in the $R(T)$ characteristics (Fig. 8.3d). The small differences could well be caused by inhomogeneities or size differences in the film. Furthermore, the T_c measured as the minimum in dR/dT is equal, i.e. 6.6 K (see Fig. 8.3d), which shows that the AlO_x layer does not influence the superconducting properties of the film.

8.4 Experimental results and discussion

With the seemingly neutral properties of AlO_x towards IL gating and the oxygen stoichiometry of the $La_{2\text{-}x}Sr_xCuO_4$ film, the gating process is expected to affect only the sectors of the film that are exposed to the IL. Typically, an eventual gate voltage between -5 and -5.5 V is applied in a stepwise fashion, while measuring the gate current and resistance of the film. In the specific example shown in Fig. 8.4, most of the effect is observed for gate voltages below -3 V, accompanied by a process which typically takes in the order of an hour to complete. This is slow compared to the RC time (~ 0.1 s) of the IL/$La_{2\text{-}x}Sr_xCuO_4$ system at these temperatures and has been observed in other IL experiments done on the cuprate $YBa_2Cu_3O_{7\text{-}\delta}$ [62, 63], and was linked to the oxygenation of $La_{2\text{-}x}Sr_xCuO_4$ [63]. This interpretation is further supported by diffusion-limited charge transfer behavior of the gate current, as also described in Chapter 6.

This specific sample has already a superconducting transition $T_c(R = 0)$ of 4.5 K at $V_g = 0$ (Fig. 8.5a). It has a 282 nm wide and ~60 nm thick AlO_x barrier in the same Hall bar-like configuration shown in Fig. 8.3a. By means of IL gating at -5.5 V the oxygenation leads to an increase of the T_c. Upon cooldown of the sample we observe two distinct critical temperatures, unlike before. The lower (higher) T_c is attributed to the S' (S) layer (un)covered by the AlO_x layer.

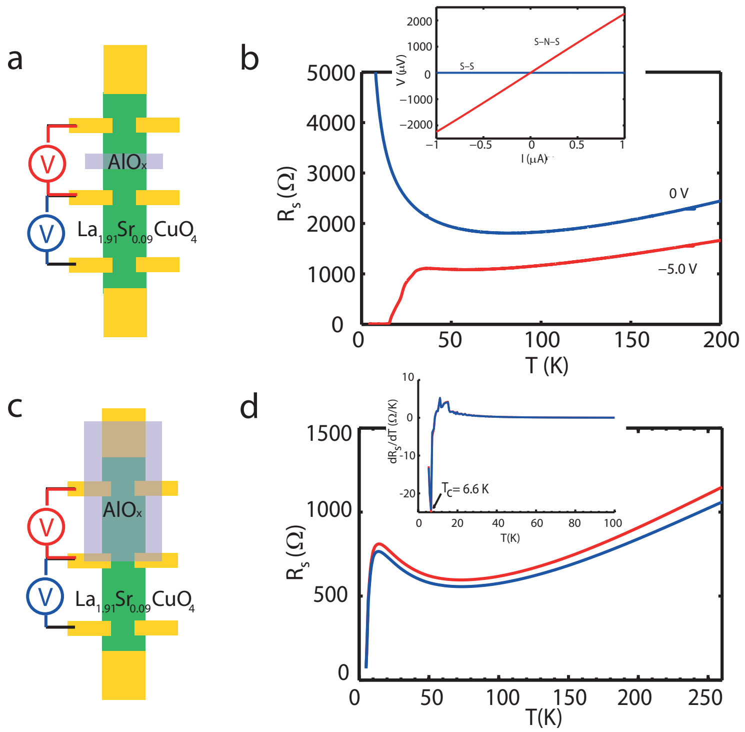

Figure 8.3: **(a)** Sheet resistance curves of a 35 UC $La_{1.95}Sr_{0.05}CuO_4$ film grown on $(LaAlO_3)_{0.3}(Sr_2AlTaO_6)_{0.7}$ before (blue) and after (red) gating at −5.0 V. **(b)** We observe semiconducting behavior at low temperatures initially, while after gating a superconducting transition is induced with a T_c $(R = 0)$ of 18 K. The inset shows I vs. V when measured across the superconducting leads of the channel without AlO_x barrier layer (blue) shows no voltage induced by the current, which confirms that the film is superconducting. The response is linear when the voltage drop is measured across the AlO_x barrier. **(c)** A four-probe measurement configuration for the purpose of quantifying the influence of a AlO_x on the superconducting properties of $La_{1.91}Sr_{0.09}CuO_4$ grown on $(LaAlO_3)_{0.3}(Sr_2AlTaO_6)_{0.7}$ in which one side of the channel is covered by the alumina. **(d)** $R(T)$ characteristics of both the covered (red) and unvcovered cuprate layer. The inset shows the dR/dT characteristics.

Remarkably, the initial $T_{c'}(R = 0)$ of 4.5 K before the application of the gate voltage increases to 9.5 K. Furthermore, we see a substantial increase in critical current by an order of magnitude (1.2×10^2 μA to 1.1×10^3 μA) at 2.0 K (Fig. 8.5b). The numerically calculated differential conductance dI/dV indicates the presence of peaks at ±1.6 mV,

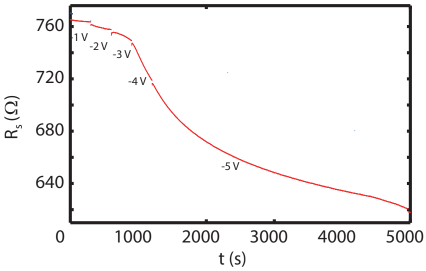

Figure 8.4: A typical time development of the sheet resistance of a 30 UC $La_{2\text{-}x}Sr_xCuO_4$ film ($x = 0.09$) grown on $(LaAlO_3)_{0.3}(Sr_2AlTaO_6)_{0.7}$ upon decreasing the gate voltage in step-wise fashion at a polarization temperature of 225 K. We observe that most of the gating effect happens below -3 V. The gating process takes $\sim$ 1 hour to complete, which is relatively slow when compared to the RC time of the IL/$La_{2\text{-}x}Sr_xCuO_4$ system ($\sim$ 0.1 s).

not observed before gating (Fig. 8.5c), although both show a large superconducting peak at zero bias. Here, the sharp zero bias peak represents the transmission of paired charge carriers between the S leads, while the two broad peaks are interpreted as transmission through transmission through Andreev bound states at voltages corresponding to Δ/e, typical for SNS junctions [247, 253, 254], with Δ the superconducting gap of the electrodes. As the ratio $2\Delta/k_BT_c$ is close to the BCS value of 3.52 for low T_c cuprates such as $La_{2\text{-}x}Sr_xCuO_4$ [247], inserting $\Delta = 1.6$ meV gives a value of the T_c of 9.8 K, comparable to the observed values of $T_{c'}$.

In summary, the critical current seems to be preserved over a distance of the barrier width of close to 300 nm, which is $\sim 100\xi_{ab}$, while the spectroscopic signal points to the presence of an SNS junction. Together with the increased $T_{c'}$ of the $La_{2\text{-}x}Sr_xCuO_4$ layer under the barrier, these observations all seem to point to a genuine long-range proximity effect. However, there still are some scenarios which can lead to the same observations, and hence need to be discussed in detail.

If the barrier material is even slightly porous for ions, we cannot tell whether the increased $T_{c'}$ of the barrier material is caused by a genuine long-range proximity effect. In this case, the role of the quality of AlO_x is indeed crucial to the presented picture in this work, for if the AlO_x is slightly porous to ions, some of the gating effect is

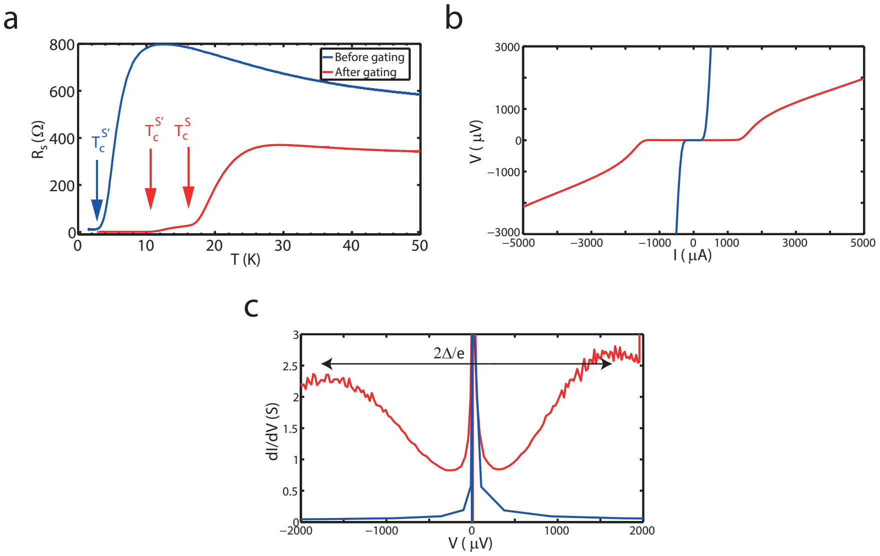

Figure 8.5: **(a)** The $R(T)$ curve measured over the 282 nm wide AlO_x barrier before gating is shown in blue, having a single T_c. After gating at -5.5 V (red curve), two transition temperatures are observed. The lower $T_{c'}$ is assumed to be that of the S' barrier, while the higher T_c is coupled to the S leads. **(b)** IV Characteristics of the junction before and after gating. Before gating, the critical current is approximately 1.2×10^2 μA. After gating, this is increased by an order of magnitude to 1.1×10^3 μA. **(c)** The numerically calculated dI/dV shows a change in behavior as well. While no structure apart from the main peak at $V = 0$ is observed before gating, after gating two additional peaks appear at ±1.6 mV.

expected to happen directly at the layer of $La_{2-x}Sr_xCuO_4$ under the barrier due to ion diffusion into the layer, which can lead to some increase in $T_{c'}$. Although the gating effect might be not as much as at the S leads, the $I(V)$ characteristics of the junction would still resemble that of the SNS or SIS junctions reported before [247].

The likelihood of this scenario depends on the deposition parameters: the oxygen pressure p and target-substrate distance d. These influence the kinetic energy of the ablated material and hence crystallinity and structure of the grown AlO_x. As stated in Ref. 166, open and porous and stoichiometric AlO_x is expected for $p^{0.5}d \geq 0.4$ $Pa^{0.5}m$, while a dense morphology but non-stoichiometric variant is grown for $p^{0.5}d \leq 0.08$ $Pa^{0.5}m$. Although the used settings in this work have been based on optimal oxygen stoichiometry, the grown material is in between both of these regimes morphologically, meaning, while most samples are non-porous, there are some samples that are indeed permeable to ions. To illustrate this, one sample is covered by a 47 nm thick layer of AlO_x on one side of a Hall-bar like channel of $La_{1.91}Sr_{0.09}CuO_4$ (Fig. 8.6a). A subsequent exposure of both areas to IL gating shows that the AlO_x covered area responds to a wide range of the gate voltage in the same way as the exposed area. We observe that, both the barrier and film area before and after gating at -5.5 V (Fig. 8.6b) can show similar T_cs, as shown in the inset.

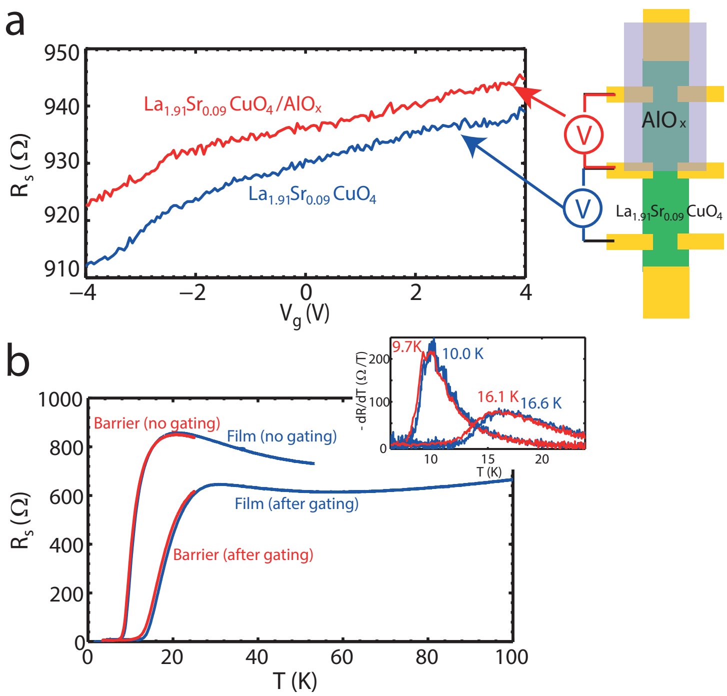

Figure 8.6: **(a)** Comparative $R(t, V_g)$ behavior of an exposed and alumina covered $La_{1.91}Sr_{0.09}CuO_4$ film in a Hall-bar configuration. **(b)** $R(T)$ characteristics of the barrier and film area before and after gating at -5.5 V. The inset shows the dR/dT as a measure of the T_c of the film and barrier areas.

It should be noted that the work presented here is preliminary, as these devices tend to breakdown at elevated voltage drops of ~5 mV between the voltage probes (~9 mA). After breakdown, the critical currents were reduced significantly, dropped to levels similar as before gating. We suspect that this might be caused by electromigration taking place either in the AlO_x barrier, or in the $La_{2\text{-}x}Sr_xCuO_4$ layer. The four-probe distance of 50 μm corresponds to an in-plane field of 1×10^4 V/cm, which is substantially lower than the required breakdown field of AlO_x of 7×10^6 V/cm [72]. The AlO_x grown in Ref. 72 is of nominal stoichiometry ($x = 1.5$), while the AlO_x grown in this work is most probably off-stoichiometry [166], which is known to have a limited breakdown voltage [81], but would still not be enough to explain the three order of magnitude of difference.

We hence suspect that a possible electromigration is more likely to happen in the cuprate layer. If we take into account that at most the top 10 UCs of the layer is conducting due to strain effects, the levels for a breakdown current of 9 mA, and 50 μm wide channel gives a current density of 1×10^6 A/cm^2. Such levels of the current densities are reported to be sufficient to induce electromigration in cuprate compounds, e.g. $YBa_2Cu_3O_{7\text{-}\delta}$ [255].

8.5 Conclusions

In conclusion, although these results are promising and we have a strong indication of a long-range proximity effect in the *ab*-axis of two orders of magnitude larger than ξ_{ab}, it is only preliminary, as we cannot exclude the AlO_x to be permeable to ions. Furthermore, the sensitivity of the system to breakdown limits the scope of this work to resistance and spectroscopic measurements, as we are lacking measurements of the IV characteristics of the junction as function of magnetic field between the initial and new T_c of the film, 4.5 K and 9.5 K, respectively. Additional data would include the dependence of the critical current as a function of the width of the AlO_x barrier. Currently, research on both of these issues is ongoing.

Chapter 9

The story continues...

As described in Chapters 7 and 8, two main methods have been used in an attempt of making an in-plane Josephson junction for the purpose of investigating the giant proximity effect (GPE). In this final chapter we introduce further experiments and combine the information from the previous chapters in order to evaluate the evidence for the in-plane giant proximity effect. We discuss the relevance of these results for various models that have been proposed, and make suggestions for further experiments.

9.1 Ionic liquid induced junction experiments revisited

The possible porosity of the barrier material of AlO$_x$ prompted us to delve into methods of overcoming this issue and to redo some of the experiments described in Chapter 8. The method used involves crosslinked poly(methyl methacrylate) (PMMA) as barrier material, which is insoluble in ethanol, acetone and the ionic liquid (IL). The present study presented here only elaborates on positive resist which becomes crosslinked at doses of $\geq$13000 μC/cm^2, an Atomic Force Microscopy (AFM) image of which can be seen in Fig. 9.1a. The backscatter effect is substantial because of long retention times of the electron beam at a certain spot during writing, resulting in wide ($\geq$80 nm) and thick barriers ($\geq$30 nm) (see Fig. 9.1b). In this specific case, the length is $\sim$5 μm, while the width is 327 nm, which is comparable to the length and width of the AlO$_x$ barrier described in Chapter 8.

The La$_{2\text{-}x}$Sr$_x$CuO$_4$ film has a doping of x = 0.09, 6 unit cells (UC) thick and is grown on top of a metallic buffer layer of 1 UC and doping of x = 0.30. Before IL gating, both the film without and with the barrier have similar electrical transport properties and critical temperature (T_c) of approximately 35.3 K (midpoint) (see Fig. 9.1c). After IL gating at $V_g = -5.5$ V for apprx. 1 hour, an increase in T_c of the film without barrier is observed, with the new value being 37.8 K. This is similar to the new T_c of the film with barrier, except that another transition temperature is present as well (see Fig. 9.1c). When the resistance related to the second T_c is inflated by a factor of 95±8, the exact, initial $R(T)$ curve is recovered, indicating that there is no T_c change of the barrier material (see Fig. 9.1d). Furthermore, this ratio would coincide with an effective barrier width of 336±28 nm, within the values suggested by AFM data.

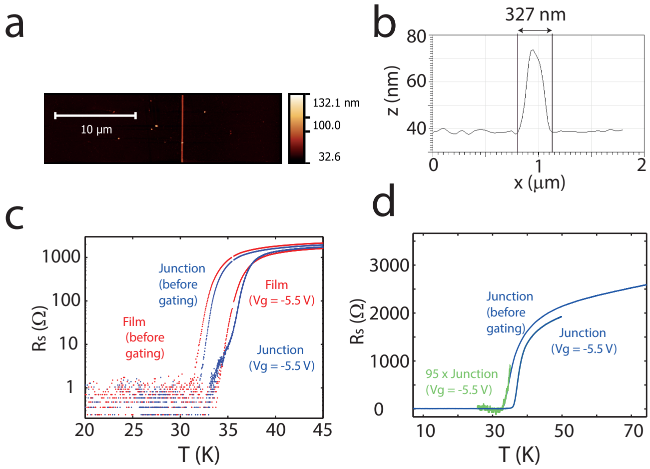

Figure 9.1: **(a)** An AFM image of the film covered with a line of crosslinked PMMA, before the application of IL. **(b)** The cross section of the barrier, having a thickness of apprx. 30 nm and width of 327 nm. **(c)** $R_s(T)$ of the film with ('Junction', blue) and without ('Film', red) barrier before and after IL gating at -5.5 V for apprx. 1 hour. Only when the resistance is measured across the film do we observe an extra transitional temperature. In **(d)**, the resistance related to this transitional temperature is inflated 95× (green) and compared to the resistance of the film with barrier before and after IL gating (blue).

Overall, the data shows that it is possible to successfully make IL gating experiments by means of barriers with crosslinked PMMA without encountering the problems of AlO$_x$. Still, the unchanged T_c of the barrier material is not supportive of a proximity effect between the leads, at least for the T_c and the barrier widths described in the present study. This is unexpected, as the barrier width is within the ab-axis GPE range reported previously.

The first explanation is, as described in Chapter 1, is the one based on the phase-disordered superconductors model proposed by Marchand *et al.* [35], which proposes that the proximity of the bulk superconductor prevents the unbinding of the vortex-antivortex pairs at the nominal barrier $T_{c'}$. This leads to a logarithmic dependence of the barrier T_c on the barrier width d and hence a significant enhancement of the supercurrent at temperatures above the initial nominal barrier $T_{c'}$,

$$T^{eff} \cong T_c \left[1 - \left(1 - \frac{T_{c'}}{T_c} \right) \frac{ln(d/\xi)}{ln(L/\xi)} \right]. \tag{9.1}$$

Here, d, ξ and L stand for the barrier width, the coherence length and length of the superconducting leads, respectively. T_c and $T_{c'}$ represent the critical temperature of the S and S' layers, respectively. Using the experimentally obtained parameters for the fitting ($d = 300$ nm; $L = 5000$ nm; $T_c = 37.8$ K; $T_{c'} = 35.3$ K and $\xi = 3.2$ nm) results in the expected barrier critical temperature as a function of the critical temperature of the leads (see Fig. 9.2).

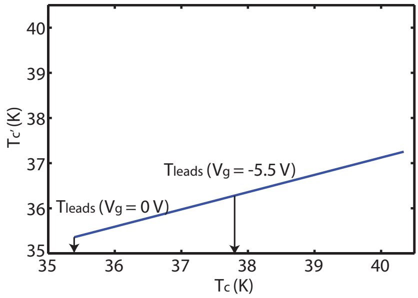

Figure 9.2: $T_{c'}$ as a function of the lead T_c of the junction shown in Fig. 9.1 according to relationship found in Marchand *et al.* [35].

The expected value for T_{eff} is 36.3 K, however the empirical value found after gating is still 35.3 K. Although the experiment requires extension to other T_c and $T_{c'}$ values and other barrier widths, the tentative conclusion is that the proximity effect does not extend as far as predicted by the model of Marchand *et al.*

9.2 Etched bilayers

The first method involved an ion etched quasi-*ab* junctions in bilayers of $La_{2\text{-}x}Sr_xCuO_4/YBa_2Cu_3O_{7\text{-}\delta}$. This method proved to be successful in achieving a genuine T_c change of the barrier material over distances of $\sim$ 50 nm, coupled with a robust I_c (using a 1 μV criterion) above its former critical temperature, $T_1 = 4.5$ K (see Fig. 9.3a).

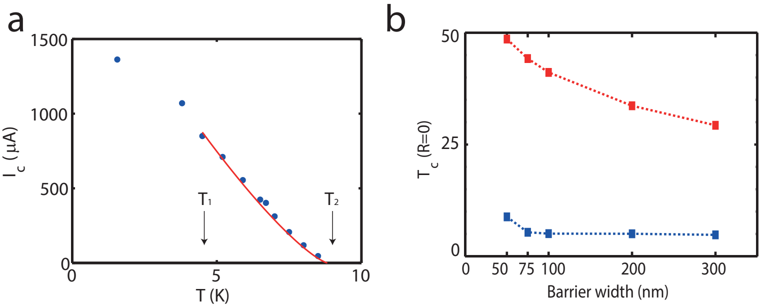

Figure 9.3: **(a)** $I_c(T)$ of the etched bilayer for a barrier width of 50 nm. At low T, the curve is characterized by a slow decrease, after which a nearly linear regime sets in. Only at temperatures close to T_c does the I_c curve upward, which allows fitting the percolation based relationship $I_c \propto \left(\frac{T}{T_c} - 1\right)^p$. The fitted curve starts from the default T_c of $La_{1.91}Sr_{0.09}CuO_4$, $T_1 = 4.5$ K until $T_2 = 8.6$ K. **(b)** $T_c(R = 0)$ values plotted as a function of barrier widths used in the etched bilayers (blue), compared with Marchand′s relationship for the expected effective barrier T_c (red).

The data presented is also compared with Marchand′*s* picture of (un)binding vortices in the pseudogap phase. Using $T_{c'} = 4.5$ K; $T_c = 78.2$ K; $L = 3$ μm and $\xi = 3.2$ nm, the values for the barrier $T_{eff}(d)$ are calculated and compared with the experimental data (see Fig. 9.3b). As a note, caution is required as the barrier is not entirely along the *ab*-axis, but is rather quasi-ab in nature. Still, the expression is only logarithmically dependent on our parameters for L, d and ξ, and the resulting dependence does not fit the experimental $T_{eff}(d)$. Hence, we have to conclude that the data presented here for the etched bilayers, in accordance with the data for the IL-gated junctions, are not in line with the vortex (un)binding theory of Marchand *et al.* [35].

Explanations invoking the divergence of coherence length expected based on the de Gennes formalism, as has been applied in the Pb/Si(111) system [21], are not satisfactory as well. Firstly, the formalism predicts that the coherence length should diverge when $T_{c'}$ is approached from above, either as $\sim 1/\sqrt{T - T_{c'}}$ (dirty limit), or as $\sim 1/(T - T_{c'})$ (clean limit). The mean free path in the S' material in our case along the *ab*-axis is estimated to be 1-2 nm, which is close to the coherence length of about 3 nm along the same direction. In either limiting cases applicable, the highest and lowest T_c of the junction, 8.6 K and 4.5 K, respectively, used to obtain $\xi = 1.4\xi_0$ or $2.0\xi_0$, which are only small corrections compared to the width of the junction.

Instead, we see a power law behavior which is in line with the theory developed by Kresin *et al.* [36] of percolation-driven connection of superconducting islands, in line with the picture of preformed pairs in the pseudogap phase (see Chapter 1). In Fig. 9.3a this is illustrated by fitting the data between $T_1 \leq T \leq T_2$ with $I_c \propto \left(\frac{T}{T_c} - 1\right)^p$, which results in power law exponent of $p = 1.29 \pm 0.15$, in agreement with the value 4/3 for the critical index known in the percolation theory, which itself is in agreement with experimental work on the GPE in $La_{2\text{-}x}Sr_xCuO_4/La_2CuO_4/La_{2\text{-}x}Sr_xCuO_4$ *c*-axis junctions by Bozovic *et al.* [36]. However, microshorts cannot be excluded in this work, especially because of the inhomogeneities involved in etching.

9.3 Conclusions and experimental outlook

To conclude, the data presented in this thesis concerning the etched bilayers and the IL-induced junctions does not support the theory based on vortex-antivortex (un)binding in the pseudogap phase as stated in Ref.35 (see Table 9.1). The de Gennes formalism has found no backing in our experiments, while we have found that the long-range proximity effect observed in the etched bilayers do support percolative transport of the supercurrent via superconducting puddles. This is quite interesting, as this can be connected to the pseudogap picture as a whole, and specifically that of phase fluctuations in accordance with Kresin′s theory [36].

Explanation	Ionic liquid induced junctions	Etched bilayers
Phase-disordered superconductor [35]	No	No
de Gennes formalism [21]	-	No
Superconducting puddles [36, 37]	-	Likely

Table 9.1: List of explanations coupled to the observations of the IL-induced junction and etched bilayer experiments.

Experimentally, there is some space for a more thorough look at the possible role of phase fluctuations in the long-range effect, where the most accute need is the investigation of the $I(V)$ characteristic of the junction firstly for various barrier widths, and secondly for a wider range of T_c of the leads. For the latter dependence, IL gating is an ideal method because of the flexibility in applying various gate voltages. Overall, the proposition would involve barriers widths (see Fig. 9.4), ideally covering at least length scales varying two orders of magnitude or more, starting from $\sim$ 10 nm. The current method of crosslinking PMMA, giving a minimum attainable width of $\sim$80 nm due to backscatter effects. Therefore, usage of negative e-beam resist such as the AR-N 7520, which crosslinks at a much lower dosage of 30 μC/cm^2 at an acceleration voltage of 30 kV, is advised. The minimized the backscattering effect ensures an attainable width is 6 nm with an aspect ratio of 10.

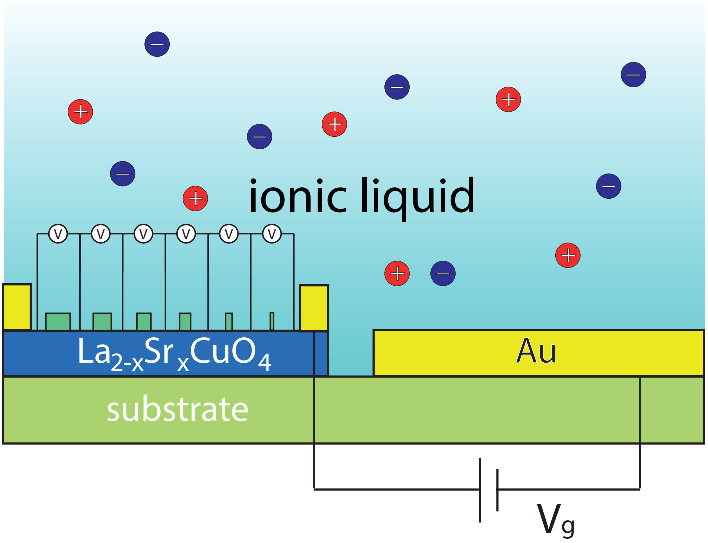

Figure 9.4: A proposed experimental setup for a further investigation of the GPE. The main aim of such an experiment is the barrier width dependence and the lead T_c dependence of the long-range effect for possible reinterpretation of the pseudogap phase. The barrier widths are varied two orders of magnitude using negative e-beam resist, starting from $\sim$ 10 nm, while the IL is used for control of the lead T_c.

9.4 The elusive Type-II Bose-Mott insulator

The long-range proximity effect reported here in the etched bilayers could fulfill the conditions required by Beekman *et al.* [42] for the observation of quantized current filaments. The model starts from a Bose-Mott insulator in its insulating phase (which may be represented by $La_{2\text{-}x}Sr_xCuO_4$ in its pseudogap phase) and is sandwiched between superconducting leads ($YBa_2Cu_3O_{7\text{-}\delta}$). The barrier should be in its Bose-Mott insulating state, and current biases smaller than the current quantum I_0 $\sim$1 mA (see Section 1.3.2) should not lead to any conduction [42]. This, however, is not observed. Although our observations do not give any evidence, this does not exclude the existence of the Type-II Bose-Mott insulator. A more dedicated experiment could involve current biasing the candidate for the Type-II Bose-Mott insulator using a parallel circuit which would have a shunt resistor (see Fig. 9.5).

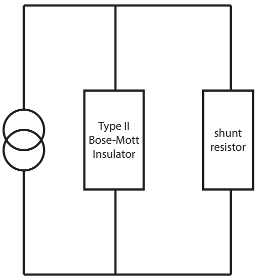

Figure 9.5: A schematic representation of an experiment which involves current biasing the idealized type-II Bose-Mott insulator in parallel with a shunt resistor.

The function of this would be that of a vacuum by-pass for the current: in case the Type-II Bose-Mott insulator has not produced its first current quantum, the resistance of the Bose-Mott insulator theoretically is infinite, and the current can still flow through the shunt resistor. Continuously increasing the current until I_0 is reached would suggest that the first Mott vortex should nucleate at the Type-II Bose-Mott insulator and the voltage drop across the Bose-Mott insulator should become zero. In principle, this process is repeatable until the 2^{nd}, 3^{rd}, n^{th} Mott vortex is formed, and in terms of an V vs. I characteristic, a sawtooth-like pattern should be observable.

This method of a vacuum by-pass for the current can be used in other systems which show interesting interplays between the electrical current and magnetism. A prominent system for this was found recently in the Mott-insulator Ca_2RuO_4 [256], for which strong diamagnetism is reported induced by a dc electrical current. The material is characterized by high resistivity at low temperatures, comparable to the situation when the Type-II Bose-Mott insulator has not yet formed the first Mott vortex. Furthermore, the ruthanate is ill characterized in this highly resistive regime, and by using the vacuum by-pass method, the unexplored regions of this interesting material can be explored, quite possibly making some connections with the present theory of the Type-II Bose-Mott insulator.

Bibliography

[1] H. K. Onnes, Comm. Phys. Lab. Univ. Leiden (1911).

[2] A. J. Moulson and J. M. Herbert, *Electroceramics: Materials, Properties, Applications* (John Wiley Sons, Chichester, 2003).

[3] G. I. Oya and E. J. Saur, Journal of Low Temperature Physics **34**, 569 (1979).

[4] C. W. Chu, L. Gao, F. Chen, Z. J. Huang, R. L. Meng, and Y. Y. Xue, Nature **365**, 6444 (1993).

[5] I. Bozovic, J. N. Eckstein, G. F. Virshup, A. Chaiken, M. Wall, R. Howell, and M. Fluss, Journal of Superconductivity **7**, 187 (1994).

[6] I. Bozovic, G. Logvenov, M. A. J. Verhoeven, P. Caputo, E. Goldobin, and M. R. Beasley, Phys. Rev. Letters **93**, 157002 (2004).

[7] E. Morenzoni, B. M. Wojek, A. Suter, T. Prokscha, G. Logvenov, and I. Bozovic, Nat. Comm. **2**, 272 (2011).

[8] K. Ueno, S. Nakamura, H. Shimotani, H. T. Yuan, N. Kimura, T. Nojima, H. Aoki, Y. Iwasa, and M. Kawasaki, Nature Nanotechnology **6**, 408 (2011).

[9] Y. Saito, Y. Kasahar, J. Ye, Y. Iwasa, and T. Nojima, Science **350**, 409 (2015).

[10] A. T. Bollinger, G. Dubuis, J. Yoon, D. Pavuna, J. Misewich, and I. Bozovič, Nature **472**, 458 (2011).

[11] M. Nakano, K. Shibuya, D. Okuyama, T. Hatano, S. Ono, M. Kawasaki, Y. Iwasa, and Y. Tokura, Nature **487**, 459 (2012).

[12] P. G. de Gennes, Rev. Mod. Phys. **36**, 225 (1964).

[13] Y. Tarutani, T. Fukazawa, U. Kabasawa, A. Tsukamoto, M. Hiratani, and K. Takagi, Appl. Phys. Lett. **58**, 2707 (1991).

[14] U. Kabasawa, Y. Tarutani, T. Fukazawa, A. Tsukamoto, M. Hiratani, and K. Takagi, Jpn. J. Appl. Phys. **30**, 1670 (1991).

[15] A. Y. Kasumov, O. V. Kononenko, V. N. Matveev, T. B. Borsenko, V. A. Tulin, E. E. Vdovin, and I. I. Khodos, Phys. Rev. Lett. **77**, 3029 (1996).

[16] R. S. Decca, H. D. Drew, E. Osquiguil, B. Maiorov, and J. Guimpel, Phys. Rev. Lett. **85**, 3708 (2000).

[17] A. Sharafiev, M. Malnou, C. Feuillet-Palma, C. Ulysse, P. Febvre, J. Lesueur, and N. Bergeal, arXiv:1701.02320v1 (2017).

[18] S. Charpentier, G. Roberge, S. Godin-Proulx, , and P. Fournier, Appl. Phys. Lett. **99**, 032511 (2011).

[19] M. Hoek, *At the interface between electron and hole-doped cuprates*, Ph.D. thesis, University of Twente (2014).

[20] T. Kirzhner and G. Koren, Scientific Reports **4**, 6244 (2014).

[21] V. Cherkez, J. Cuevas, C. Brun, T. Cren, G. Ménard, F. Debontridder, V. Stolyarov, and D. Roditchev, Phys. Rev. X **4**, 011033 (2014).

[22] L. Merchant, J. Ostrick, R. P. Barber, and R. C. Dynes, Phys. Rev. B **63**, 134508 (2001).

[23] O. Yuli, I. Asulin, L. Iomin, G. Koren, O. Millo, and D. Orgad, Phys. Rev. Lett. **101**, 057005 (2008).

[24] A. S. Alexandrov, Phys. Rev. B **75**, 132501 (2007).

[25] P. Kotetes and G. Varelogiannis, Phys. Rev. B **78**, 220509 (2008).

[26] J. Quintanilla, K. Capelle, and L. N. Oliveira, Phys. Rev. Letters **90**, 089703 (2003).

[27] G. Deutscher and P. de Gennes, *Superconductivity* (Dekker, New York, 1969).

[28] O. Fischer, M. Kugler, I. Maggio-Aprile, C. Berthod, and C. Renner, Rev. Mod. Phys. **79**, 353 (2007).

[29] J. Shi, S. D. Ha, Y. Zhiu, F. Schoofs, and S. Ramanathan, Nat. Comm. **4**, 2676 (2013).

[30] S. Blanco-Canosa, A. Frano, T. Loew, Y. Lu, J. Porras, G. Ghiringhelli, M. Minola, C. Mazzoli, L. Braicovich, E. Schierle, E. Weschke, M. L. Tacon, and B. Keimer, Phys. Rev. Lett. **110**, 187001 (2013).

[31] Y. Wang, L. Li, and N. P. Ong, Phys. Rev. B **73**, 024510 (2006).

[32] J. E. Hoffman, Physics **3**, 23 (2010).

[33] S. A. Kivelson and E. Fradkin, *Handbook of High Temperature Superconductivity* (Springer, Berlin, 2007).

[34] E. Berg, D. Orgad, and S. A. Kivelson, Phys. Rev. B **78**, 094509 (2008).

[35] D. Marchand, L. Covaci, M. Berciu, and M. Franz, Phys. Rev. Lett. **101**, 097004 (2008).

[36] V. Kresin, Y. Ovchinnikov, and S. Wolf, Appl. Phys. Lett. **83**, 722 (2003).

[37] G. Alvarez, M. Mayr, A. Moreo, and E. Dagotto, Phys. Rev. B **71**, 014514 (2005).

[38] K. McElroy, J. Lee, J. A. Slezak, D.-H. Lee, H. Eisaki, S. Uchida, and J. C. Davis, Science **309**, 1048 (2005).

[39] L. Covaci and F. Marsiglio, Phys. Rev. B **73**, 014503 (2006).

[40] N. F. Mott, Proc. Phys. Soc. A **62**, 416 (1949).

[41] M. Imada, A. Fujimori, and Y. Tokura, Rev. Mod. Phys. **70**, 1039 (1998).

[42] A. J. Beekman and J. Zaanen, Phys. Rev. B **86**, 125129 (2012).

[43] J. Bonca, P. Prelovsek, A. Ramsak, and S. Sarkar, *Open problems in strongly correlated electron systems* (Kluwer Academic Publishers, New Jersey, 2001).

[44] H. Liu, Y. Liu, and J. Li, Phys. Chem. Chem. Phys. **12**, 1685 (2010).

[45] R. Hayes, G. G. Warr, and R. Atkin, Chem. Rev. **115**, 6357 (2015).

[46] Y. V. Pershin and D. Ventra, Adv. Phys. **60**, 145 (2011).

[47] R. L. McCreery and A. J. Bergren, Adv. Mat. **21**, 4303 (2009).

[48] Z. Yang, C. Ko, and S. Ramanathan, Ann. Rev. Mater. Res. **41**, 337 (2011).

[49] K. Ueno, H. Shimotani, Y. Iwasa, and M. Kawasaki, Applied Physics Letters **96**, 252107 (2010).

[50] H. Yuan, H. Shimotani, A. Tsukazaki, A. Ohtomo, M. Kawasaki, and Y. Iwasa, J. Am. Chem. Soc. **132**, 6672 (2010).

[51] S. Shimizu, R. Yoshimi, T. Hatano, K. S. Takahashi, A. Tsukazaki, M. Kawasaki, Y. Iwasa, and Y. Tokura, Phys. Rev. B. **86**, 045319 (2012).

[52] J. T. Ye, Y. J. Zhang, R. Akashi, M. S. Bahramy, R. Arita, and Y. Iwasa, Science **338**, 1193 (2012).

[53] H. Yuan, M. S. Bahramy, K. Morimoto, S. Wu, K. Nomura, B.-J. Yang, H. Shimotani, R. Suzuki, M. Toh, C. Kloc, X. Xu, R. Arita, N. Nagaosa, and Y. Iwasa, Nature Physics **9**, 563 (2013).

[54] D. Constanzo, S. Jo, H. Berger, and A. F. Morpurgo, Nature Nanotechnology **11**, 339 (2016).

[55] J. T. Ye, S. Inoue, K. Kobayashi, Y. Kasahara, H. T. Yuan, H. Shimotani, and Y. Iwasa, Nature Mater. **9**, 125 (2010).

[56] S. Asanuma, X. P.-H, H. Yamada, H. Sato, I. H. Inoue, H. Akoh, A. Sawa, K. Ueno, H. Shimotani, H. Yuan, M. Kawasaki, and Y. Iwasa, Appl. Phys. Lett. **97**, 142110 (2010).

[57] C. Ge, K.-J. Jin, L. Gu, L.-C. Peng, Y.-S. Hu, H.-Z. Guo, H.-F. Shi, J.-K. Li, J.-O. Wang, X.-X. Guo, C. Wang, M. He, H.-B. Lu, and G.-Z. Yang, Adv. Mat. Interfaces **2**, 1500407 (2015).

[58] A. Herklotz, E.-J. Guo, A. T. Wong, T. L. Meyer, S. Dai, T. Z. Ward, H. N. Lee, and M. R. Fitzsimmons, Nano Lett. **17**, 1665 (2017).

[59] X. Leng, J. Garcia-Barriocanal, S. Bose, Y. Lee, and A. M. Goldman, Physical Review Letters **107**, 027001 (2011).

[60] J. Garcia-Barriocanal, A. Kobrinskii, X. Leng, J. Kinney, B. Yang, S. Snyder, and A. M. Goldman, Physical Review B **87**, 024509 (2013).

[61] J. Garcia-Barriocanal, A. Kobrinskii, X. Leng, J. Kinney, B. Yang, S. Snyder, and A. M. Goldman, Physical Review B **87**, 024509 (2013).

[62] A. Fete, L. Rossi, A. Augieri, and C. Senatore, Appl. Phys. Lett. **109**, 192601 (2016).

[63] A. M. Perez-Muoz, P. Schio, R. Poloni, A. Fernandez-Martinez, A. Rivera-Calzada, J. C. Cezar, E. Salas-Colera, G. R. Castro, J. Kinney, C. Leon, J. Santamaria, J. Garcia-Barriocana, and A. M. Goldman, PNAS **114**, 215 (2017).

[64] G. Dubuis, Y. Yacoby, H. Zhou, X. He, A. T. Bollinger, D. Pavuna, R. Pindak, and I. Bozovič, Sci. Rep. **6**, 32378 (2016).

[65] K. Jin, W. Hu, B. Zhu, D. Kim, J. Yuan, Y. Sun, T. Xiang, M. S. Fuhrer, I. Takeuchi, and R. L. Greene, Scientific Reports **6**, 26642 (2016).

[66] S. W. Zeng, Z. Huang, W. M. Lv, N. N. Bao, K. Gopinadhan, L. K. Jian, T. S. Herng, Z. Q. Liu, Y. L. Zhao, C. J. Li, H. J. H. Ma, P. Yang, J. Ding, T. Venkatesan, and Ariando, Physical Review B **92**, 020503 (2015).

[67] J. Jeong, N. Aetukuri, T. Graf, T. D. Schladt, M. G. Samant, and S. S. P. Parkin, Science **339**, 1402 (2013).

[68] Y. Zhou and S. Ramanathan, J. of Applied Physics **111**, 084508 (2012).

[69] H. Ji, J. Wei, and D. Natelson, Nano Letters **12**, 2988 (2012).

[70] M. Li, W. Han, J. Jeong, M. G. Samant, and S. S. P. Parkin, Nano Letters **13**, 4675 (2013).

[71] P. Gallagher, M. Lee, T. A. Petach, S. W. Stanwyck, J. R. Williams, K. Watanabe, T. Taniguchi, and D. Goldhaber-Gordon, Nature Communications **6**, 1 (2015).

[72] P. Gallagher, M. Lee, J. R. Williams, and D. Goldhaber-Gordon, Nature Physics **10**, 748 (2014).

[73] Y. Lee, C. Clement, J. Hellerstedt, J. Kinney, L. Kinnischtzke, X. Leng, S. D. Snyder, and A. M. Goldman, Physical Review Letters **106**, 136809 (2011).

[74] P. Walden, Bull. Acad. Imper. Sci. (St. Petersburg) **8**, 405 (1914).

[75] J. D. Holbrey and K. R. Seddon, Clean. Prod. Processes **1**, 223 (1999).

[76] L. Crowhurst, P. R. Mawdsley, J. M. Perez-Arlandis, P. A. Salter, and T. Welton, Phys. Chem. Chem. Phys. **5**, 2790 (2003).

[77] E. W. Castner, C. Margulis, M. Maroncelli, and J. F. Wishart, Annual Review of Physical Chemistry **62**, 85 (2011).

[78] H. Helmholtz, Annalen der Physik und Chemie **89**, 211 (1853).

[79] S. Z. Bisri, Adv. Mat. **29**, 1607054 (2017).

[80] T. Fujimoto and K. Awaga, Phys. Chem. Chem. Phys. **15**, 8983 (2013).

[81] M. Huijben, *Interface Engineering for Oxide Electronics*, Ph.D. thesis, University of Twente (2006).

[82] M. Suzuki and M. Hikita, Phys. Rev. B **44**, 249 (1991).

[83] P. Konsin and B. Sorkin, Phys. Rev. B **58**, 5795 (1998).

[84] F. Wang, P. Stepanov, M. Gray, C. N. Lau, M. E. Itkis, and R. C. Haddon, ACS Nano **15**, 5284 (2012).

[85] L. Fruchter, V. Brouet, D. Colson, J.-B. Moussy, A. Forget, and Z. Z. Li, arXiv:1703.05978v2 (2017).

[86] A. Baldelli, Acc. Chem. Res. **41**, 421 (2008).

[87] M. V. Fedorov, J. Phys. Chem. B **112**, 11868 (2008).

[88] T. A. Petach, A. Mehta, R. Marks, B. Johnson, M. F. Toney, and D. Goldhaber-Gordon, ACS Nano **10**, 4565 (2016).

[89] T. A. P. K. V. Reich, X. Zhang, K. Watanabe, T. Taniguchi, B. I. Shklovskii, and D. Goldhaber-Gordon, ACS Nano **11**, 8395 (2017).

[90] Y. Sato, K. Doi, Y. Katayama, and K. Ueno, Japanese Journal of Applied Physics **56**, 051101 (2017).

[91] G. Dezi, N. Scopigno, S. Caprara, and M. Grilli, arXiv:1706.01274v1 (2017).

[92] K. Hanzawa, H. Sato, H. Hiramatsu, T. Kamiya, and H. Hosono, IEEE Transactions on Applied Superconductivity **27**, 7500405 (2017).

[93] O. M. Yaghi, G. Li, and H. Li, Nature **378**, 703 (1995).

[94] X. Zaho, W. Jin, J. Cai, J. Ye, Z. Li, Y. Ma, J. Xie, and L. Qi, Adv. Funct. Mater. **21**, 3554 (2011).

[95] W. H. Brattain and C. G. B. Garrett, Bell Labs Technical Journal **34**, 129 (1955).

[96] X. Leng, J. Pereiro, J. Strle, G. Dubuis, A. T. Bollinger, A. Gozar, J. Wu, N. Litombe, C. Panagopoulos, D. Pavuna, and I. Božović, Quantum Materials **2**, 35 (2017).

[97] X. Meng, F. Quenneville, F. Venne, E. D. Mauro, D. Işık, M. Barbosa, Y. Drolet, M. M. Natile, D. Rochefort, F. Soavi, and C. Santo, J. Phys. Chem. C **119**, 21732 (2015).

[98] H. Yuan, H. Shimotani, J. Ye, S. Yoon, H. Aliah, A. Tsukazaki, M. Kawasaki, and Y. Iwasa, J. Am. Chem. Soc. **132**, 18402 (2010).

[99] T. D. Schladt, T. Graf, N. B. Aetukuri, M. Li, A. Fantini, X. Jiang, M. G. Samant, and S. S. P. Parking, ACS Nano **7**, 8074 (2013).

[100] N. Chandrasekhar, O. T. Valls, and A. M. Goldman, Phys. Rev. Lett. **71**, 1079 (1993).

[101] M. Lee, J. R. Williams, S. Zhang, C. D. Frisbie, and D. Goldhaber-Gordon, Phys. Rev. Lett. **107**, 256601 (2011).

[102] H. Tada, T. Nojima, S. Nakamura, H. Shimotani, Y. Iwasa, and N. Kobayashi, Journal of Physics: Conference Series **150**, 10.1088/1742 (2009).

[103] S. D. Ha, U. Vetter, J. Shi, and S. Ramanathan, Appl. Phys. Lett. **102**, 183102 (2013).

[104] A. M. G. S. Bubel, A. J. Hauser, S. S. T. E. Mates, and M. L. Chabinyc, Appl. Phys. Lett. **106**, 122102 (2015).

[105] Y. Dong, H. Xu, Z. Luo, H. Zhou, D. D. Fong, W. Wu, and C. Gao, APL Materials **5**, 051101 (2017).

[106] J. Shi, S. D. Ha, Y. Zhou, F. Schoofs, and S. Ramanathan, Nature Communications **472**, 458 (2013).

[107] R. Scherwitzl, P. Zubko, G. Lezama, and S. Ono, Adv. Mat. **22**, 5517 (2010).

[108] A. C. Lang, J. D. Sloppy, H. Ghassemi, R. C. Devlin, R. J. Sichel-Tissot, J.-C. Idrobo, S. J. May, and M. L. Taheri, ACS Appl. Mat. and Inter. **6**, 17018 (2014).

[109] H. Yuan, H. Shimotani, A. Tsukazaki, A. Ohtomo, M. Kawasaki, and Y. Iwasa, Advanced Functional Materials **19**, 1046 (2009).

[110] S. Mickevičius, S. Grebinskij, V. Bondarenka, H. Tvardauskas, M. Senulis, V. Lisauskas, K. Šliužienė, B. Vengalis, and B. A. Orlowski, Radiat. Phys. Chem. **78**, S29 (2009).

[111] S. Thiemann, S. Sachnov., S. Porscha, P. Wasserscheid, and J. Zaumseil, Journ. Phys. Chem. C **116**, 13536 (2012).

[112] K. Ueno, T. Nojima, S. Yonezawa, M. Kawasaki, Y. Iwasa, and Y. Maeno, Phys. Rev. B **89**, 020508(R) (2014).

[113] X. Leng, A. T. Bollinger, and I. Božović, Sci. Rep. **6**, 31239 (2016).

[114] Y. Yamada, K. Ueno, T. Fukumura, H. T. Yuan, H. Shimotani, Y. Iwasa, L. Gu, S. Tsukimoto, Y. Ikuhara, and M. Kawasaki, Science **332**, 1065 (2011).

[115] M. Nakano, D. Okuyama, K. Shibuya, M. Mizumaki, H. Ohsumi, M. Yoshida, M. Takata, M. Kawasaki, Y. Tokura, T. Arima, and Y. Iwasa, Adv. Electron. Mater. **1**, 1500093 (2015).

[116] T. Ichimura, K. Fujiwara, and H. Tanaka, Sci. Rep. **4**, 5818 (2014).

[117] A. Ohtomo and H. Y. Hwang, Nature **427**, 423 (2004).

[118] C. J. Noguera, J. Phys.: Condens. Matter. **12**, R367 (2000).

[119] H. Ohno, *Electrochemical Aspects of Ionic Liquids* (John Wiley Sons, Inc., New Jersey, 2005).

[120] U. Schroder, J. D. Wadhawan, R. G. Compton, P. A. Z. Marken, F. Suarez, C. S. Consorti, R. F. de Souza, and J. Dupont, New J. Chem. **24**, 1009 (2000).

[121] A. M. O'Mahony and other, Journal of Chemical Engineering Data **53**, 2884 (2008).

[122] J. T. Ye, S. Inoue, K. Kobayashi, Y. Kasahara, H. T. Yuan, H. Shimotani, and Y. Iwasa, Nature Materials **9**, 125 (2010).

[123] H. F. Wong, S. M. Ng, W. F. Cheng, Y. Liu, X. Chen, D. von Nordheim, C. L. Mak, J. Dai, B. Ploss, and C. W. Leung, Solid-State Electronics **138**, 56 (2017).

[124] J. Lourembam, J. Wu, J. Ding, W. Lin, and T. Wu, PRB **89**, 014425 (2014).

[125] P.-H. Xiang, S. Asanuma, H. Yamada, I. H. Inoue, H. Sato, H. Akoh, A. Sawa, K. Ueno, H. Yuan, H. Shimotani, M. Kawasaki, and Y. Iwasa, Adv. Mat. **23**, 5822 (2011).

[126] T. Nakamura, A. N. Hattori, T. V. A. Nugyyen, K. Fujiwara, and H. Tanaka, Appl. Phys. Express **8**, 073201 (2015).

[127] A. S. Dhoot, C. Israel, X. Moya, N. D. Mathur, and R. H. Friend, Phys. Rev. Lett. **102**, 136402 (2009).

[128] H. Atesci, F. Coneri, M. Leeuwenhoek, F. Coneri, J. Bommer, S. G. Lemay, J. Seddon, H. Hilgenkamp, and J. M. van Ruitenbeek, arXiv:1709.01178 (2017).

[129] X. Leng, J. Garcia-Barriocanal, J. Kinney, B. Yang, Y. Lee, and A. M. Goldman, Eur. Phys. J. Special Topics **222**, 1203 (2013).

[130] T. Nojima, H. Tada, S. Nakamura, N. Kobayashi, H. Shimotani, and Y. Iwasa, Phys. Rev. B **84**, 020502 (2011).

[131] H. Atesci, F. Coneri, M. Leeuwenhoek, H. Hilgenkamp, and J. M. van Ruitenbeek, Fizika Nizkikh Temperatur **43**, 353 (2017).

[132] P.-H. Xiang, S. Asanuma, H. Yamada, H. Sato, I. H. Inoue, H. Akoh, A. Sawa, M. Kawasaki, and Y. Iwasa, Adv. Mat. **25**, 2158 (2013).

[133] P. M. Wu, Appl. Phys. Lett. **106**, 042602 (2015).

[134] S. Nishihaya, M. Uchida, Y. Kozuka, Y. Iwasa, and M. Kawasaki, ACS Appl. Mater. Interfaces **8**, 22330 (2016).

[135] R. Misra, M. McCarthy, and A. F. Hebard, Appl. Phys. Lett. **90**, 052905 (2007).

[136] H. T. Yi, B. Gao, W. Xie, S.-W. Cheong, and V. Podzorova, Sci. Rep. **4**, 6604 (2014).

[137] F. Breech and L. Cross, Appl. Spect. **16**, 59 (1962).

[138] H. Smith and A. Tuner, Appl. Opt. **4**, 147 (1965).

[139] D. Dijkkamp, T. Venkatesan, X. Wu, S. Shaheen, N. Jisrawi, Y. Min-Lee, W. McLean, and M. Croft, Appl. Phys. Lett. **51**, 619 (1987).

[140] E. Irissou, B. Le Drogoff, M. Chaker, M. Trudeau, and D. Guay, J. Mater. Res. **19**, 950 (2004).

[141] E. Irissou, B. Le Drogoff, M. Chaker, and D. Guay, Appl. Phys. Lett. **80**, 1716 (2002).

[142] N. W. Ashcroft and N. D. Mermin, *Solid State Physics* (Thomson Learning, Inc., 1976).

[143] T. Terashima, Y. Bando, K. Iijima, K. Yamamoto, K. Hirata, K. Hayashi, K. Kamigaki, and H. Terauchi, Physical Review Letters **65**, 2684 (1990).

[144] G. Rijnders, G. Koster, V. Leca, D. H. A. Blank, and H. Rogalla, Applied Surface Science **168**, 223 (2000).

[145] H. Takagi, T. Ido, S. Ishibashi, M. Uota, S. Uchida, and Y.Tokura, Phys. Rev. B **40**, 2254 (1989).

[146] J. Kinney, *Continuous Doping of* La_2CuO_{4+x} *Thin Films*, Ph.D. thesis, University of Minnesota (2015).

[147] X. Leng and I. Bozovič, J. Supercond. Nov. Magn. **28**, 71 (2015).

[148] J. P. Locquet, J. Perret, J. Fompeyrine, and E. Machler, Nature **394**, 453 (1998).

[149] L. Gao, Y. Y. Xue, F. Chen, Q. Xiong, R. L. Meng, D. Ramirez, C. W. Chu, J. H. Eggert, and H. K. Mao, Phys. Rev. B **50**, 4260 (1994).

[150] A. P. Drozdov, M. I. Eremets, I. A. Troyan, V. Ksenofontov, and S. I. Shylin, Nature **525**, 73 (2016).

[151] H. Sato and M. Naito, Physica C **274**, 221 (1997).

[152] M. Z. Cieplak, M. Berkowski, S. Guha, E. Cheng, A. S. Vagelos, D. J. Rabinowitz, B. Wu, I. E. Trofimov, and P. Lindenfeld, Appl. Phys. Lett. **65**, 3383 (1994).

[153] H. Sato, H. Yamamoto, and M. Naito, Physica C **274**, 227 (1997).

[154] I. Bozovic, G. Logvenov, I. Belca, B. Narimbetov, and I. Sveklo, Phys. Rev. Lett. **89**, 107001 (2002).

[155] T. Ohnishi, K. Takahashi, M. Nakamura, M. Kawasaki, M. Yoshimoto, and H. Koinuma, Appl. Phys. Lett. **74**, 2531 (1999).

[156] I. Bozovič, X. He, J. Wu, and A. T. Bollinger, Nature **536**, 309 (2016).

[157] A. Biswas, P. B. Rossen, J. Ravichandran, Y. H. Chu, Y. W. Lee, C.-H. Yang, R. Ramesh, and Y. H. Jeong, Appl. Phys. Lett. **102**, 051603 (2013).

[158] C. Le Paven-Thivet, M. Guilloux-Viry, J. Padiou, A. Perrin, M. Sergent, M. A. de Vauchier, and N. Bontemps, Physica C **244**, 231 (1995).

[159] A. Gozat, G. Logvenov, L. F. Kourkoutis, A. T. Bollinger, L. A. Giannuzzi, D. A. Muller, and I. Bozovic, Nature **455**, 782 (2008).

[160] B. Prijamboedi and S. Kashiwaya, J Mater Sci: Mater Electron **17**, 483 (2006).

[161] L. Luo, M. E. Hawley, C. J. Maggiore, R. C. Dye, R. E. Muenchausen, L. Chen, B. Schmidt, and A. E. Kaloyeros, Appl. Phys. Lett. **62**, 1993 (1993).

[162] B.-S. Li, A. Sawa, and H. Okamoto, Appl. Phys. Lett. **102**, 111606 (2013).

[163] Y. Xie, Y. Hikita, C. Bell, and H. Y. Hwang, Nature Communications **2**, 494 (2011).

[164] J. G. Simmons, J. Appl. Phys. **34**, 1793 (1963).

[165] H. B. Michaelson, J. of Appl. Phys. **48**, 4729 (1977).

[166] F. D. Fonzo, D. Tonini, A. L. Bassi, C. S. Casari, M. G. Beghi, C. E. Bottani, D. Gastaldi, P. Vena, and R. Contro, Appl. Phys. A **93**, 765 (2008).

[167] G. J. H. M. Rijnders, G. Koster, D. H. A. Blank, and H. Rogalla, IEEE Transactions on Applied Superconductivity **9**, 1547 (1999).

[168] T. Frey, C. C. Chi, C. C. Tsuei, T. Shaw, and F. Bozso, Physical Review B **49**, 3483 (1994).

[169] H. Yuan, H. Shimotani, A. Tsukazaki, A. Ohtomo, M. Kawasaki, and Y. Iwasa, Adv. Func. Mater. **19**, 1046 (2009).

[170] H. Shimotani, H. Asanuma, A. Tsukazaki, A. Ohtomo, M. Kawasaki, and Y. Iwasa, Appl. Phys. Lett. **91**, 082106 (2007).

[171] A. M. Goldman, Ann. Rev. Mater. Res. **44**, 45 (2014).

[172] K. Ueno, S. Nakamura, H. Shimotani, H. T. Yuan, N. Kimura, T. Nojima, H. Aoki, Y. Iwasa, and M. Kawasaki, Nature Nano. **6**, 408 (2011).

[173] X. Leng, J. Garcia-Barriocanal, S. Bose, Y. Lee, and A. M. Goldman, Phys. Rev. Lett. **107**, 027001 (2011).

[174] Y. Lee, C. Clement, J. Hellerstedt, J. Kinney, L. Kinnischtzke, X. Leng, S. D. Snyder, and A. M. Goldman, Phys. Rev. Lett. **106**, 136809 (2011).

[175] M. Nakano, K. Shibuya, D. Okuyama, T. Hatano, S. Ono, M. Kawasaki, Y. Iwasa, and Y. Tokura, Nature **487**, 459 (2012).

[176] Y.-Y. Pai, A. Tylan-Tyler, P. Irvin, and J. Levy, ChemArxiv.org (2017).

[177] K. Ueno, S. Nakamura, H. Shimotani, A. Ohtomo, N. Kimura, T. Nojima, H. Aoki, Y. Iwasa, and M. Kawasaki, Nature Mater. **7**, 855 (2008).

[178] M. Li, T. Graf, T. Schladt, X. Jiang, and S. P. Parkin, Phys. Rev. Lett. **109**, 196803 (2012).

[179] P. Gallagher, M. Lee, T. A. Petach, S. W. Stanwyck, J. R. Williams, K. Watanabe, T. Taniguchi, and D. Goldhaber-Gordon, Nature Commun. **6**, 1 (2015).

[180] T. Petach, K. Reich, X. Zhang, K. Watanabe, T. Taniguchi, B. Shklovskii, and D. Goldhaber-Gordon, ACS Nano **11**, 8395 (2017).

[181] J. Jeong, N. Aetukuri, T. Graf, T. D. Schladt, M. G. Samant, and S. S. P. Parkin, Science **339**, 1402 (2013).

[182] M. Li, W. Han, J. Jeong, M. G. Samant, and S. S. P. Parkin, Nano Lett. **13**, 4675 (2013).

[183] K. Ueno, H. Shimotani, Y. Iwasa, and M. Kawasaki, Appl. Phys. Lett. **96**, 252107 (2010).

[184] J. Garcia-Barriocanal, A. Kobrinskii, X. Leng, J. Kinney, B. Yang, S. Snyder, and A. M. Goldman, Phys. Rev. B **87**, 024509 (2013).

[185] T. Tsuchiya, M. Ochi, T. Higuchi, K. Terabe, and M. Aono, ACS Appl. Mater. Interf. **7**, 12254 (2015).

[186] E. Schmidt, S. Shi, P. Ruden, and C. Frisbie, ACS Appl. Mater. Interf. **8**, 14879 (2016).

[187] H. Li, K. Xu, B. Bourdon, H. Lu, Y.-C. Lin, J. Robinson, A. Seabaugh, and S. Fullerton-Shirey, J. Phys. Chem. C **121**, 16996 (2017).

[188] T. Sato, G. Masuda, and K. Takagi, Electrochimica Acta **49**, 3603 (2004).

[189] H. Ohno, *Electrochemical Aspects of Ionic Liquids* (John Wiley & Sons, Inc., New Jersey, 2005).

[190] H. Yuan, H. Shimotani, J. Ye, S. Yoon, H. Aliah, A. Tsukazaki, M. Kawasaki, and Y. Iwasa, J. Am. Chem. Soc. **132**, 18402 (2010).

[191] K. Hayamizu, S. Tsuzuki, S. Seki, K. Fujii, M. Suenaga, and Y. Umebayashi, J. Chem. Phys. **133**, 194505 (2010).

[192] S. Adam, S. Cho, M. S. Fuhrer, and S. Das Sarma, Phys. Rev. Lett. **101**, 046404 (2008).

[193] A. K. Sen, K. K. Bardhan, and B. K. Chakrabart, *Quantum and Semi-classical Percolation and Breakdown in Disordered Solids* (Springer, Berlin, 2009).

[194] A. J. Rimberg, T. R. Ho, and J. Clarke, Phys. Rev. Lett. **74**, 4714 (1995).

[195] M. Li, T. Graf, T. D. Schladt, X. Jian, and S. S. P. Parkin, Phys. Rev. Lett. **109**, 196803 (2012).

[196] Y. Zhou and S. Ramanathani, Appl. Phys. Lett. **111**, 084508 (2012).

[197] J. Bednorz and K. A. Müller, Z. Phys. B: Condens. Matter **64**, 189 (1986).

[198] E. Dagotto, Review of Modern Physics **66**, 763 (1994).

[199] D. J. Scalapino, Phys. Rep. **250**, 329 (1995).

[200] M. A. Kastner, R. J. Birgeneau, G. Shirane, and Y. Endoh, Rev. Mod. Phys. **70**, 897 (1998).

[201] T. Timusk and B. Statt, Rep. Prog. Phys. **62**, 61 (1999).

[202] J. Orenstein and A. J. Millis, Science **288**, 468 (2000).

[203] C. H. Ahn, A. Bhattacharya, M. D. Ventra, J. N. Eckstein, C. D. Frisbie, M. E. Gershenson, A. M. Goldman, I. H. Inoue, J. Mannhart, A. J. Millis, A. F. Morpurgo, D. Natelson, and J. M. Triscone, Review of Modern Physics **78**, 1185 (2006).

[204] D. Matthey, S. Gariglio, and J. Triscone, Applied Physics Letters **83**, 3758 (2003).

[205] M. Salluzzo, A. Cassinese, G. M. D. Luca, A. Gambardella, A. Prigiobbo, and R. Vaglio, Physical Review B **70**, 214528 (2004).

[206] A. Cassinese, G. M. D. Luca, A. Prigiobbo, M. Salluzzo, and R. Vaglio, Applied Physics Letters **84**, 3933 (2004).

[207] J. Mannhart, J. G. Bednorz, K. A. Miiller, and D. G. Schlom, Z. Phys. B **83**, 307 (1991).

[208] J. Mannhart, Supercond. Sci. Technol. **9**, 46 (1996).

[209] H. C. Lin, P. D. Ye, and G. D. Wilk, Applied Physics Letters **87**, 182904 (2005).

[210] Y. H. Wu, M. Y. Yang, and A. Chin, IEEE Electron Device Letters **21**, 341 (2000).

[211] V. C. Matijasevic, S. Bogers, N. Y. Chen, H. M. Appelboom, P. Hadley, and J. E. Mooij, Physica C **235-240**, 2097 (1994).

[212] H. Shimotani, H. Asanuma, A. Tsukazaki, A. Ohtomo, M. Kawasaki, and Y. Iwasa, Applied Physics Letters **91**, 082106 (2007).

[213] G. Dubuis, A. T. Bollinger, D. Pavuna, J. Misewich, and I. Bozovič, Journal of Applied Physics **111**, 112632 (2012).

[214] L. Zhang, S. W. Zeng, D. Y. Wan, K. Han, L. K. Jian, A. Ariando, and T. Venkatesan, (2016), aPS March Meeting, http://meetings.aps.org/link/BAPS.2016.MAR.V25.11.

[215] A. Rüfenacht, P. Chappatte, S. Gariglio, Leemann, J. Fompeyrine, J.-P. Locquet, and Martinoli, Solid-State Electron **47**, 2167 (2003).

[216] Y. Jaccard, A. Cretton, E. J. Williams, J.-P. Locquet, E. Mächler, C. Gerber, T. Schneider, O. Fischer, and P. Martinoli, Proc. SPIE **2158**, 200 (1994).

[217] E. O. Polat, O. Balcı, and O. Kocabas, Sci. Rep. **4** (2014), 10.1038/srep06484.

[218] G. Dubuis, A. T. Bollinger, D. Pavuna, and I. Bozovič, J. of Applied Physics **111**, 112632 (2012).

[219] T. Sato, G. Masuda, and K. Takagi, Electrochimica Acta **49**, 3603 (2004).

[220] J. F. Rusling and S. L. Suib, Adv. Mat. **6**, 922 (1994).

[221] P. T. Kissinger and W. R. Heineman, J. Chem. Education **60**, 702 (1983).

[222] T. Tsuchiya, M. Ochi, T. Higuchi, K. Terabe, and M. Aono, ACS Appl. Mater. Interfaces **7**, 12254 (2015).

[223] K. Hayamizu, S. Tsukuzi, S. Seki, Y. Ohno, H. Miyashiro, and Y. Kobayashi, J. Phys. Chem. B **112**, 1189 (2008).

[224] K. Hayamizu, S. Tsukuzi, and S. Seki, J. Chem. Eng. Data **59**, 1944 (2014).

[225] T. Katase, K. Endo, T. Tohei, Y. Ikuhara, and H. Ohta, Adv. Electron. Mater. **1**, 1500063 (2015).

[226] K. Kobayashi, Y. Goto, S. Matsushima, and G. Okada, J. Mat. Sci. Letters **10**, 523 (1991).

[227] W. Jian, S. N. Mao, X. X. Xi, X. Jian, J. L. Peng, T. Venkatesan, C. J. Lobb, and R. L. Greene, Physical Review Letters **73**, 1291 (1994).

[228] Y. Saito and Y. Iwasa, ACS Nano **9**, 3192 (2015).

[229] K. Ueno, S. Nakamura, H. Shimotani, A. Ohtomo, N. Kimura, T. Nojima, H. Aoki, Y. Iwasa, and M. Kawasaki, Nature Materials **7**, 855 (2008).

[230] B.-S. Li, A. Sawa, and H. Okamoto, Appl. Phys. Lett. **102**, 111606 (2013).

[231] H. Atesci, F. Coneri, M. Leeuwenhoek, J. Bommer, S. G. Lemay, J. R. T. Seddon, H. Hilgenkamp, and J. M. Van Ruitenbeek, e-print arXiv:1709.01178 (2017).

[232] C. Y. Chen, R. J. Birgeneau, M. A. Kastner, N. W. Preyer, and T. Thio, Phys. Rev. B **43**, 392 (1991).

[233] K. Hanzawa, H. S. and. H. Hiramatsu, T. Kamiya, and H. Hosono, IEEE Transactions on Applied Superconductivity **27**, 7500405 (2017).

[234] T. Jänsch, J. Wallauer, and B. Roling, J. Phys. Chem. C **119**, 4620 (2015).

[235] R. Atkin, N. Borisenko, M. Drüschler, S. Z. E. Abedin, F. Endres, R. Hayes, B. Huber, and B. Roling, Phys. Chem. Chem. Phys. **13**, 6849 (2011).

[236] N. Chandrasekhar, O. T. Valls, and A. M. Goldman, Phys. Rev. Lett. **71**, 1079 (1993).

[237] F. Arrouy, J.-P. Locquet, E. J. Williams, E. Mächler, J.-C. G. R. Berger C. Gerber, C. Monroux, and A. Wattiaux, Phys. Rev. B **54**, 7512 (1996).

[238] J.-P. Locquet, F. Arrouy, E. Mächler, M. Despont, P. Bauer, and E. J. Williams, Appl. Phys. Lett **14**, 1999 (1999).

[239] T. Ekino, K. Matsukuma, T. Takabatake, and H. Fujii, Physica B **165-166**, 1529 (1990).

[240] V. J. Emery and S. A. Kivelson, Nature **374**, 434 (1995).

[241] W. S. Lee, I. M. Vishik, K. Tanaka, D. H. Lu, T. Sasagawa, N. Nagaosa, T. P. Devereaux, Z. Hussain, and Z.-X. Shen, Nature **450**, 81 (2007).

[242] V. Kresin, Y. Ovchinnikov, and S. Wolf, Physics Reports **431**, 231 (2006).

[243] K.-U. Barholz, M. Y. Kupriyanov, U. Hübner, F. Schmidl, and P. Seidel, Physica C: Superconductivity **334**, 175 (2000).

[244] K. A. Delin and A. W. Kleinsasser, Supercond. Sci. Technol. **9**, 227 (1996).

[245] P. Chaudhari, J. Mannhart, D. Dimos, C. C. Tsuei, J. Chi, M. M. Oprysko, and M. Scheuermann, Phys. Rev. Lett. **60**, 1653 (1988).

[246] J. Gao, W. A. M. Aarnink, G. J. Gerritsma, and H. Rogalla, Physica C **171**, 126 (1990).

[247] S. A. Cybart, E. Y. Cho, T. J. Wong, B. H. Wehlin, M. K. Ma, C. Huynh, and R. C. Dynes, Nature Nanotechnology **10**, 598 (2015).

[248] S. A. Cybart, S. M. Anton, S. M. Wu, and J. C. R. C. Dynes, Nano Letters **9**, 3581 (2009).

[249] I. A. Chaban, Physics of the Solid State **50**, 803 (2008).

[250] M. Tinkham, *Introduction to Superconductivity 2nd edn* (Dover Publications, Mineola, New York, 1996).

[251] V. J. Emery and S. A. Kivelson, Nature **374**, 434 (1995).

[252] G. Deutscher, Nature **397**, 410412 (1990).

[253] Y. Takahashi, Y. Hashimoto, Y. Iye, and S. Katsumoto, Journal of Crystal Growth **378**, 400 (2013).

[254] A. Shailos, W. Nativel, A. Kasumov, C. Collet, M. Ferrier, S. Gueron, R. Deblock, and H. Bouchiat, Europhysics Letters **79**, 57008 (2007).

[255] J. P. Sydow, D. Chamberlain, R. A. Buhrman, K. Char, and B. H. Moeckly, Applied Superconductivity **6**, 511 (1998).

[256] C. Sow, S. Yonezawa, S. Kitamura, T. Oka, K. Kuroki, F. Nakamura, and Y. Maeno, Science **358**, 1084 (2017).

Summary

Superconductivity is a phenomenon characterized by electrons condensing into a Bosonic state, described as a single, quantum mechanical function. The Bardeen-Cooper-Schliefer (BCS) theory for superconductivity, formulated in 1957, is able to characterize only a select class of superconductors, generally having a critical temperature (T_c) below 30 K. The theory does not (seem to) be valid for high-T_c superconducting copper oxides (cuprates). These cuprate superconductors behave differently in a number of important aspects.

Cuprate superconductors typically have an insulating ground state, and doping of this insulator changes its electronic properties. Only when the cuprate is supplied with the correct amount of doping does one get superconductivity below its T_c. Hence, the cuprate is characterized with distinct insulating and superconducting phases in a so-called phase diagram of doping vs. temperature. However, between those two phases, one finds an ill-understood pseudogap phase, that is believed to be crucial for the understanding of cuprate superconductivity.

Cuprates are highly anisotropic in their electronic properties such as ξ, the superconducting coherence length. This is due to the layered nature of their unit cell structure, consisting of the crucially important superconducting CuO_2 planes, parallel to the a and b axes of the unit cell (i.e., in-plane directions). Indeed, for a compound like $La_{2\text{-}x}Sr_xCuO_4$, $\xi_{a,b} \simeq 100\xi_c$.

The coherence length plays a crucial role in the superconducting proximity effect. This effect arises when a normal metal is sandwiched between two superconductors and is characterized by an exponential decrease of the superconducting wave function across the normal metal. The superconductors on top and bottom may be either of the conventional type or of the high-T_c type.

What happens now when we replace the normal metal with a cuprate in its pseudogap phase with its c-axis parallel to the interface normal? Surprisingly, the coherence length is amplified by a factor 100 or more; this stunning result is known as the Giant Proximity Effect (GPE). The exact origins of the GPE are still unknown, and could be related to the pseudogap physics of the cuprate.

Given the fact that $\xi_{a,b} \simeq 100\xi_c$, one may expect to observe a proximity effect for distances of up to 10^2 nm along the ab-axis for typical cuprates. With these in mind, the GPE, and in particular the GPE along the ab-axis, forms the central theme of this thesis.

We have employed two methods to induce a GPE along the ab-axis, the first of which is ionic liquid (IL) gating, motivated in part because this approach allows creating a junction in a film that is structurally homogeneous. This method makes use of a molten (molecular) salt to achieve high charge carrier densities. The application of a bias voltage across the ionic liquid forms an electric double layer at the surface of the material which can be gated. This method results in charge carrier densities of the order of $10^{14}/\mathrm{cm}^2$, which is sufficient to traverse the phase diagram of a typical cuprate. The method has its own intricacies and Chapter 2 provides a glimpse into these.

Chapter 3 describes the methods used for the growth of cuprates, namely pulsed laser deposition combined with reflection high energy electron diffraction. In this chapter, the ways of using RHEED data to interpret in-situ growth is explained, along with different parameters for the growth of a number of materials, in particular cuprates such as $\mathrm{Nd}_{2\text{-}x}\mathrm{Ce}_x\mathrm{CuO}_4$, $\mathrm{La}_{2\text{-}x}\mathrm{Sr}_x\mathrm{CuO}_4$ and $\mathrm{YBa}_2\mathrm{Cu}_3\mathrm{O}_{7\text{-}x}$. Furthermore, the methods for attaining ab-axis Josephson junctions are described, among other important aspects pertaining to device manufacturing and ionic liquid handling.

The ionic liquid gating method has first been extensively used on a non-cuprate, namely SrTiO_3, as discussed in Chapter 4. Here, we have found a way of differentiating between electrochemical and electrostatic processes induced by ionic liquid gating. We have found that performing the measurements at low temperatures (close to the melting point of the ionic liquid, 183 K) and at low pressures (10^{-6} mbar) completely removes the electrochemical mechanism, in which case SrTiO_3 charges homogeneously. The resulting 2D electronic system at the surface of SrTiO_3 is characterized by percolation driven transport.

Similar studies have been performed for the cuprates $\mathrm{Nd}_{2\text{-}x}\mathrm{Ce}_x\mathrm{CuO}_4$

(Chapter 5) and $La_{2\text{-}x}Sr_xCuO_4$ (Chapter 6). With the Nd compound we were unable to induce a substantial change in the charge carrier density. Rather, we found that the thin films of $Nd_{2\text{-}x}Ce_xCuO_4$ were very susceptible to electrochemical reactions. These also play a role in the study of the La compound. Albeit in the form of oxygenation, this effectively hole dopes the compound and induces superconductivity in thin $La_{2\text{-}x}Sr_xCuO_4$ films.

Chapter 8 describes the application of the methods presented in Chapter 3 for making an in-plane Josephson junction. Here, ionic liquid gating is applied for an initially superconducting film with low T_c. An artificial junction area of AlO_x is made so that the gating effect on top of this area is blocked by means of a barrier. Although the increased carrier density on the gated areas leads to a higher T_c in the barrier area over distance much larger than $\xi_{a,b}$ (about two orders of magnitude), the results are not yet conclusive as the effect might be caused by possible barrier imperfections, namely porosity.

The second method makes use of etched bilayers (Chapter 7). In short, this method involves the deposition of a film of low T_c ($La_{2\text{-}x}Sr_xCuO_4$) followed by one of high T_c ($YBa_2Cu_3O_{7\text{-}x}$). Next, the top layer is etched away in a specific area using argon ion dry etching. In doing so, a quasi *ab*-axis junction is formed where the flow of electrons between both high-T_c layers passes through the low-T_c area. Backed up by magnetic field measurements, the results seem to support a long range proximity effect along distances much larger than $\xi_{a,b}$. However, inhomogeneities in the method pertaining to the nature of etching process requires further improvements of this approach.

The thesis is finalized with an outlook and conclusion on the origins of the GPE based on key measurements made with both methods in Chapter 9. Despite the limitations of the junctions investigated we conclude that two of the proposed mechanisms of GPE are not favored by the experimental observations.

Samenvatting

Supergeleiding is een fenomeen dat gekarakteriseerd wordt door condensatie van elektronen in een Bosonische grondtoestand, beschreven door één enkele, kwantummechanische functie. De theorie die voor supergeleiders in 1957 is geformuleerd door Bardeen, Cooper en Schliefer (BCS-theorie), is in staat een specifieke categorie van supergeleiders te beschrijven die in het algemeen een kritische temperatuur (T_c) hebben onder 30 K. De theorie lijkt niet toepasbaar te zijn voor hoge-T_c supergeleiders van koperoxides (cupraten). Deze cupraten gedragen zich anders in een aantal belangrijke aspecten.

Cupraat supergeleiders hebben typisch een isolerende grondtoestand, waarbij dotering de elektrische eigenschappen van de isolator verandert. Supergeleiding wordt alleen verkregen wanneer het cupraat voorzien wordt van een correcte hoeveelheid dotering (mits de temperatuur lager is dan T_c). Wanneer de dotering in een fasediagram wordt uitgezet tegen de temperatuur, laat dit zien dat het cupraat wordt gekarakteriseerd door afzonderlijke isolerende en supergeleidende fases. Echter, tussen deze twee fases in bevindt zich de zogenaamde pseudogapfase, een fase die, tot op heden, niet heel goed begrepen is, maar die verondersteld wordt cruciaal te zijn voor ons begrip van supergeleiding in de cupraten.

Cupraten zijn in hoge mate anisotropisch in hun elektrische eigenschappen zoals ξ, de supergeleidende coherentielengte. Dit wordt veroorzaakt door de gelaagdheid van hun eenheidscelstructuur, bestaande uit de supergeleidende CuO_2-vlakken in het a, b-vlak van de eenheidscel. Zo geldt voor een verbinding zoals $La_{2\text{-}x}Sr_xCuO_4$ dat $\xi_{a,b} \simeq 100\xi_c$.

De coherentielengte speelt een cruciale rol in het supergeleidende "proximity" effect. Dit effect ontstaat bijvoorbeeld wanneer een normaal metaal is gesitueerd tussen twee supergeleiders (net als in een boterham). Het wordt gekarakteriseerd door een exponentiële afname van de supergeleidende golffunctie over de dikte van het normale metaal. De supegeleiders boven en onder het metaal kunnen zowel van het conventionele soort als van de hoge-T_c soort zijn.

Wat gebeurt er nu wanneer het normale metaal wordt vervangen door een cupraat dat zich bevindt in zijn pseudogapfase en waarbij de c-as ervan loodrecht op het grensvlak staat? Verrassend genoeg wordt de coherenctielengte opgevoerd, en wel met een factor 100 of meer. Dit verbluffende resultaat staat bekend als het Giant Proximity Effect (GPE). De exacte fysische oorzaken van het GPE zijn vooralsnog onbekend, maar zouden gerelateerd kunnen zijn aan de pseudogapfysica van het koperoxide.

Gezien het feit dat $\xi_{a,b} \simeq 100\xi_c$, zou verwacht kunnen worden dat voor typische cupraten het proximity effect langs de ab-as zich over afstanden tot wel 10^2 nm zou kunnen manifesteren. Daarom vormt het onderzoek naar het GPE, en in het bijzonder naar het GPE langs de ab-as, het centrale thema van dit proefschrift.

We hebben twee methoden gebruikt om een GPE langs de ab-as te induceren. De eerste maakt gebruik van het elektrostatisch induceren van ladingsdragers (*gaten*) met behulp van ionische vloeistoffen. Deze aanpak maakt het mogelijk een junctie tot stand te brengen die structureel homogeen is. De methode maakt gebruik van een gesmolten (moleculair) zout om grote ladingsdragerdichtheden te verkrijgen. Door over de ionische vloeistof een potentiaalverschil aan te brengen, wordt een elektrische dubbellaag gevormd op het oppervlak van het materiaal. Deze methode leidt tot ladingsdragerdichtheden van de orde van $10^{14}/\text{cm}^2$, typisch voldoende om het fasediagram van een cupraat te doorlopen. Hoofdstuk 2 biedt de lezer een idee van wat er bij komt kijken om deze methode toe te passen.

Hoofdstuk 3 beschrijft de methodes die gebruikt zijn bij de groei van cupraten, namelijk gepulste laserdepositie gecombineerd met reflectie hoge-energie elektronendiffractie (RHEED). In dit hoofdstuk wordt de interpratie van RHEED-data, en informatie over verschillende parameters voor de groei van cupraten, met name $Nd_{2\text{-}x}Ce_xCuO_4$, $La_{2\text{-}x}Sr_xCuO_4$ en $YBa_2Cu_3O_{7\text{-}x}$ voorgelegd aan de lezer. Daarnaast worden methodes beschreven voor het verkrijgen van ab-as Josephson-juncties, en worden belangrijke aspecten van structuurfabricage en ionische vloeistofbehandeling toegelicht.

De ionische vloeistof gatingmethode werd eerst uitgebreid toegepast op een niet-koperoxide, namelijk $SrTiO_3$, zoals beschreven in

Hoofdstuk 4. Hierin wordt beschreven hoe we een manier hebben gevonden om te differentiëren tussen elektrochemsiche en elektrostatische processen geïnduceerd door ionische vloeistof gating. Metingen bij lage temperatuur (dichtbij het smeltpunt van de ionische vloeistof, 183 K) en bij lage druk (10^{-6} mbar) verwijdert het elektrochemische mechanisme van gating, en zorgt ervoor dat het oxide homogeen kan opladen. Het resulterende 2D elektronsich systeem op het oppervlak van $SrTiO_3$ wordt gekarakteriseerd door percolatiegedreven transport.

Vergelijkbare studies zijn uitgevoerd op de cupraten $Nd_{2\text{-}x}Ce_xCuO_4$ (Hoofdstuk 5) en $La_{2\text{-}x}Sr_xCuO_4$ (Hoofdstuk 6). We zijn niet in staat geweest om met de Nb-verbinding een substantiële verandering teweeg te brengen in de ladingsdragerdichtheid aan het oppervlak vanwege de grote gevoeligheid van dit materiaal voor elektrochemische reacties. Deze spelen ook een rol in de La-verbinding in de vorm van oxygenatie. Dit proces doteert het materiaal met positieve ladingsdragers en maakt het mogelijk om supergeleiding te induceren in deze films.

Hoofdstuk 8 beschrijft de methodes voor het maken van een Josephson-junctie in het vlak. Hier wordt ionische vloeistof gating toegepast op een dunne supergeleidende film met een lage T_c, waarbij een specifiek gebied door middel van een laag AlO_x op het koperoxide het gatingeffect blokkeert. We nemen waar dat, alhoewel de toegenomen ladingsdragerdichtheid op de niet door AlO_x bedekte gebieden wel leidt tot een hogere T_c in het junctiegebied over afstanden veel groter dan $\xi_{a,b}$ (ongeveer twee ordes van grootte), de resultaten nog niet doorslaggevend zijn vanwege vermoede imperfecties (i.e., porositeit) in het AlO_x.

De tweede methode maakt gebruikt van geëtste dubbellagen (zie Hoofdstuk 7). Hier worden, opeenvolgend een film met een lage T_c ($La_{2\text{-}x}Sr_xCuO_4$) en een film met een hoge T_c ($YBa_2Cu_3O_{7\text{-}x}$) gedeponeerd. Daarna wordt de toplaag weggeëtst op een specifieke manier met een bundel van argonionen. De resulterende quasi-*ab*-as junctie biedt elektronen van beide hoge-T_c elektroden een pad door het lage-T_c gebied van de barrière. De resultaten worden ondersteund door magnetische veldmetingen en wijzen op een "proximity" effect over afstanden die beduidend groter zijn dan $\xi_{a,b}$. Echter, inhomogeniteiten als gevolg van het gebruikte etsproces laten niet toe dat ondubbelzinnige conclusies worden getrokken.

Het proefschrift wordt afgerond met een vooruitblik en een kritische beschouwing over de fysische oorsprongen van het GPE op grond van een aantal cruciale metingen in Hoofdstuk 9. Ondanks de beperkingen van de onderzochte juncties concluderen we voorzichtig dat twee van de voorgestelde mechanismen van het GPE niet de voorkeur hebben.

Curriculum Vitae

Hasan Ateşçi

born on August 10th 1990, in Almelo (The Netherlands)

2002-2008 Secundary Education

Pius X College, Almelo (The Netherlands)

2008-2011 BSc. Applied Physics

University of Twente, Enschede (The Netherlands)
Electronic transport properties of self-assembled monolayers of β-Cyclodextrin (β-CD) molecules
Supervision of Prof. dr. ir. Harold Zandvliet

2011-2013 MSc. Applied Physics

University of Twente, Enschede (The Netherlands)
Electronic properties of Pt and Au induced nanowires on Ge(001) surfaces
Supervision of Prof. dr. ir. Harold Zandvliet

2013-2017 PhD. Research in Physics

Leiden University, Leiden (The Netherlands)
Towards an ab-axis giant proximity effect
using ionic liquid gating
Supervision of Prof. dr. Jan van Ruitenbeek and
Prof. dr. ir. Hans Hilgenkamp

2018-Now Design Engineer

ASML, Veldhoven (The Netherlands)

List of Publications

1. A. Kumar, R. Heimbuch, K. S. Wimbush, H. Atesci, A. Acun, K. Wimbush, H. J. W. Zandvliet, *Electron-Induced Dynamics of Heptathioether β-Cyclodextrin Molecules*, Small **8**, 317-322 (2012).

2. R. Heimbuch, H. Atesci, I. Slootheer, H. J. W. Zandvliet, *Electronic end-states in platinum atom chains*, Surface Science **644**, 91-94 (2016).

3. H. Atesci, F. Coneri, M. Leeuwenhoek, J. W. M. Hilgenkamp, J. M. van Ruitenbeek, *On the nature of ionic liquid gating of* $Nd_{2\text{-}x}Ce_xCuO_4$ *thin films*, Low Temperature Physics **43**, 290 (2017).

4. H. Atesci, F. Coneri, M. Leeuwenhoek, J. Bommer, J. R. T. Seddon, J. W. M. Hilgenkamp, J. M. van Ruitenbeek, *On the formation of a conducting surface channel by ionic liquid gating of an insulator*, accepted for publication in Ann. Phys. (Berlin).

5. H. Atesci, W. Gelling, F. Coneri, J. W. M. Hilgenkamp, J. M. van Ruitenbeek, *On the nature of ionic liquid gating of* $La_{2\text{-}x}Sr_xCuO_4$, International Journal of Molecular Sciences **19**, 566 (2018).

6. H. Atesci, J. W. M. Hilgenkamp, J. M. van Ruitenbeek, *Towards an ab-axis giant proximity effect using ionic liquid gating and etched bilayers*, to be submitted.

Acknowledgements

I start with thanking the Almighty Creator, Allah, for giving me the perseverance to successfully accomplish my thesis. I would also like to thank those that helped me along the way.

Firstly, I would like to express my deepest gratitude to Jan van Ruitenbeek for this great project that he has offered me. His cordial supervision and our helpful and fruitful discussions really helped me a great deal, both personally and professionally. He always patiently listened to my stories and issues when I would walk into his office. Thanks so much! I would also like to express my thanks to Hans Hilgenkamp with whom I enjoyed many discussions. He had many great suggestions, and came up with many out of the box ideas that put new energy into the project. Thank you!

I thank Sasha Vbrica and Sumit Tewari for their stimulating company. It was a pleasure to be part of the same group. My special gratitude goes to my former student Wouter Gelling and his classmates Xavier Le Large and Bart Woltjes for the nice moments we shared together, and the occasional moments at the coffee machine. I would like to thank Jan Aarts for allowing me to use his measurement setups for some years and Amrita Singh and Stefano Voltan for their cordial advice on critical aspects of experimental issues. Furthermore, I would like to extend my thanks to my university neighbor Sander Blok, for his help with operating the cryostat, and fruitful discussions. Marcel Hesselberth for his in-depth knowledge of a lot of processing steps required for my research, and the same goes for Daan Boltje and Douwe Scholma. Federica Galli, thank you for your help and good company! Next, I thank Peter van Veldhuizen from the electronics department, and Ellie, Charlotte and Shirley for their administrative support.

To those (who used to be) at the University of Twente, I would like to thank Francesco Coneri, for his optimism and help in picking things

up very quickly in the beginning of my project. Frank Roesthuis has been a great help and partner as well. I could always come to you whenever I needed help, not only for urgent problems, but also for the more generic things. Thanks a lot! Thank you Dick Veldhuis for help with the probe station and helium, among other things. I would like to thank Sander Smink for tips and tricks regarding processing and RHEED techniques, and Pim Reith for his Nb test samples, and Jouri Bommer for his valuable help during the research project, and the same goes for James Seddon and Serge Lemay. Many thanks to Adil Acun, my long time friend, for his companionship and for inviting me to his LEEM machine and occasional tea and coffee and cordial discussions at the University of Twente.

Last but not least, I would like thank my family members, my father, my sister, brother, and my twin brother Hüseyin, with whom I have not only completed my prenatal journey, but also my preliminary school, secondary school and university education. We have even found jobs at the same place! I think that is special. This part of the thesis would be incomplete without a special sentence devoted to my mother for her continued warmth, love and support before, during and after the project.